

Diffusion processes and nanoparticle growth

Claudia Fanelli

Supervised by Prof. Dr. Timothy G. Myers

Submitted in fulfillment of the requirements
for the degree of Doctor in Philosophy in Applied Mathematics
in the Facultat de Matemàtiques i Estadística
at the Universitat Politècnica de Catalunya.

2020, Barcelona, Spain.



Acta de qualificació de tesi doctoral

Curs acadèmic:

Nom i cognoms

Programa de doctorat

Unitat estructural responsable del programa

Resolució del Tribunal

Reunit el Tribunal designat a l'efecte, el doctorand / la doctoranda exposa el tema de la seva tesi doctoral titulada

Acabada la lectura i després de donar resposta a les qüestions formulades pels membres titulars del tribunal, aquest atorga la qualificació:

☐

NO APTE

☐

APROVAT

☐

NOTABLE

☐

EXCEL·LENT

(Nom, cognoms i signatura)		(Nom, cognoms i signatura)	
President/a		Secretari/ària	
(Nom, cognoms i signatura)	(Nom, cognoms i signatura)	(Nom, cognoms i signatura)	
Vocal	Vocal	Vocal	

_____, _____ d'/de _____ de _____

El resultat de l'escrutini dels vots emesos pels membres titulars del tribunal, efectuat per la Comissió Permanent de l'Escola de Doctorat, atorga la MENCIÓ CUM LAUDE:

☐

SÍ

☐

NO

(Nom, cognoms i signatura)		(Nom, cognoms i signatura)	
President/a de la Comissió Permanent de l'Escola de Doctorat		Secretari/ària de la Comissió Permanent de l'Escola de Doctorat	

Barcelona, _____ d'/de _____ de _____

Acknowledgments

This manuscript does not do justice to four very long years in which I have tried to find my way in this world. I did not find it, but I have found some people that have helped me become a better version of myself after all. For this reason I would like to thank those people who have crossed my way at some point and left a mark.

I would like to thank my supervisor Tim Myers, for giving me the chance to see what being a researcher could and could not mean.

I would like to express my sincere gratitude to Katerina Kaouri for making possible my visit to Cardiff and our project together. I admire not only her enthusiasm and passion for science, but also her capacity to always keep in mind looking at the real world, which is something that I have barely found during my journey in this field. Without any doubt she gave me some lost hope back, both in a professional and personal way, and I sincerely hope that our paths will cross again.

I would also like to thank Tim Phillips for sharing some of his knowledge and giving me precious advice with patience and kindness.

Además quiero agradecer la invaluable aportación moral y científica que Francesc ha hecho a esta tesis, especialmente en momentos críticos. Su amabilidad y su fuerza de voluntad han sido fundamentales para no rendirse ante las muchas dificultades encontradas en este mundo.

En segundo lugar, sin duda ninguna no habría podido llegar a acabar esta tesis sin Alberto. Gracias por la infinita paciencia, por haberme hecho sentir finalmente en casa, por la increíble capacidad de querer ver el lado positivo en todo (incluso en mí!) y sobre todo gracias por contribuir cada día a hacerme la luchadora incansable que crees que soy.

También quiero agradecer a esos compañeros de trabajo que al final han sido mucho más. Gracias a Helena, por las infinitas risas (y algunas lágrimas), por haber aprovechado conmigo del lado mejor de Catalunya, desde Montserrat a la Costa Brava pasando por las paellas con gusto a justicia social y las cervezas que después *et fa mal el cap*. Gracias por haber sido colega, amiga y familia todo en una, durante todos estos años y a pesar de la

distancia. Grazie a Carmelo, per le risate, per i tour eno-gastronomici catalani che poi finivano a Aperol e prosecco, per la quantità di ore in cui mi ha pazientemente ascoltato lamentarmi di qualsiasi cosa esista sulla faccia della terra, ma più di tutto grazie per essere stato sempre presente. Gracias a Gemma, por su incansable sonrisa y ganas de hacer, por todo el apoyo que siempre me ha demostrado y por haber sido una amiga en una vida llena de conocidos. Gracias a Marina y Carles, por las muchas conversaciones nunca banales, por las luchas continuas y a veces exasperantes que compartimos y que a menudo no serían soportables sin el apoyo mutuo. Gracias también a quién me ha regalado muchas sonrisas y ayudado en momentos difíciles haciendo cada día este viaje mucho más ligero: Víctor, Daria y Nico. I would also like to thank Vinnie, for giving me many precious advice and countless laughter. Además quiero agradecer a Natàlia Castellana, por haberme apoyado en el momento más difícil de este doctorado, demostrándome que se puede ser investigadoras diferentes y que hay que luchar por ello.

Mis agradecimientos también van a quién me ha apoyado cada día desde fuera y a veces desde lejos. Gracias a Stop Mare Mortum, por haber compartido una inquietud diaria y el camino para intentar cancelarla. En particular gracias a Marta, por la filosofía con que intentamos encontrar nuestro sitio en el mundo y por recordarme de mirar al mar cada vez que todo me ha parecido negro. Grazie a Francesca e Silvia, compagne gattare insostituibili, trovate nella matematica senza saperne troppo bene il perché, tenute strette nella vita per innumerevoli ragioni. Un profondo grazie va anche alle romane e ai romani (di nascita e acquisite) che mi sono state vicino da lontano, e in particolare a Flavia e Cristiana, per farlo incessantemente da così tanto tempo. También quiero agradecer a mi hermosa Galicia y a la gente que me ha traído en la vida. Sin duda hay un antes y un después de conocerte y mi tiempo contigo ha sido de incalculable valor.

Un enorme grazie, infine, va alla mia famiglia. In particolare ai miei genitori, per avermi supportato in questo viaggio ma soprattutto per avermi supportato ogni giorno della mia vita (compito, lo ammetto, alquanto complicato). E grazie ai miei nipoti, gli unici in grado di farmi tornare a sorridere anche nei momenti più bui passati in questi ultimi anni.

Last but not least, thanks to my awesome flatmates Gertrude and Spadina, for being my endless source of happiness.

Finally, I want to acknowledge financial support from the Spanish Ministry of Economy and Competitiveness, through the “Maria de Maeztu” Programme for Units of Excellence in R&D.

Outline

The main body of this thesis is split into two parts. Part I deals with a mathematical model for nanoparticles growth in solution. Part II analyses mathematical and physical aspects of magnetic drug targeting. Chapter 1 is a general introduction to those topics. Chapter 2 is an overview of the classical techniques to solve a particular Stefan problem related to the one studied in the first part of the thesis. Chapter 3 analyses the standard model for the growth of a single particle in solution. Chapter 4 presents an extended version of the same model for a system of N nanoparticles. Chapter 5 deals with the mathematical modelling of nanodrug delivery. Chapter 6 contains the conclusions.

The list below include the publications derived from this thesis. From 1 to 3, correspond to Chapters 3, 4 and 5, respectively.

1. T. G. Myers, C. Fanelli. *On the incorrect use and interpretation of the model for colloidal, spherical crystal growth*. Journal of Colloid and Interface Science, 536, pp. 98–104 (2019). *Impact factor: 6.361*.
2. C. Fanelli, V. Cregan, F. Font, T. G. Myers. *Modelling nanocrystal growth via the precipitation method*. To appear in International Journal of Heat and Mass Transfer, (2020). *Impact factor: 4.346*.
3. C. Fanelli, K. Kaouri, T. N. Phillips, F. Font, T. G. Myers. *Mathematical modelling of a non-Newtonian nanofluid under the influence of an external magnetic field with applications in drug delivery*. In preparation.

Abstract

It is well-known that many properties of nanoparticles, such as luminescence, photostability, optical radiation efficiencies and electric properties, are size dependent. Hence, the ability to create nanoparticles of a specific size is crucial. In this thesis, we begin by developing mathematical models for the nanoparticle growth process and so obtain guidelines for efficient growth strategies. Once the growth process is understood we move on to a specific practical application of nanoparticles, namely targeted drug delivery. In the first part, the mathematical model analysed is a non-standard Stefan problem where the moving boundary is the surface of the particles. In the second part, the model involves the motion of a non-Newtonian nanofluid subject to an external magnetic field and an advection-diffusion equation for the concentration of the nanoparticles in the fluid. In both cases we employ several mathematical tools, such as similarity solutions, asymptotic analysis and numerical techniques.

In Chapter 2 we work on a simple but representative Stefan problem with constant boundary values by means of analytical and numerical methods in order to identify the key mathematical aspects of this type of problem. In Chapter 3 the standard model for the growth of a single nanoparticle in solution is presented and analysed using the techniques developed in the previous chapter. Particular attention is paid to the validity of the assumptions regularly made in literature. Specifically, the analysis of the diffusion boundary layer shows how the standard model does not hold at early times, while the pseudo-steady assumption is found to be valid. Moreover, within experimental error a new analytical solution for the particles radius depending only on two independent parameters is determined. This demonstrates that the model is unable to distinguish between diffusion and reaction driven growth. In Chapter 4 the model of Chapter 3 is extended for

a system of N particles, where N is arbitrarily large. By non-dimensionalising the system and identifying dominant terms, the problem is reduced and solved by analytical and numerical techniques. The Gibbs-Thompson equation for the solubility of the particles shows the importance of this effect in order to control Ostwald ripening, which is driven by the delicate balance between the bulk concentration and the particles solubility. The comparison with experimental data and the analytical solution found in the previous chapter shows excellent agreement, giving an important tool to control the particle size distribution and optimise strategies for the growth.

The second part of the thesis deals with a practical use of nanoparticles, the promising medical technique of magnetic drug targeting. In Chapter 5 a mathematical model for the transport of drug nanocarriers in the bloodstream under the influence of an external magnetic field is presented. Simplifications of the geometry allows the reduction of the Navier-Stokes equations for the blood flow. Within the restrictions of these simplifications analytical solutions are obtained. The comparison between the Newtonian and non-Newtonian approximations shows the importance of taking into account the shear-thinning behaviour of the blood when modelling drug delivery. In this scenario, the viscosity of the blood, which changes depending on the shear rate, is crucial in the calculation of the velocity of the magnetic particles in the vessel and non-Newtonian models need to be used. The ultimate goal is to determine strategies to maximise drug delivery to a specific site.

Resumen

Es conocido que muchas propiedades de las nanopartículas, como la luminiscencia, la fotoestabilidad, la eficiencia de la radiación óptica y las propiedades eléctricas, dependen del tamaño. Por lo tanto, la capacidad de crear nanopartículas de un tamaño específico es crucial. En esta tesis, desarrollamos modelos matemáticos para el proceso de crecimiento de nanopartículas con el objetivo de obtener pautas para estrategias de crecimiento eficientes. Una vez comprendido el proceso de crecimiento, analizamos una aplicación práctica de las nanopartículas, conocida como la liberación controlada de fármacos. En la primera parte, el modelo matemático analizado es un problema no estándar de Stefan donde la frontera libre es la superficie de las partículas. En la segunda parte, tratamos un modelo para el movimiento de un nanofluido no newtoniano sujeto a un campo magnético externo y una ecuación de advección-difusión para la concentración de las nanopartículas en el fluido. En ambos casos empleamos varias herramientas matemáticas, como variables de similitud, análisis asintótica y métodos numéricos.

En el Capítulo 2 analizamos un problema de Stefan con valores constantes en la frontera mediante métodos analíticos y numéricos para identificar los aspectos matemáticos clave de este tipo de problema. En el Capítulo 3 se presenta y analiza el modelo estándar para el crecimiento de una sola nanopartícula en una solución líquida utilizando las técnicas desarrolladas en el capítulo anterior. Se presta especial atención a la validez de las hipótesis que se hacen regularmente en la literatura. Específicamente, el análisis de la capa límite de difusión muestra como el modelo estándar no se cumple para tiempos pequeños, mientras que la hipótesis de estado pseudoestable es válida. Además, se obtiene una nueva solución analítica para la evolución del radio de la partícula que solo depende de dos parámetros independientes. Esta solución demuestra que el modelo no puede distinguir entre la difusión

y el crecimiento impulsado por la reacción. En el Capítulo 4, el modelo del Capítulo 3 se extiende para un sistema de N partículas, donde N es arbitrariamente grande. A través de la adimensionalización del sistema e identificación de los términos dominantes, el problema se reduce y se resuelve mediante técnicas analíticas y numéricas. La ecuación de Gibbs-Thompson para la solubilidad de las partículas muestra la importancia de este efecto para controlar la maduración de Ostwald, que es impulsada por el delicado equilibrio entre la concentración de la solución lejos de la superficie y la solubilidad de las partículas. La comparación con los datos experimentales y con la solución analítica encontrada en el capítulo anterior muestra excelente resultado, dando una herramienta importante para controlar la distribución del tamaño de las partículas y optimizar las estrategias para el crecimiento.

La segunda parte de la tesis trata sobre un uso práctico de las nanopartículas: la liberación de fármacos controlada. En el Capítulo 5 se presenta un modelo matemático para el transporte de nanopartículas portadoras de fármacos en el vaso sanguíneo bajo la influencia de un campo magnético externo. Las simplificaciones geométricas realizadas permiten reducir las ecuaciones de Navier-Stokes para el flujo sanguíneo y encontrar soluciones analíticas válidas dentro de los límites establecidos por dichas simplificaciones. La comparación entre los modelos newtonianos y no newtonianos muestra la importancia de tener en cuenta la reología pseudoplástica de la sangre a la hora de modelar la administración de fármacos. En este escenario, la viscosidad de la sangre, que cambia en función de la velocidad de corte, es crucial en el cálculo de la velocidad de las partículas magnéticas en el vaso sanguíneo y es necesario utilizar modelos no newtonianos. Finalmente, a partir del modelo formulado se establecen estrategias para maximizar la liberación de medicamentos en un sitio específico.

Contents

Acknowledgments	v
Outline	vii
Abstract	viii
1 Introduction	1
I Nanoparticle growth	7
2 Moving boundary problems	9
2.1 Introduction	9
2.2 The mathematical model	10
2.3 Small time analysis	12
2.3.1 Similarity solution method	13
2.3.2 Laplace transform	15
2.4 Exact and approximate solutions for large times	17
2.4.1 Similarity solutions	17
2.4.2 Perturbation theory	19
2.4.3 Heat Balance Integral Method	20
2.4.4 Numerical approximation	24
2.5 Results	26
3 A model for colloidal, spherical crystal growth	27
3.1 Introduction	28

3.2	Growth of a single particle	29
3.2.1	Pseudo-steady state solution	31
3.3	Standard solution method	32
3.4	Diffusion and kinetics driven cases	33
3.5	Validity of the assumptions	35
3.6	An explicit solution for $r(t)$	37
3.7	Conclusion	42
4	Modelling nanocrystal growth via the precipitation method	45
4.1	Introduction	46
4.2	Growth of a single particle	49
4.2.1	Nondimensionalisation	53
4.2.2	Pseudo-steady state solution	55
4.3	Evolution of a system of N particles	56
4.4	Comparison of model with experiment	57
4.4.1	Parameter estimation via the analytical solution	58
4.4.2	Validating the pseudo-steady state approximation	59
4.4.3	Ostwald ripening with $N = 2$	61
4.4.4	N particles system	62
4.4.5	Optimal strategies for growth	64
4.5	Conclusions	65
II	Drug delivery at the nanoscale	67
5	Magnetic drug targeting	69
5.1	Introduction	69
5.2	A mathematical model for magnetic drug delivery	73
5.2.1	The magnetic field	76
5.3	Blood as a non-Newtonian fluid	78
5.3.1	Governing equations and nondimensionalisation	82
5.3.2	Comparison of the models	85

5.3.3	Velocity and viscosity	87
5.4	Concentration of nanoparticles	89
5.4.1	Nondimensionalisation of the advection-diffusion equation	91
5.4.2	Analytical solutions	92
5.5	Numerical approximations	95
5.5.1	Small time analysis	95
5.5.2	Parameter estimation	95
5.5.3	Finite difference scheme	98
5.5.4	Results	99
5.6	Conclusion	107
6	Conclusions	109
	Bibliography	113

List of Figures

1.1	Sketch of Ostwald ripening in the case of two particles with different radius.	3
1.2	Microscopy images of the growth of gold seed particles at different time steps from Bastús <i>et al.</i> [10].	3
1.3	<i>In vivo</i> images of intracellular labelling of tumour cells by semiconductor nanocrystals quantum dots of different sizes from [114].	5
2.1	Sketch of a particle growing in a solution.	11
2.2	Comparison of (a) the concentration and (b) the particle radius profiles given by the similarity variables method (dashed line), the HBIM (dots) and the numerical approximation (solid line) with $\varepsilon = 0.01$	26
3.1	Chuang <i>et al.</i> [23] $G = 28.28, r_m = 2.892, n = 5$ ($n = 6, G = 28.56 = 1\%$ change), Bullen <i>et al.</i> [17] $G = 18.82, n = 4, r_m = 2.015$	41
3.2	Pan <i>et al.</i> [85] $G = 1166, n = 5, r_m = 1.75$, Su <i>et al.</i> [102] $G = 789.3, n = 9, r_m = 1.24$	41
4.1	Schematic of a single nanoparticle with radius r_p^* and the surrounding monomer concentration profile where s^* , c_i^* and c_b^* are the particle solubility, the concentration at the surface of the particle and the far-field concentration, respectively.	50
4.2	The circles represent the experimental data from Peng <i>et al.</i> [89] and the solid line the corresponding least-squares fit to the analytical solution, equation (4.21) with $G = 958$. The dashed line is the PSS model with the same value of G	58

4.3	Solution of the full and the PSS models (represented by circles and by a solid line, respectively) for the growth of a single particle. Panel (a) shows the evolution of the particle radius and panel (b) the concentration of monomer around the particle at five different times.	60
4.4	Evolution of two CdSe nanoparticles. (a) Change in time of the radii of two particles with initial radii of 2 nm (dashed line) and 2.5 nm (solid line). (b) Change in bulk concentration (dotted line) and solubilities of smaller (dashed line) and larger (solid line) particles.	62
4.5	Comparison of the model for N particles (dashed lines) with experimental data from Peng <i>et al.</i> [89] (dots) using $N = 10$ in (a) and $N = 1000$ in (b). The solid lines represent the explicit solution for the one particle model, equation (4.21). The inset plots show the percentage difference between the models.	63
4.6	Evolution of the radius varying the time of further injections.	65
5.1	Different types of vessels in the circulatory system. Image credits to the U.S. National Library of Medicine [92].	73
5.2	Sketch of the injection of magnetic nanoparticles in a vessel in the presence of red blood cells and subject to an magnetic field.	75
5.3	The viscosity/shear rate plot in logarithmic scale for the power law (red dotted-dashed line), the Carreau (black solid line) and the Ellis models (green dashed line). The light grey dashed lines represents the constant limit viscosities η_0 and η_∞	81
5.4	Comparison of (a) velocity and (b) viscosity profiles of Newtonian (represented by the letter N and the blue dotted line), power-law (represented by PL and the red dashed-dotted line), Carreau (represented by the letter C and the black solid line) and Ellis model (represented by the letter E and the green dashed line).	88

-
- 5.5 Snapshots of the concentration of particles in an artery at six different times ($t = 0\text{s}$, $t = 4\text{s}$, $t = 6\text{s}$, $t = 10\text{s}$, $t = 15\text{s}$, $t = 30\text{s}$), choosing the Newtonian model for the blood flow and with a constant magnetic force equal to $F_0 = 1 \times 10^{-13}$ N. The first image represents the velocity field. 102
- 5.6 Motion of magnetic nanoparticles in an artery at six different times ($t = 0\text{s}$, $t = 4\text{s}$, $t = 6\text{s}$, $t = 10\text{s}$, $t = 15\text{s}$, $t = 30\text{s}$ and $t = 40\text{s}$), choosing the Carreau model for the blood flow and with a constant magnetic force acting on particles equal to $F_0 = 8 \times 10^{-13}$ N. The first image represents the velocity field. 103
- 5.7 Snapshots of the concentration of particles in an artery at six different times ($t = 0\text{s}$, $t = 4\text{s}$, $t = 6\text{s}$, $t = 10\text{s}$, $t = 15\text{s}$, $t = 30\text{s}$), choosing the Ellis model for the blood flow and with a constant magnetic force equal to $F_0 = 1 \times 10^{-13}$ N. The first image represents the velocity field. 104
- 5.8 Motion of magnetic nanoparticles in an artery at six different times ($t = 0\text{s}$, $t = 4\text{s}$, $t = 6\text{s}$, $t = 15\text{s}$, $t = 30\text{s}$ and $t = 40\text{s}$), choosing the Carreau model for the blood flow and with a constant magnetic force acting on particles equal to $F_0 = 8 \times 10^{-13}$ N. The first image represents the velocity field. 105
- 5.9 Motion of magnetic nanoparticles in an artery at six different times ($t = 0\text{s}$, $t = 4\text{s}$, $t = 6\text{s}$, $t = 15\text{s}$, $t = 30\text{s}$ and $t = 40\text{s}$), choosing the Ellis model for the blood flow and with a constant magnetic force acting on particles equal to $F_0 = 8 \times 10^{-13}$ N. The first image represents the velocity field. 106

List of Tables

3.1	Comparison of the parameters for nanocrystal growth in different studies. . .	34
4.1	Physical parameters for the cadmium selenide (CdSe) nanoparticle synthesis method used by Peng <i>et al.</i> [89]. The parameters in italics are not given explicitly and are obtained via a fitting approach.	59
5.1	Typical values for the various types of vessels in human body: average length (L) and width (R), estimation of the average number of a specific vessel in the circulatory system (N). All values are adapted from [38].	74
5.2	Typical parameters for the blood flow equations for each model.	82
5.3	Dimensional parameters for the particles concentration equation.	98

1 | Introduction

During the last decades it has been shown that nanotechnology-based industry can develop materials, devices and systems that will change the way to work and manage scientific challenges in a wide range of applications, like biomedicine [41, 42], environmental-related problems [1], electronics and catalysis [9, 11, 26]. The formal definition of nanomaterials requires the material to be man-made and with dimensions between 1 and 100 nanometers (nm). But why is nanoscale so interesting? Nanoparticles (NPs) have unique properties that naturally occur at that scale. There are two main features that show the power of nanoscale:

1. **Surface area to volume ratio:**

Materials made up of nanoparticles have a greater surface area when compared to the same volume of material made up of larger particles. This means that a great amount of the material can come into contact with surrounding materials, increasing the reactivity.

2. **“Tunability” of properties:**

With slight changes in size, a scientist is able to control and adapt a nanomaterial property, such as electronic and optical properties of metals and semiconductors [74], luminescence and photostability [46, 54], and optical radiation efficiencies [105], among others.

Since many of these properties are size dependent, the ability to create nanoparticles of a specific size is crucial.

A famous example that shows the great potential of this scale involves gold nanoparticles. At the nanoscale, the motion of the gold’s electrons is confined and, because of that, they

react differently with light compared at a larger scale. The result is that gold nanoparticles are not yellow as we expect, but can appear red or purple according to their size. Moreover, adjusting their dimensions, gold nanoparticles can be tuned according to the purpose: for example, they can selectively accumulate in tumours in order to identify diseased cells and to target laser destruction of the tumour avoiding healthy cells.

This thesis is devoted to providing a greater understanding of certain nanoscale processes. In the first part the growth of nanoparticles is studied, with the aim of providing guidelines for improving and optimising the process. In the second part a specific applications for nanoparticles is considered. Specifically, the targeted delivery of magnetic nanoparticles is modelled.

Over the past 40 years, growing nanoparticles to a specific size has been the object of several studies. It is known that they can be prepared by both gas phase and solution based synthesis techniques. Although the first method can produce large quantities of nanoparticles, agglomeration and nonuniformity in particle size and shape are typical problems [69]. Using the precipitation method monodisperse spherical nanoparticles can be generated. The standard approach is to apply the classical La Mer and Dinegar synthesis strategy where nucleation and growth are separated [58, 59]. The strategy is to rapidly add the precursor at high temperature into batch reactors, causing a short nucleation burst in order to create a large number of nuclei in a short space of time. To separate the nucleation from growth, the reactor is cooled and the nanoparticles formed start to grow [119]. The subsequent growth involves two different stages:

1. The focusing period, where particles increases rapidly and the size distribution is relatively small.
2. The defocusing period, where the growth slows down and the size distribution become larger.

The first phase leads to the desired result of monodisperse nanoparticles. In the second phase we can observe a phenomenon called Ostwald ripening (OR), a process by which larger particles grow at the expense of the smaller ones which dissolve due to their much higher solubility. This process, schematized in Figure 1.1, produces monomer, which is subsequently used to support growth of the larger particles. However, this simultaneous

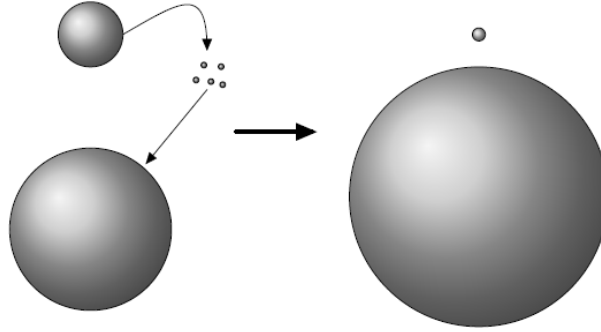


Figure 1.1: Sketch of Ostwald ripening in the case of two particles with different radius.

growth and dissolution leads to the unwanted defocusing of the particle size distribution (PSD).

Recently, it has been shown that the PSD can be refocused by changing the reaction kinetics. For example, in Figure 1.2, we can see a series of snapshots of the growth process of gold nanoparticles from Bastús *et al.* [10], where temperature, gold precursor to seed particle concentration, and pH are adjusted during the process in order to obtain the desired result. The project studied in the first part of this thesis is motivated by the desire for a deeper understanding of nanoparticles synthesis. This is motivated by the work of the Inorganic Nanoparticles group research from the Institut Català de Nanociència i Nanotecnologia (ICN2), where the main authors of [10] worked.

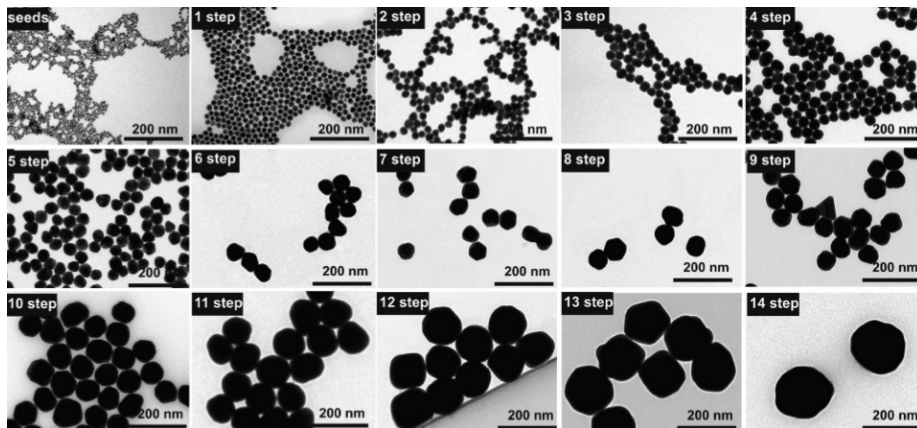


Figure 1.2: Microscopy images of the growth of gold seed particles at different time steps from Bastús *et al.* [10].

In order to model this process, it will be shown how, from a mathematical point of view, the growth of single nanoparticle is analogous to a one-phase Stefan problem. This is a particular kind of boundary value problem for a partial differential equation where the position of the border is time-dependent and has to be found as an unknown variable of the system. In literature the equation that defines this position, commonly known as the Stefan condition, usually describes the temperature distribution under a phase-change but it is found to be perfectly suitable to define the growth evolution. To help understand this complex nanoparticles growth problem, in Chapter 2 several analytical and numerical techniques for solving a related Stefan problem are summarized and compared. Simplifications are made in order to obtain analytical solutions and anticipate the behaviour of the concentration of particles in a solution-based synthesis. However, there exist very few practically useful exact solutions to moving boundary problems and so other types of approximations will be studied, such as perturbation techniques, the heat balance integral method and its improvements, and finally numerical methods.

Chapter 3 is dedicated to the correct interpretation of the standard model for the growth of a single spherical particle and has already been published [79]. The main results concern the limited time-range for the validity of this model and the impossibility to distinguish between diffusion or surface reaction driven growth in the pseudo-steady approximation. Moreover, an explicit equation for the growth of the particle radius is given which is shown to depend only on two independent parameters. Finally, the importance of the variation of particle solubility is highlighted, especially during the initial phase of the growth.

The single particle model may be adapted to approximate the evolution of the average radius of a group of similar sized nanoparticles. However, in order to understand and control the undesired Ostwald ripening we need to keep track of the radius of each particle. For this reason, an N particle model will be developed and described in Chapter 4. This model incorporates the particle solubility variation which then permits the model to capture OR. The $N = 2$ model can equally well represent the average radii for an initially bimodal distribution of nanocrystals while an $N > 2$ model can represent a much larger distribution of particles. This work has been already accepted and is pending printing [29].

In order to show a practical use of the ability to control the size of nanoparticles, it is interesting to introduce some applications in the field of biomedicine. Many medical

researchers are facing a wide variety of challenges, including the detection of disease-specific biomarkers in the blood, targeted magnetic resonance imaging contrast agents in the field of neurological surgeries, the specific detection of DNA and proteins, and many others [31]. For example, as already mentioned above, gold nanoparticles can be precisely built in order to selectively activate through tissue irradiation for therapeutic thermal ablation. In Figure 1.3 we can see *in vivo* images of intracellular labelling of tumour cells by quantum dots from the experimental work of [114]. A precise map of the distribution of many molecular markers can be generated by irradiation, conjugating each colour (i.e. each size) of nanoparticles with antibodies to different molecular targets. However, it is recognized that novel mathematical models are needed in order to secure the added value of nanotechnology into the medical field [31].

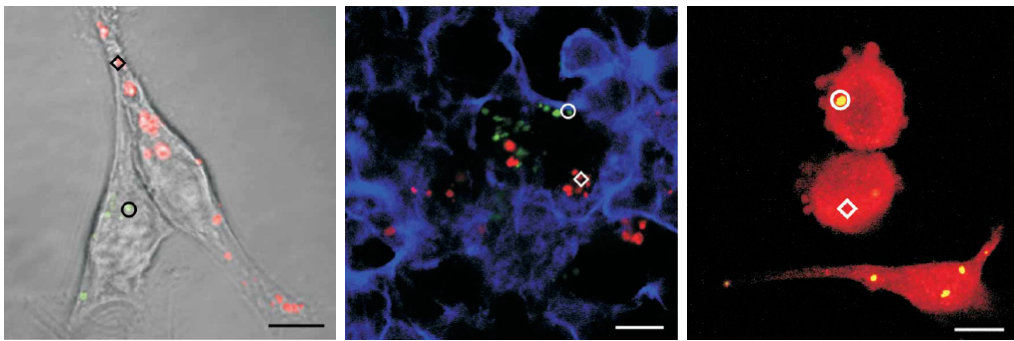


Figure 1.3: *In vivo* images of intracellular labelling of tumour cells by semiconductor nanocrystals quantum dots of different sizes from [114].

After understanding the growth process of nanoparticles, the aim of the second part of this thesis is to look at a practical use for NPs. Specifically, a model is developed for a very popular and effective way to introduce drugs in selected parts of human body in the context of cancer therapy: magnetic drug targeting. This technique consist in attaching a drug to a biocompatible magnetic nanoparticle carrier, injecting them into the circulatory system and then using a high gradient magnetic field to direct them to the target region. One of the great potentials of selectively reaching the desired targets is to avoid, or at least reduce, collateral damage. Currently, the main approaches for cancer treatment are non-specific and their efficacy is low. The technique of magnetically targeted drug delivery will allow to deliver the drugs directly to the tumour cells which results in minimizing the doses

required and, especially, avoiding undesired side effects. The main advantages of magnetic nanoparticles lies on two fundamental aspects: firstly, their controllable size are smaller than or comparable to some important biological entities, like genes, cells, proteins or virus, and therefore adapt to interact with them; secondly, they respond to external manipulation such as magnetic fields making them easy to transport or heat up from a distance. However, the success of the therapy also depends of many physical aspects, such as hydrodynamic and physiological parameters. In fact, controlling the balance between magnetic and blood drag forces is one of the main difficulties of this technique.

The movement and directing of magnetic nanoparticles in specific vessels of the circulatory system subject to an external magnetic field is the focus of Chapter 5. The goal is to investigate the evolution of the physical situation taking into account all the forces acting on the drug carriers. The mathematical model consists of a system of nonlinear partial differential equations formed by the Navier-Stokes equations for the flow of the blood coupled with an advection–diffusion equation for the concentration of nanoparticles. It is important to notice that blood is a biological fluid that reaches the whole body and understanding its rheological and flow properties is essential in order to develop tools to handle the great majority of the diseases. Its composition results in non-Newtonian characteristics which can affect drastically the particle dynamics. Geometry simplifications of the chosen vessel permit the comparison between several models for the velocity and the viscosity of the fluid, highlighting the importance to choose an accurate approximation. Once obtained the profile for the flow of the blood, the equation for the concentration of magnetic nanoparticles is analysed and solved by numerical techniques. The main results concern the ability to understand whether the magnetic force can compete with drag force when considering a correct approximation for the viscosity of the blood.

Part I

Nanoparticle growth

2 | Moving boundary problems: analytical and numerical techniques

2.1 Introduction

Many real-life problems in the area of applied science lead to a partial differential equation coupled with a moving boundary condition, such as the melting of ice, alloy solidification, freezing of soil, ablation, oxygen diffusion and many others. The classical formulation of these type of problems was introduced by Josef Stefan in 1889 (and named after him) and deals with the phenomenon of solid-liquid change of phase [101]. In this first paper, he modelled the growth of sea ice, solving a one dimensional diffusion equation (resulting from conservation of heat) with a moving boundary between a polar ice cap and the ocean. Nowadays, it is known that a lot of industrial problems can be modelled through an adaptation of the classical Stefan theory. In the first part of this thesis we will focus on a model for spherical nanoparticle growth in a solution, that is mathematically equivalent to a one phase Stefan problem. The process is described by a diffusion equation for the concentration of the solution, a Stefan condition for the evolving particle radius and a mass conservation expression for the bulk concentration, and is a very interesting case of these kind of problems.

The aim of this chapter is to study analytical and numerical techniques in order to solve a related but simplified problem which may aid in the analysis of the nanoparticle growth model. The techniques will be applied to standard configurations and then, if possible,

adapted in subsequent chapters for the physical problem.

There are a very few practically useful exact solutions to moving boundary problems. An exact analytical solution of the Stefan problem is possible only in a few cases even in the one-dimensional case, and is mostly based on special type of solutions written in terms of error and complementary error functions [47, 48]. Consequently many analytical approximations and numerical techniques have been developed in the literature. In the next sections, several approaches are described following the direction of the classical one phase case. Firstly, similarity solutions and Laplace methods are used for small and large times, to obtain expressions for the concentration and the radius of the particle [25]. Secondly, due to the presence of a small parameter ε multiplying the time derivative in the diffusion equation, we analyse the pseudo-steady case, which is a reasonably good approximation of the problem as $\varepsilon \rightarrow 0$. Assuming the dependence of the solution on this parameter, it can be determined using a Taylor series expansion about $\varepsilon = 0$ where the pseudo-steady solution appears as the first term in this expansion [49]. For this reason, perturbation techniques have been applied to derive higher order terms to improve the accuracy of the approximation [12, 18, 49, 55]. An interesting example of these methods applied to physical problems can be found in [120], where it is considered the case of the solidification of a finite slab with convective cooling and shrinkage. In cases where $\varepsilon = \mathcal{O}(1)$ we have employed the Heat Balance Integral Method (from now on HBIM) to find approximate solutions to our parabolic equation. This method was initially introduced by Goodman [43, 44] and gained popularity due to its simplicity, although the accuracy depends on the choice of an approximating function [73]. In 1973, Langford [60] proposed a definition of an error for the HBIM method and later an interesting improvement has been developed and applied to several forms of Stefan problem [72, 73, 77, 78, 80]. Finally, the solutions obtained through the analysis are compared with numerical results via finite difference methods using the boundary-fixing technique [37, 57].

2.2 The mathematical model

As introduced in the previous section and represented in Figure 2.1, we will analyse a mathematical model for the growth of a single particle of radius \hat{R} in a bulk solution. The

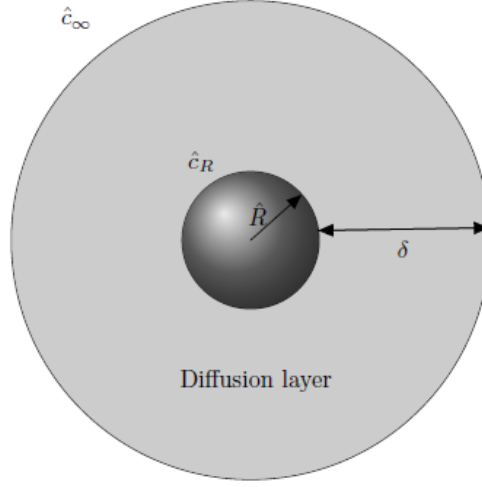


Figure 2.1: Sketch of a particle growing in a solution.

concentration of monomer diffuses in the light grey layer of depth $\delta \rightarrow \infty$, adjusting from \hat{c}_R to an equilibrium value equal to \hat{c}_∞ . In the limit $\delta \rightarrow \infty$, the problem is then governed by the classical diffusion equation

$$\frac{\partial \hat{c}}{\partial \hat{t}} = \frac{D}{\hat{r}^2} \frac{\partial}{\partial \hat{r}} \left(\hat{r}^2 \frac{\partial \hat{c}}{\partial \hat{r}} \right) \quad \text{for} \quad \hat{R}(\hat{t}) < \hat{r} < \infty, \quad (2.1)$$

describing the behaviour of the concentration $\hat{c}(r, t)$ with a constant diffusion coefficient D , and subject to the initial and boundary conditions

$$\begin{aligned} \hat{c}(\hat{R}(\hat{t}), \hat{t}) &= c_R, & \hat{t} &> 0, \\ \hat{c}(\hat{r} \rightarrow \infty, \hat{t}) &= c_\infty, & \hat{t} &> 0, \\ \hat{c}(\hat{r}, 0) &= c_\infty, & \hat{R}(t) &< \hat{r} < \infty, \end{aligned} \quad (2.2)$$

where c_R and c_∞ are constant. We are interested in the location of the moving interface, $\hat{R}(\hat{t})$, which represents the particle radius. It grows due to the diffusion of the monomer molecules from the bulk to the surface of the nanoparticles and is described by the mass balance

$$\frac{d\hat{R}}{d\hat{t}} = V_M D \frac{\partial \hat{c}}{\partial \hat{r}} \Big|_{\hat{r}=\hat{R}(\hat{t})}, \quad (2.3)$$

with the associated initial condition $\hat{R}(0) = R_0$. Note, this is equivalent to a Stefan condition in a one-phase problem. However, the Stefan condition arises through an energy balance.

In order to analyse the problem, we proceed to the nondimensionalisation of the variables, then use a small time analysis and apply several methods to find approximate and exact solutions.

The nondimensionalisation obtained using the re-scaling

$$c = \frac{\hat{c} - c_\infty}{c_\infty - c_R}, \quad r = \frac{\hat{r}}{R_0}, \quad t = \frac{\hat{t}}{\tau}, \quad (2.4)$$

substituting into equations (2.1) and (2.3), gives

$$\frac{\partial c}{\partial t} = \frac{\tau D}{R_0^2} \frac{1}{r^2} \frac{\partial}{\partial r} \left(r^2 \frac{\partial c}{\partial r} \right), \quad (2.5)$$

$$\frac{dR}{dt} = \frac{\tau V_M D (c_\infty - c_R)}{R_0^2} \frac{\partial c}{\partial r} \Big|_{r=R(t)}, \quad (2.6)$$

for the governing equation and the Stefan condition. Our interest about the change in time of the moving boundary $R(t)$ leads to choose the time scale

$$\tau = \frac{R_0^2}{V_M D (c_R - c_\infty)}, \quad (2.7)$$

and then

$$\varepsilon \frac{\partial c}{\partial t} = \frac{1}{r^2} \frac{\partial}{\partial r} \left(r^2 \frac{\partial c}{\partial r} \right), \quad (2.8)$$

$$c(R(t), t) = -1, \quad c(\infty, t) = 0, \quad c(r, 0) = 0, \quad (2.9)$$

$$\frac{dR}{dt} = \frac{\partial c}{\partial r} \Big|_{r=R(t)}, \quad R(0) = 1, \quad (2.10)$$

where the moving boundary is $R = \hat{R}/R_0$ and $\varepsilon = V_M (c_\infty - c_R)$. It has to be noticed that ε is typically very small; for example in the case of the CdSe nanoparticles growth treated in Chapters 3 and 4, the values used in [89] imply $\varepsilon = \mathcal{O}(10^{-3})$, which is a typical value in this kind of chemical processes.

2.3 Small time analysis

Looking at the initial conditions of the problem, we can notice that although at $t = 0$ the concentration is zero everywhere, as soon as the process starts we have a big jump with $c(R(t), t) = -1$. This suggests that for small times we will have a large gradient for the concentration close to the boundary. In order to understand this behaviour, we proceed with a small time analysis applying two different methods to find the exact solution.

2.3.1 Similarity solution method

Let $t = \varepsilon^\alpha \tau$ where $\varepsilon \ll 1$, we analyse the behaviour at $r \sim R(t)$ by introducing the new variable z defined by

$$r - R(t) = \varepsilon^\beta z, \quad (2.11)$$

where α and β have to be found. Putting (2.11) into the governing equation (2.8), we have

$$\varepsilon \left[\frac{1}{\varepsilon^\alpha} \frac{\partial c}{\partial \tau} \right] \approx \frac{1}{\varepsilon^{2\beta} R^2(t)} \frac{\partial}{\partial z} \left(R^2(t) \frac{\partial c}{\partial z} \right), \quad (2.12)$$

and considering $z \ll 1$, equation (2.12) leads to

$$\varepsilon^{1-\alpha+2\beta} c_\tau = c_{zz}. \quad (2.13)$$

We want $\varepsilon^{1-\alpha+2\beta} \sim 1$, that is $1 - \alpha + 2\beta = 0$. Thus, in order to look close to the border, we choose $\beta = 1$ that gives $\alpha = 3$, obtaining the classical diffusion problem described by

$$c_\tau = c_{zz}, \quad (2.14)$$

and subject to the conditions

$$c(0, \tau) = -1, \quad c(\infty, \tau) = 0, \quad c(z, 0) = 0. \quad (2.15)$$

The moving boundary is governed by the differential equation

$$R_\tau = \varepsilon^2 c_z|_{z=0} \quad (2.16)$$

where $R(0) = 1$. Equation (2.16) shows clearly that R is small at small times.

One possible solution can be found via the similarity variables method, considering the change of variable $\eta = Az\tau^\alpha$ and $c(r, \tau) = f(\eta)$. The derivatives become

$$\begin{aligned} c_\tau &= f_\eta \eta_\tau = f_\eta \alpha A z \tau^{\alpha-1}, \\ c_z &= f_\eta \eta_z = f_\eta A \tau^\alpha, \\ c_{zz} &= (c_z)_z = (f_\eta \eta_z)_z = (f_\eta A \tau^\alpha)_z = (f_\eta A \tau^\alpha)_\eta \eta_z = f_{\eta\eta} A^2 \tau^{2\alpha}. \end{aligned} \quad (2.17)$$

Substituting (2.17) into (2.14), considering the definition of η and multiplying for τ both terms, we will have the related equation

$$\alpha \eta f_\eta = A^2 t^{2\alpha+1} f_{\eta\eta}. \quad (2.18)$$

In order to remove the time dependence, we choose $\alpha = -1/2$ and $A = 1/2$, and we obtain the simple ODE

$$-2\eta f_\eta = f_{\eta\eta}. \quad (2.19)$$

Let $y = f_\eta$, then (2.19) can be written as

$$-2\eta y = y_\eta, \quad (2.20)$$

which can be easily solved by separation of variables, obtaining

$$y = C_1 e^{-\eta^2}. \quad (2.21)$$

Applying the last change of variable, we can integrate this expression and obtain

$$f(\eta) = C_1 \frac{\sqrt{\pi}}{2} \operatorname{erf}(\eta) + C_2. \quad (2.22)$$

The values for the constant of integration can be found using boundary conditions (2.15), which give $C_1 = 2/\sqrt{\pi}$ and $C_2 = -1$. Therefore, coming back to the first change of variables, the solution will be

$$c(z, \tau) = \operatorname{erf}\left(\frac{z}{2\sqrt{\tau}}\right) - 1. \quad (2.23)$$

Following the same idea, we can find an analytical solution for the moving interface since we already have an expression for the concentration. Considering that

$$c_z = f_\eta \eta_z = \frac{f_\eta}{2\sqrt{\tau}}, \quad (2.24)$$

with the same change of variables, (2.16) becomes

$$R_\tau = \frac{\varepsilon^2}{2\sqrt{\tau}} f_\eta|_{\eta=0} = \frac{\varepsilon^2}{2\sqrt{\tau}} \left(\frac{2}{\sqrt{\pi}} e^{-\eta^2} \right) \Big|_{\eta=0} = \frac{\varepsilon^2}{\sqrt{\tau\pi}}. \quad (2.25)$$

Integrating (2.25), we obtain

$$R(\tau) = 2\varepsilon^2 \sqrt{\frac{\tau}{\pi}} + C_3, \quad (2.26)$$

where C_3 is given by the initial condition $R(0) = 1$. We can notice from (2.25) that R_τ is infinite at $\tau = 0$, which is an inevitable consequence of the discontinuity in concentration at $t = 0$. However, this occurs over an infinitely small time, finally resulting in a finite R , as shown by equation (2.26). In the original coordinates, we can write the solution for the concentration and for the moving boundary

$$c(r, t) = \operatorname{erf}\left(\frac{r - R}{2} \sqrt{\frac{\varepsilon}{t}}\right) - 1, \quad R(t) = 2\sqrt{\frac{\varepsilon t}{\pi}} + 1. \quad (2.27)$$

2.3.2 Laplace transform

Another way to obtain an analytical solution is to apply the Laplace transform to the governing equations in order to obtain a much simpler problem. Hence, we define the Laplace transform of the function $c(r, t)$ as

$$\mathcal{L}\{c(r, t)\} = \int_0^\infty e^{-st} c(r, t) dt = \tilde{c}(r, s). \quad (2.28)$$

It has to be noticed in (2.28) that the variable r has to be independent. When we consider $r = R(t)$, the integral is affected. To overcome this problem, we make the assumption that $R(t)$ varies slowly with t , i.e. for $\varepsilon \rightarrow 0$. This is also confirmed if we look at the Stefan condition for small times. In fact, considering the variable change $t = \varepsilon\tau$ and noting that equation (2.3) becomes

$$\frac{dR}{d\tau} = \varepsilon \frac{\partial c}{\partial r} \Big|_{r=R(\tau)}, \quad (2.29)$$

it is reasonable to assume that $R(\tau)$ is almost constant as $\varepsilon \rightarrow 0$ and that the Laplace transform has sense at the border. Applying (2.28) to (2.8), we obtain

$$\mathcal{L}\{\partial_\tau c\} = \mathcal{L}\left\{\frac{1}{r^2} \partial_r (r^2 \partial_r c)\right\}, \quad (2.30)$$

where

$$\begin{aligned} \mathcal{L}\{\partial_\tau c\} &= \int_0^\infty e^{-s\tau} c_\tau(r, \tau) d\tau = \int_0^\infty s e^{-s\tau} c(r, \tau) d\tau + e^{-s\tau} c(r, \tau) \Big|_0^\infty \\ &= s \tilde{c}(r, s) - c(r, 0) = s \tilde{c}(r, s), \end{aligned} \quad (2.31)$$

and

$$\begin{aligned} \mathcal{L}\left\{\frac{1}{r^2} \partial_r (r^2 \partial_r c)\right\} &= \mathcal{L}\left\{\partial_{rr} c + \frac{2}{r} \partial_r c\right\} = \int_0^\infty e^{-s\tau} \left[\partial_{rr} c + \frac{2}{r} \partial_r c\right] d\tau = \\ &= \partial_{rr} \tilde{c} + \frac{2}{r} \partial_r \tilde{c} = \frac{1}{r^2} \partial_r [r^2 \partial_r \tilde{c}(r, s)], \end{aligned} \quad (2.32)$$

that gives the equation

$$\partial_{rr} \tilde{c}(r, s) + \frac{2}{r} \partial_r \tilde{c}(r, s) - s \tilde{c}(r, s) = 0. \quad (2.33)$$

The transformed boundary conditions associated to (2.9) are

$$\tilde{c}(R, s) = -\frac{1}{s}, \quad (2.34)$$

$$\tilde{c}(r \rightarrow \infty, s) = 0, \quad (2.35)$$

for $s > 0$ and neglecting the t variation in R in (2.34). The solution of the transformed equation (2.33) will be

$$\tilde{c}(r, s) = \frac{Ae^{\sqrt{s}r} + Be^{-\sqrt{s}r}}{r}, \quad (2.36)$$

where the constants A and B have to be found applying the boundary conditions. It is easy to see that condition (2.35) implies $A = 0$ and condition (2.34) implies

$$\frac{Be^{-\sqrt{s}R}}{R} = -\frac{1}{s}, \quad (2.37)$$

giving the final solution

$$\tilde{c}(r, s) = -\frac{R}{r} \left(\frac{e^{\sqrt{s}(R-r)}}{s} \right). \quad (2.38)$$

Applying the inverse Laplace transform to (2.38) we obtain

$$\mathcal{L}^{-1}\{\tilde{c}(r, s)\} = -\frac{R}{r} \operatorname{erfc} \left(\frac{r-R}{2\sqrt{\tau}} \right), \quad (2.39)$$

that gives, coming back to the original time scale,

$$c(r, t) = \frac{R(t)}{r} \left[\operatorname{erf} \left(\frac{r-R(t)}{2} \sqrt{\frac{\varepsilon}{t}} \right) - 1 \right], \quad (2.40)$$

which is exactly the same solution given by similarity variables for small times in equation (2.27) for $r \sim R(t)$. In order to find an analytical expression for the moving boundary, we can use this solution for the concentration in equation (2.39) and obtain

$$R_\tau = \varepsilon c_r|_{r=R(\tau)} = \varepsilon \left(\frac{1}{\sqrt{\pi\tau}} + \frac{1}{R(\tau)} \right). \quad (2.41)$$

Considering $R = 1 + \varepsilon R_1$ and the expansion of $\frac{1}{R}$, we can write (2.41) as

$$\varepsilon R_{1\tau} = \varepsilon \left[\frac{1}{\sqrt{\pi\tau}} + 1 - \varepsilon R_1 \right], \quad (2.42)$$

and considering just the leading order we can approximate

$$R_{1\tau} = \frac{1}{\sqrt{\pi\tau}} + 1. \quad (2.43)$$

Integrating with respect to τ and coming back to the initial change of variables, we obtain

$$R_1 = 2\sqrt{\frac{\tau}{\pi}} + \tau = 2\sqrt{\frac{\varepsilon t}{\pi}} + \varepsilon t, \quad (2.44)$$

and finally we can write the analytical solution of the moving boundary for small times as

$$R(t) = 1 + 2\sqrt{\frac{\varepsilon t}{\pi}} + \varepsilon t. \quad (2.45)$$

2.4 Exact and approximate solutions for large times

The aim of this section is to find an exact solution for large times via similarity methods and compare that with approximate solutions obtained through perturbation analysis, the heat balance integral method and numerical techniques.

2.4.1 Similarity solutions

Applying the same method of similarity variables detailed in Section 2.3.1, let $c(r, t) = f(\eta)$ where $\eta = Art^\alpha$, we can write equation (2.8) as

$$\varepsilon f_\eta \alpha Art^{\alpha-1} = A^2 t^{2\alpha} \left(f_{\eta\eta} + \frac{2}{\eta} f_\eta \right), \quad (2.46)$$

that, for definition of η and multiplying for t both terms, implies

$$\varepsilon f_\eta \alpha \eta = A^2 t^{2\alpha+1} \left(f_{\eta\eta} + \frac{2}{\eta} f_\eta \right). \quad (2.47)$$

Again, in order to remove the time dependence, we set $\alpha = -1/2$ and $A = 1/2$, and we obtain

$$-\varepsilon f_\eta \frac{\eta}{2} = \frac{1}{4} \left(f_{\eta\eta} + \frac{2}{\eta} f_\eta \right), \quad (2.48)$$

that gives

$$-2f_\eta \left(\varepsilon \eta + \frac{1}{\eta} \right) = f_{\eta\eta}, \quad (2.49)$$

where now $\eta = Art^\alpha = r/(2\sqrt{t})$. At this point, let define $y = f_\eta$ in order to obtain a first order ODE:

$$y_\eta = -2 \left(\varepsilon \eta + \frac{1}{\eta} \right) y \quad \implies \quad \int \frac{dy}{y} = -2 \int \left(\varepsilon \eta + \frac{1}{\eta} \right) d\eta, \quad (2.50)$$

that gives

$$\log(y) = -\varepsilon \eta^2 - 2 \log(\eta) + C_1 \quad \implies \quad \log(y) = \log(e^{-\varepsilon \eta^2} \eta^{-2}) + C_1, \quad (2.51)$$

and finally

$$y = C_1 e^{-\varepsilon \eta^2} \eta^{-2}. \quad (2.52)$$

Considering the definition of y , we integrate equation (2.52)

$$\int f_\eta = C_2 \int \left(e^{-\varepsilon \eta^2} \eta^{-2} \right) d\eta, \quad (2.53)$$

that gives

$$f(\eta) = -A_1 \left(\sqrt{\varepsilon\pi} \operatorname{erf}(\sqrt{\varepsilon}\eta) + \frac{e^{-\varepsilon\eta^2}}{\eta} \right) + A_2, \quad (2.54)$$

and we now adjust the boundary conditions in order to find the constants of integration. To allow A_1 and A_2 to be constant, we require $R(t) \propto \sqrt{t}$, and looking at the border condition in $\eta = R/(2\sqrt{t})$ we choose

$$R(t) = 2\lambda\sqrt{t}, \quad (2.55)$$

where λ is an unknown constant that has to be found. Conditions (2.9) lead to

$$\begin{aligned} f(\eta)|_{\eta \rightarrow \infty} = 0 & \implies -A_1\sqrt{\varepsilon\pi} + A_2 = 0, \\ f(\eta)|_{\eta=\lambda} = -1 & \implies -A_1 \left[\sqrt{\varepsilon\pi} \operatorname{erf}(\sqrt{\varepsilon}\lambda) + \frac{e^{-\varepsilon\lambda^2}}{\lambda} \right] + A_2 = -1. \end{aligned} \quad (2.56)$$

that gives

$$\begin{aligned} A_1 &= \frac{\lambda}{e^{-\varepsilon\lambda^2} - \lambda\sqrt{\varepsilon\pi} \operatorname{erfc}(\sqrt{\varepsilon}\lambda)}, \\ A_2 &= \frac{\lambda\sqrt{\varepsilon\pi}}{e^{-\varepsilon\lambda^2} - \lambda\sqrt{\varepsilon\pi} \operatorname{erfc}(\sqrt{\varepsilon}\lambda)}. \end{aligned} \quad (2.57)$$

Thus, we can define

$$A(\lambda) = \frac{\lambda}{e^{-\varepsilon\lambda^2} - \lambda\sqrt{\varepsilon\pi} \operatorname{erfc}(\sqrt{\varepsilon}\lambda)}, \quad (2.58)$$

that allows us to write the solution in the form

$$c(r, t) = A(\lambda) \left[\sqrt{\varepsilon\pi} \operatorname{erfc} \left(\frac{r}{2} \sqrt{\frac{\varepsilon}{t}} \right) - \frac{2\sqrt{t}}{r} e^{-\frac{\varepsilon r^2}{4t}} \right]. \quad (2.59)$$

From equation (2.55) we know that

$$\frac{dR}{dt} = \frac{\lambda}{\sqrt{t}}, \quad (2.60)$$

and substituting (2.60) into the Stefan condition (2.10) we have

$$\frac{\partial c}{\partial r} \Big|_{r=R(t)} = \frac{\lambda}{\sqrt{t}}. \quad (2.61)$$

According to our variables change, we have $c_r = f_\eta \eta_r$ that gives

$$\begin{aligned} \frac{\partial c}{\partial r} \Big|_{r=R(t)} &= \left[f_\eta \frac{1}{2\sqrt{t}} \right]_{\eta=\lambda} = \frac{\lambda}{e^{-\varepsilon\lambda^2} - \lambda\sqrt{\varepsilon\pi} \operatorname{erfc}(\sqrt{\varepsilon}\lambda)} \left[\frac{e^{-\varepsilon\eta^2}}{\eta^2} \right]_{\eta=\lambda} \frac{1}{2\sqrt{t}} \\ &= \frac{e^{-\varepsilon\lambda^2}}{[e^{-\varepsilon\lambda^2} - \lambda\sqrt{\varepsilon\pi} \operatorname{erfc}(\sqrt{\varepsilon}\lambda)][2\lambda\sqrt{t}]}. \end{aligned} \quad (2.62)$$

Therefore, we can write the equality between (2.60) and (2.62) and obtain

$$\frac{e^{-\varepsilon\lambda^2}}{[e^{-\varepsilon\lambda^2} - \lambda\sqrt{\varepsilon\pi} \operatorname{erfc}(\sqrt{\varepsilon}\lambda)][2\lambda\sqrt{t}]} = \frac{\lambda}{\sqrt{t}}, \quad (2.63)$$

that gives

$$2\lambda^2 - \frac{e^{-\varepsilon\lambda^2}}{e^{-\varepsilon\lambda^2} - \lambda\sqrt{\varepsilon\pi} \operatorname{erfc}(\sqrt{\varepsilon}\lambda)} = 0. \quad (2.64)$$

Finally, we obtain an equation for λ

$$2\lambda^2 \left[e^{-\varepsilon\lambda^2} - \lambda\sqrt{\varepsilon\pi} \operatorname{erfc}(\sqrt{\varepsilon}\lambda) \right] - e^{-\varepsilon\lambda^2} = 0, \quad (2.65)$$

and its solution, depending on ε , allows us to obtain the profile of $R(t)$. It has to be notice that this solution do not verify the initial condition $R(0) = 1$ and it is only valid for large times, away from the initial condition.

2.4.2 Perturbation theory

We follow the perturbation method to find an approximate solution, by starting from the exact solution of a related simpler problem. Thus, we want to approximate the concentration and the moving boundary with a function of the form

$$c = c_0 + \varepsilon c_1 + \varepsilon^2 c_2 + \dots \quad \text{and} \quad R = R_0 + \varepsilon R_1 + \varepsilon^2 R_2 + \dots \quad (2.66)$$

and divide the original problem in simpler related problems. Substituting (2.66) into (2.8) and grouping terms with the same power of ε , we obtain:

$$\mathcal{O}(\varepsilon^0) \quad \longrightarrow \quad \frac{1}{r^2} \frac{\partial}{\partial r} \left(r^2 \frac{\partial c_0}{\partial r} \right) = 0 \quad (2.67)$$

$$\mathcal{O}(\varepsilon^1) \quad \longrightarrow \quad \frac{1}{r^2} \frac{\partial}{\partial r} \left(r^2 \frac{\partial c_1}{\partial r} \right) = \frac{\partial c_0}{\partial t} \quad (2.68)$$

$$\mathcal{O}(\varepsilon^2) \quad \longrightarrow \quad \frac{1}{r^2} \frac{\partial}{\partial r} \left(r^2 \frac{\partial c_2}{\partial r} \right) = \frac{\partial c_1}{\partial t} \quad (2.69)$$

$$\mathcal{O}(\varepsilon^3) \quad \longrightarrow \quad \dots \quad (2.70)$$

The related non zero boundary condition then becomes

$$c(R, t) = c_0(R_0 + \varepsilon R_1 + \dots, t) + \varepsilon c_1(R_0 + \varepsilon R_1 + \dots, t) + \dots \quad (2.71)$$

$$= c_0(R_0, t) + \varepsilon R_1 \frac{\partial c_0}{\partial r} \Big|_{r=R_0} + \varepsilon c_1(R_0, t) + \dots = -1. \quad (2.72)$$

which gives

$$\begin{aligned} c_0(R, t) = -1, \quad c_0(\infty, t) = 0, \quad c_i(R, t) = c_i(\infty, t) = 0 \quad \text{for } i = 1, 2, \dots \\ R_0(0) = 1, \quad R_i(0) = 0 \quad \text{for } i = 1, 2, \dots \end{aligned} \quad (2.73)$$

From the first order (2.67) and boundary conditions (2.73), we can write

$$c_0(r, t) = -\frac{R_0(t)}{r}. \quad (2.74)$$

Therefore, using equation (2.74), the lower order of the Stefan condition will be

$$\frac{dR_0}{dt} = \frac{\partial c_0}{\partial r} \Big|_{r=R_0} = \frac{1}{R_0}, \quad (2.75)$$

which gives the solution for the moving boundary profile

$$R_0(t) = \sqrt{2t + 1}, \quad (2.76)$$

where the initial condition $R_0(0) = 1$ has been applied. In order to solve the equation for $\mathcal{O}(\varepsilon)$, we can use the solution (2.74) and the Stefan condition in order to write

$$\frac{\partial c_0}{\partial t} = -\frac{1}{r} \frac{dR_0}{dt} = -\frac{1}{r} \left(\frac{\partial c_0}{\partial r} \Big|_{r=R_0} \right) = -\frac{1}{rR_0}. \quad (2.77)$$

Substituting (2.77) into (2.68) and integrating twice, we obtain

$$c_1(r, t) = \frac{1}{2} \left(1 - \frac{r}{R_0} \right) + A \left(\frac{1}{R_0} - \frac{1}{r} \right), \quad (2.78)$$

where the left boundary condition in (2.73) has been used and A is a constant that has to be found applying the right boundary condition. However, we can observe that (2.78) explodes as $r \rightarrow \infty$ suggesting that we can only use this solution at $r \sim R$, and we should rescale variables for large values of r .

2.4.3 Heat Balance Integral Method

For an alternative theoretical study of the function, we apply the heat balance integral method, which was initially proposed by Goodman in the late 1950s in order to solve thermal problems [44]. The HBIM is used to find approximate solutions to heat equation and Stefan problems, where very few analytical solution can be found. Essentially, it follows three steps:

1. The introduction of a parameter δ that represents the diffusion depth: for $r \geq \delta$ the concentration change is negligible and hence $c(\delta, t) = 0$ and $c_r(\delta, t) = 0$.
2. The definition of an approximate function dependent on δ and appropriate boundary conditions.
3. The integration of the governing equation to produce the heat balance integral that gives an ordinary differential equation for δ .

In order to simplify the diffusion equation (2.8), we also consider the change of variable $c = u/r$ and obtain the related system:

$$\varepsilon \frac{\partial u}{\partial t} = \frac{\partial^2 u}{\partial r^2}, \quad u(r, 0) = 0, \quad R(t) < r < \delta, \quad t > 0, \quad (2.79)$$

$$u(R(t), t) = -R(t), \quad u(\delta, t) = 0, \quad t > 0, \quad (2.80)$$

$$R(t) \frac{dR}{dt} = \frac{\partial u}{\partial r} \Big|_{r=R(t)} + 1, \quad R(0) = 1, \quad t > 0. \quad (2.81)$$

As suggested in [73], we assume that the approximate function u is a polynomial of the form

$$u(r, t) = a_0 + a_1 \left(\frac{\delta - r}{\delta - R(t)} \right) + a_2 \left(\frac{\delta - r}{\delta - R(t)} \right)^n, \quad (2.82)$$

where the coefficients a_0 , a_1 and a_2 may depend on time and δ is the diffusion thickness.

Using the boundary condition (2.80) at $r = \delta$, we have:

$$\begin{aligned} u(\delta, t) = 0 &\implies a_0 = 0, \\ \frac{\partial u}{\partial r} \Big|_{r=\delta} = 0 &\implies a_1 = 0. \end{aligned} \quad (2.83)$$

Moreover, evaluating (2.82) at $r = R$, we have

$$u(R(t), t) = a_2 = -R(t), \quad (2.84)$$

that gives the final approximating function:

$$u(r, t) = -R(t) \left(\frac{\delta - r}{\delta - R(t)} \right)^n. \quad (2.85)$$

In order to find the behaviour of δ and R , we consider the heat balance integral

$$\int_{R(t)}^{\delta} \varepsilon \frac{\partial u}{\partial t} dr = \int_{R(t)}^{\delta} \frac{\partial^2 u}{\partial r^2} dr, \quad (2.86)$$

that gives

$$\int_{R(t)}^{\delta} \varepsilon \frac{\partial u}{\partial t} dr = \left[\frac{\partial u}{\partial r} \Big|_{r=\delta} - \frac{\partial u}{\partial r} \Big|_{r=R(t)} \right]. \quad (2.87)$$

Putting (2.85) into the right side of (2.87), we have that $\frac{\partial u}{\partial r} \Big|_{r=\delta} = 0$ and

$$\frac{\partial u}{\partial r} \Big|_{r=R(t)} = \frac{nR(t)(\delta - r)^{n-1}}{(\delta - R(t))^n} \Big|_{r=R(t)} = \frac{nR(t)}{\delta - R(t)}. \quad (2.88)$$

Moreover, for Leibniz's theorem, we have

$$\begin{aligned} \frac{d}{dt} \int_{R(t)}^{\delta} \varepsilon u(r, t) dr &= \varepsilon \left[\frac{d\delta}{dt} u(\delta, t) - \frac{dR}{dt} u(R(t), t) + \int_{R(t)}^{\delta} \frac{\partial u}{\partial t} dr \right] \\ &= \varepsilon \left\{ \frac{dR}{dt} R(t) + \int_{R(t)}^{\delta} \frac{\partial u}{\partial t} dr \right\}, \end{aligned} \quad (2.89)$$

where (2.80) is being applied. Therefore, (2.89) gives

$$\int_{R(t)}^{\delta} \varepsilon \frac{\partial u}{\partial t} dr = \frac{d}{dt} \int_{R(t)}^{\delta} \varepsilon u(r, t) dr - \varepsilon \frac{dR}{dt} R(t). \quad (2.90)$$

We can write the second integral as

$$\begin{aligned} \int_{R(t)}^{\delta} \varepsilon u(r, t) dr &= \varepsilon \int_{R(t)}^{\delta} \left[-R(t) \left(\frac{\delta - r}{\delta - R(t)} \right)^n \right] dr = -\frac{\varepsilon R(t)}{(\delta - R(t))^n} \left[-\frac{(\delta - r)^{n+1}}{n+1} \right]_{R(t)}^{\delta} \\ &= -\frac{\varepsilon R(t)(\delta - R(t))}{n+1}, \end{aligned} \quad (2.91)$$

and obtain the equation

$$\frac{d}{dt} \left[\frac{\varepsilon R(t)(\delta - R(t))}{n+1} \right] + \varepsilon \frac{dR}{dt} R(t) = \frac{nR(t)}{\delta - R(t)}. \quad (2.92)$$

Using the Stefan condition (2.81) we finally obtain the ODEs system

$$\frac{dR}{dt} = \frac{n}{\delta - R(t)} + \frac{1}{R(t)}, \quad (2.93)$$

$$\frac{d\delta}{dt} = \frac{[\varepsilon(n-1)^2 - n^2 - n] R^2(t) + 2\varepsilon\delta(n-1)R(t) + \varepsilon\delta^2}{R^2(t)(R(t) - \delta)\varepsilon}, \quad (2.94)$$

with the initial conditions $R(0) = \delta(0) = 1$. In fact, at the beginning, diffusion does not occur and consequently the thickness initial condition correspond to the initial value of the radius. In order to avoid the singularity at the initial point, we proceed with a small time analysis and suppose that

$$R(t) = 1 + 2\nu\sqrt{t}. \quad (2.95)$$

Putting this expression into the Stefan condition (2.93) we obtain

$$(1 + 2\nu\sqrt{t}) \frac{d}{dt} (1 + 2\nu\sqrt{t}) = \frac{n(1 + 2\nu\sqrt{t})}{\delta - R(t)} + 1, \quad (2.96)$$

that gives

$$(1 + 2\nu\sqrt{t}) \frac{\nu}{\sqrt{t}} = \frac{n(1 + 2\nu\sqrt{t})}{\delta - (1 + 2\nu\sqrt{t})} + 1. \quad (2.97)$$

Thus, the term $(\delta - R)$ has to balance the factor \sqrt{t} , e.g. we suppose that

$$\delta = 1 + 2\mu\sqrt{t}, \quad (2.98)$$

obtaining

$$\nu = \frac{n}{2(\mu - \nu)}, \quad (2.99)$$

that gives

$$\mu = \nu + \frac{n}{2\nu}. \quad (2.100)$$

Putting (2.95) and (2.98) into the HBIM equation, we obtain

$$\varepsilon \left[\frac{d}{dt} \left(\frac{(1 + 2\nu\sqrt{t})(2(\mu - \nu)\sqrt{t})}{n + 1} \right) + \frac{\nu}{\sqrt{t}}(1 + 2\nu\sqrt{t}) \right] = \frac{n(1 + 2\nu\sqrt{t})}{2(\mu - \nu)\sqrt{t}}, \quad (2.101)$$

and due to the fact that $t \ll 1$, we can approximate this expression as

$$\varepsilon \left[\frac{d}{dt} \left(\frac{2(\mu - \nu)\sqrt{t}}{n + 1} \right) + \frac{\nu}{\sqrt{t}} \right] = \frac{n}{2(\mu - \nu)\sqrt{t}}, \quad (2.102)$$

that leads to

$$\varepsilon \left[\frac{n}{2\nu(n + 1)} + \nu \right] = \nu, \quad (2.103)$$

where (2.100) has been used to substitute μ . We can finally write an expression for ν as

$$\nu = \sqrt{\frac{\varepsilon n}{2(1 - \varepsilon)(n + 1)}}, \quad (2.104)$$

that gives

$$R = 1 + \sqrt{\frac{\varepsilon n t}{2(1 - \varepsilon)(n + 1)}}. \quad (2.105)$$

Putting (2.104) into (2.100) we have

$$\mu = \frac{n[(1 - \varepsilon)n - 1]}{\sqrt{2(1 - \varepsilon)(n + 1)\varepsilon n}}, \quad (2.106)$$

hence

$$\delta = 1 + \frac{n[(1-\varepsilon)n-1]\sqrt{t}}{\sqrt{2(1-\varepsilon)(n+1)\varepsilon n}}. \quad (2.107)$$

Thanks to this analysis we can choose an initial value for R and δ at $t_0 \ll 1$ and calculate the approximate solution of (2.93)–(2.94) using the MATLAB in-built function `ode45`. The issue is understand which is the best choice for n in the approximate function. Langford [60] proposed a definition of an error for the HBIM method through the integral of the energy. Myers [78] used this definition to minimize the error leaving the exponent unknown. Applying this strategy to our problem we obtain that the error

$$E_n(t) = \int_R^\delta \left[\varepsilon \frac{\partial u}{\partial t} - \frac{\partial^2 u}{\partial r^2} \right]^2 dr \quad (2.108)$$

is minimized for $n = 3.7$.

2.4.4 Numerical approximation

As we have to deal with a numerical approximation, we introduce a constant δ_f that represents the diffusion depth as in Section 2.4.3. We transform the system (2.79)–(2.81) fixing the boundary through the change of variables

$$\eta = \frac{r - R}{\delta_f - R}, \quad \tau = t, \quad (2.109)$$

obtaining the equivalent system

$$\varepsilon \frac{\partial u}{\partial \tau} = \varepsilon \frac{dR}{d\tau} \left(\frac{1 - \eta}{R - \delta_f} \right) \frac{\partial u}{\partial \eta} + \frac{1}{(R - \delta_f)^2} \frac{\partial^2 u}{\partial \eta^2}, \quad 0 < \eta < 1, \quad (2.110)$$

$$u(0, \tau) = -R, \quad u(1, \tau) = 0, \quad u(\eta, 0) = 0, \quad (2.111)$$

$$R \frac{dR}{d\tau} = \frac{1}{(R - \delta_f)} \frac{\partial u}{\partial \eta} \Big|_{\eta=0} + 1, \quad R(0) = 1. \quad (2.112)$$

Let define the discrete variables in space and time

$$\begin{aligned} \eta_j &= j\Delta\eta & \text{for } j &= 0, \dots, J, \\ t_n &= n\Delta\tau & \text{for } n &= 0, \dots, N. \end{aligned} \quad (2.113)$$

Thus, considering the notation $u_j^n = u(\eta_j, t^n)$, we approximate the diffusion equation (2.110) using first order Euler for the time derivative and central difference for the spatial derivatives, as:

$$\frac{\partial u}{\partial \tau} \approx \frac{u_j^{n+1} - u_j^n}{\Delta\tau}, \quad \frac{\partial u}{\partial \eta} \approx \frac{u_{j+1}^n - u_{j-1}^n}{2\Delta\eta}, \quad \frac{\partial^2 u}{\partial \eta^2} \approx \frac{u_{j+1}^n - 2u_j^n + u_{j-1}^n}{\Delta\eta^2}. \quad (2.114)$$

The behaviour of the boundary is given by forward difference in time and the three-term backward difference of the solution, i.e.

$$\frac{dR}{d\tau} \approx \frac{R^{n+1} - R^n}{\Delta\tau}, \quad \left. \frac{\partial u}{\partial \eta} \right|_{\eta=0} \approx \frac{3u_1^n - 4u_2^n + u_3^n}{2\Delta\eta}. \quad (2.115)$$

Hence, equation (2.110) can be approximated as

$$\begin{aligned} \varepsilon \left(\frac{u_j^{n+1} - u_j^n}{\Delta\tau} \right) = & \varepsilon \left(\frac{R^{n+1} - R^n}{\Delta\tau} \right) \left(\frac{1 - \eta_j}{R^n - \delta_f} \right) \left(\frac{u_{j+1}^n - u_{j-1}^n}{2\Delta\eta} \right) \\ & + \frac{1}{(R^n - \delta_f)^2} \left(\frac{u_{j+1}^n - 2u_j^n + u_{j-1}^n}{\Delta\eta^2} \right), \end{aligned} \quad (2.116)$$

where

$$R^{n+1} = \frac{\Delta\tau}{R^n(R^n - \delta_f)} \left(\frac{3u_1^{n+1} - 4u_2^{n+1} + u_3^{n+1}}{2\Delta\eta} \right) + \frac{\Delta\tau}{R^n} + R^n, \quad (2.117)$$

subject to $R^1 = 1$. Multiplying (2.116) by $(R^n - \delta_f)^2 \Delta\tau$, defining $\nu = \Delta\tau/2\Delta\eta$ and $\mu = \Delta\tau/\Delta\eta^2$, we can write the scheme as

$$a^{n+1}u_{j-1}^{n+1} + b^{n+1}u_j^{n+1} + d^{n+1}u_{j+1}^{n+1} = e^n u_j^n, \quad (2.118)$$

where

$$\begin{aligned} a^{n+1} &= \varepsilon(R^n - \delta_f)(1 - \eta_j)\nu R_\tau^{n+1} - \mu, \\ b^{n+1} &= \varepsilon(R^n - \delta_f)^2 + 2\mu, \\ d^{n+1} &= -\varepsilon(R^n - \delta_f)(1 - \eta_j)\nu R_\tau^{n+1} - \mu, \\ e^n &= \varepsilon(R^n - \delta_f)^2. \end{aligned} \quad (2.119)$$

Boundary and initial conditions can be written as

$$u_0^{n+1} = -R^n, \quad u_J^{n+1} = 0, \quad u_i^1 = \delta\eta_i + 1. \quad (2.120)$$

We can write the system in the matrix form

$$M^n U^{n+1} = U^n, \quad (2.121)$$

for $n = 1, \dots, T-1$, which expanded becomes

$$\begin{pmatrix} a_1^{n+1} & b_1^{n+1} & d_1^{n+1} & 0 & \dots & \dots & 0 \\ a^{n+1} & b^{n+1} & d^{n+1} & 0 & \dots & \dots & 0 \\ 0 & a^{n+1} & b^{n+1} & d^{n+1} & 0 & \dots & 0 \\ 0 & 0 & \ddots & \ddots & \ddots & \dots & 0 \\ 0 & \dots & \dots & \dots & a^{n+1} & b^{n+1} & d^{n+1} \\ 0 & \dots & \dots & \dots & \dots & 0 & 1 \end{pmatrix} \begin{pmatrix} u_1^{n+1} \\ u_2^{n+1} \\ \vdots \\ \vdots \\ u_{J-1}^{n+1} \\ u_J^{n+1} \end{pmatrix} = \begin{pmatrix} e_1^{n+1} \\ e^n u_2^n \\ \vdots \\ \vdots \\ e^n u_{J-1}^n \\ e_J^{n+1} \end{pmatrix}. \quad (2.122)$$

At each time we solve the system (2.121) and we use the solution U^{n+1} to solve the Stefan condition (2.117).

2.5 Results

The approximations described in this chapter are compared in Figure 2.2 for $\varepsilon = 0.01$. In Figure 2.2(a) we can observe the behaviour of the solutions for the concentration at a fixed time \bar{t} . The image shows good agreement between the similarity solution (2.59) where $\lambda = 0.75$, the numerical approximation given by solving (2.121) and the HBIM method obtained from re-scaling (2.85) with $n = 3.7$. In particular, the latter two are almost undistinguishable. On the other hand, in Figure 2.2(b) the profile for the radius shows the limits of some methods. While there is an excellent agreement between the numerical solution given by (2.117) and the HBIM approximation (2.93), it is clearly shown the invalidity of the similarity solution described in (2.55) for small times.

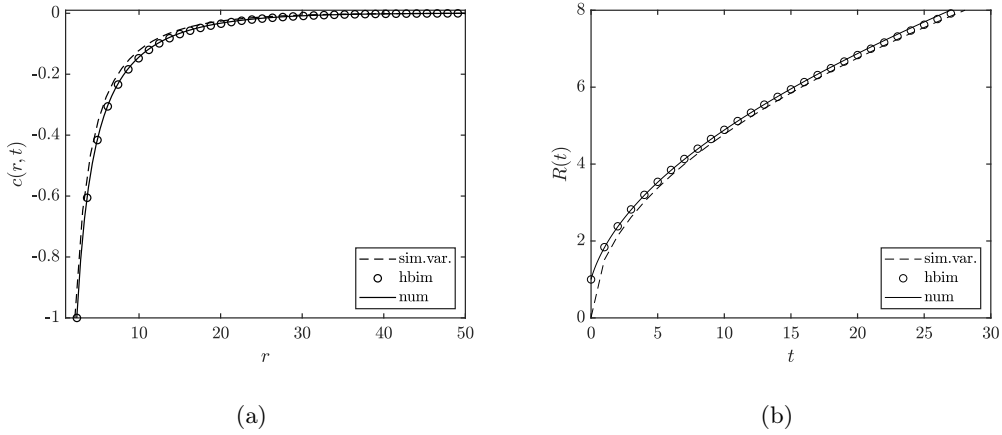


Figure 2.2: Comparison of (a) the concentration and (b) the particle radius profiles given by the similarity variables method (dashed line), the HBIM (dots) and the numerical approximation (solid line) with $\varepsilon = 0.01$.

3 | A model for colloidal, spherical crystal growth

T. G. Myers, C. Fanelli.

On the incorrect use and interpretation of the model for colloidal, spherical crystal growth.

Journal of Colloid and Interface Science, 536, pp. 98–104 (2019).

Impact factor: 6.361

Abstract

We examine the standard model for diffusion and surface kinetics driven growth of a single spherical particle in solution and show that it is applied incorrectly throughout the literature. It is shown that crystal growth occurs in two distinct stages: an early time where the growth rate is large and a late time, when the rate decreases. The definition of 'early' depends on the particular experiment, but may be of the order of hundreds of seconds. It is only during the late time that the standard model holds. Authors typically fit the model to all experimentally obtained growth data however since it is invalid in the early time stage this leads to incorrect values for the diffusion and surface kinetic coefficients. In fact the model cannot even distinguish between diffusion or surface kinetics driven growth, although the majority of authors assume one or the other to be the dominant driving force: since the model cannot distinguish either assumption leads to equally good results. Applying the model correctly shows that the growth is controlled by a single non-dimensional group: practically this means that the growth data may only be

used to predict a single unknown. Previous studies, where 2, 3 or 4 parameters were calculated have redundancy. The Gibbs-Thomson relation plays an important role but, in the cases studied here it has a noticeable effect only during the first growth stage where the model does not hold. On a more positive note, we finish by providing an explicit relation for the variation of the radius with time. This is the first such relation in the literature and, for large times with just a single fitting parameter, excellent agreement with experimental data on CdSe nanocrystal growth is demonstrated.

3.1 Introduction

Nanocrystals or chemically grown quantum dots have a wealth of uses, such as in solar cells, light emitting diodes, biological markers, optoelectronic devices and nanoelectronics [24, 71, 102]. It is estimated that semiconductor quantum dots may have a market value of over \$4 billion by 2020 [15]. Since nanocrystal properties are tunable by adjusting their size and/or shape it is essential to be able to prepare monodisperse particles in a reproducible manner. To do this requires a clear understanding of the growth process, yet surprisingly there is a lack of theoretical understanding for the process of growing nanocrystals in colloidal solutions [104] and consequently production is still primarily carried out via small batch processes and trial and error [15].

In this paper we study the standard model for colloidal spherically symmetric crystal growth. Obviously this has application in a multitude of synthetic growth processes, however we will focus primarily on the nanoscale due to the current high interest in this field. LSW theory [7] is currently the most popular theoretical method to describe the colloidal crystal growth process. The initial stage of this theory is to apply a kinetic model, whereby the growth rate of each crystal depends on the local solute concentration, diffusion rate and surface kinetics. Mathematically this leads to a diffusion equation in the solute, coupled to a mass balance which describes the growth rate of the crystal. The growth rate obtained through this analysis is then introduced into a continuity equation to calculate the particle size distribution. With multiple particles it is possible to predict Ostwald ripening or size focussing and to identify the key parameters controlling the process. It is therefore essential to understand and to correctly apply the basic building block, the kinetic model,

and for this reason it is discussed in detail by many authors. Sugimoto [103] uses the kinetic model to provide a detailed theoretical and practical discussion of crystal growth. Peng *et al.* [89] focus solely on the context of nanocrystal growth. In several nanocrystal studies [7, 17, 23, 24, 71, 102, 104] the kinetic model is typically solved, subject to various assumptions, to obtain an expression for $t(r)$ (the change of time with radius, since the function cannot be inverted to $r(t)$) and then the diffusion and surface kinetic coefficients obtained via comparison with experimental data. All are able to obtain good agreement to the data despite the fact different driving mechanisms (diffusion/surface kinetics) are assumed to dominate and distinct growth regimes are observed. This means that different numbers of fitting parameters are used in the various studies.

3.2 Growth of a single particle

We now focus on the typical scenario involving a single, spherical nanoparticle, with radius r_p . We assume the standard La Mer model [58] which is based on temporal separation between nucleation and growth and then model only the period of particle growth. The system is dilute, such that particle interaction and aggregation are neglected. The growth is always spherically symmetric, i.e. we average the typical atom by atom growth: this assumption becomes more reasonable as the size increases. The affect of any solvent used to facilitate the growth process is accounted for by the diffusion and or kinetic rate constant. The monomer concentration at the particle surface and in the far-field are C_i and C_b , respectively. The particle solubility, C_s is given by the Gibbs-Thomson (or Ostwald-Freundlich) relation

$$C_s = C_\infty \exp \left\{ \left(\frac{\alpha}{r_p} \right) \right\}, \quad (3.1)$$

where α is the capillary length and C_∞ is the bulk solubility of the particle, i.e. when $r_p \rightarrow \infty$. If $C_s < C_b$ then monomer molecules diffuse from the bulk towards the particle to react with the surface and the particle grows, whereas if $C_s > C_b$ the particle shrinks.

The monomer concentration, C , is described by the diffusion equation

$$\frac{\partial C}{\partial t} = \frac{D}{r^2} \frac{\partial}{\partial r} \left(r^2 \frac{\partial C}{\partial r} \right), \quad (3.2)$$

where r is distance from the centre of the particle and t is time. This is subject to

$$C(r_p, t) = C_i(t), \quad C(r_p + \delta, t) = C_b(t), \quad C(r, 0) = C_0 \quad \text{for } r > r_p, \quad (3.3)$$

where the last condition states that initially the monomer solution is well-mixed and at a uniform concentration, C_0 . To conform with standard literature (see Refs. [69, 103, 108]), we have included a diffusion layer of width δ around the particle, where the concentration adjusts from C_i to C_b .

In practice the concentration adjacent to the particle surface, C_i , is difficult to measure. It may be eliminated from the model by considering two equivalent expressions for the mass flux at the particle surface, J . Fick's first law relates the flux of monomers passing through a spherical surface of radius r to the concentration gradient

$$J = 4\pi r^2 D \frac{\partial C}{\partial r} = \frac{4\pi D r_p (r_p + \delta)}{\delta} (C_b - C_i), \quad (3.4)$$

where D is the constant diffusion coefficient. Invoking a first-order surface reaction, the flux is also proportional to the difference between monomer concentration adjacent to the particle and the particle surface concentration

$$J = 4\pi r_p^2 k (C_i - C_s), \quad (3.5)$$

where k is a rate constant. Equating (3.4) with (3.5) gives

$$C_i = C_s + \frac{D}{k} \frac{\partial C}{\partial r} \bigg|_{r=r_p}, \quad (3.6)$$

which defines the concentration C_i for the surface condition of (3.3).

The diffusion equation must be solved on a domain $r > r_p$, where the particle radius is an unknown function of time. To determine the radius we impose the mass balance

$$\frac{d}{dt} \left(\frac{4}{3} \pi r_p^3 \right) = 4\pi r_p^2 \frac{dr_p}{dt} = V_m J, \quad (3.7)$$

which upon substituting for J (at $r = r_p$) yields

$$\frac{dr_p}{dt} = V_M D \frac{\partial C}{\partial r} \bigg|_{r=r_p}, \quad r_p(0) = r_{p0}, \quad (3.8)$$

where $r_{p0} > 0$ is the initial particle radius.

To complete the system we require an expression for the time-dependent bulk concentration, $C_b(t)$. The volume of solute per particle is $1/N_0$, where N_0 is the population density. A mass balance within the volume surrounding a particle gives

$$\frac{1}{N_0} M_p C_0 = M_p C_b(t) \left(\frac{1}{N_0} - \frac{4\pi}{3} r_p^3 \right) + \frac{4\pi}{3} \rho_p r_p^3, \quad (3.9)$$

where M_p is molar mass. On the left hand side is the total amount of monomer initially in the solute, before nucleation has occurred. The first term on the right hand side represents the amount of monomer at time t , but now the volume occupied by monomer is the original value minus the space taken up by the nanocrystal. Finally, monomer has been used to create a nanocrystal with density ρ_p , which is the final term. LSW theory is valid for dilute systems, where particle-particle interaction is negligible, which means that $4\pi r_p^3 N_0/3 \ll 1$ (this is easily verified using the values of Table 3.1). Noting that $V_M = M_p/\rho_p$ we obtain

$$C_b(t) \approx C_0 - \frac{4\pi}{3} \frac{\rho_p}{M_p} N_0 r_p^3 = C_0 - \frac{4\pi}{3} \frac{N_0}{V_M} r_p^3. \quad (3.10)$$

The system is now fully defined: monomer concentration is described by equation (3.2), subject to the boundary conditions (3.3) and holds for $r > r_p(t)$ where r_p satisfies (3.8), the bulk concentration required for the boundary conditions is given by (3.10). Mathematically the problem is analogous to the melting or solidification of a spherical nanoparticle, as described in Refs. [36, 93], where the melt temperature is a function of the radius (following the Gibbs-Thomson relation). It is well-known from this theory that even for simple configurations there is no analytical solution and so approximate or numerical solutions are required.

3.2.1 Pseudo-steady state solution

The pseudo-steady state approximation is simply obtained by neglecting the time derivative in (3.2) and integrating the resultant ordinary differential equation:

$$C = C_b + \frac{k r_p^2}{D(r_p + \delta) + k \delta r_p} [C_b - C_s] \left(1 - \frac{r_p + \delta}{r} \right). \quad (3.11)$$

The ‘constants’ of integration (which may be time-dependent since the integration is with respect to r) come from applying the boundary conditions in (3.3) and replacing C_i from

(3.6). The concentration $C_s(t)$ is defined by the Gibbs-Thomson equation (3.1) and $C_b(t)$ by equation (3.10). The growth rate of the particle comes from equation (3.8)

$$\begin{aligned} \frac{dr_p}{dt} &= V_M D \frac{k(r_p + \delta)}{D(r_p + \delta) + k\delta r_p} (C_b - C_s) \\ &= D \frac{k(r_p + \delta)}{D(r_p + \delta) + k\delta r_p} \left[V_M (C_0 - C_\infty e^{\alpha/r_p}) - b^3 r_p^3 \right], \end{aligned} \quad (3.12)$$

where $b^3 = 4\pi N_0/3$.

Equation (3.11) describes the evolution of the concentration over time, it contains the unknown δ , which represents the width of the adjustment zone where the concentration increases from the particle edge to the bulk value. This is more commonly termed the boundary layer. Diffusion boundary layers are time-dependent and, if the fluid is initially well-mixed, $\delta(0) = 0 < r_p$. In the pseudo-steady approximation there is no way to calculate $\delta(t)$. It may only be obtained via a full time dependent calculation (numerical) or certain approximation techniques, see Ref. [78]. The growth equation (3.12) also contains $\delta(t)$, consequently in its present form the pseudo-steady solution is of no practical use.

3.3 Standard solution method

To permit a tractable mathematical model a number of assumptions are made in the literature, these include: pseudo-steady state diffusion; a diffusion layer thickness which is significantly greater than the particle size; neglect of the Gibbs-Thomson relation (resulting in a constant particle solubility) [7, 110]. The first two assumptions are so widely accepted that they are usually stated regardless of the experimental procedure, then analysis proceeds without discussion of their validity. We will investigate when these assumptions are reasonable in a later section.

Following the pseudo-steady assumption, setting $\delta \gg r_p$ and taking $C_{eq} = C_\infty e^{\alpha/r_p}$ to be constant leads to

$$C = C_b + \frac{kr_p^2}{(D + kr_p)\delta} [C_b - C_{eq}] \left(1 - \frac{\delta}{r} \right) \quad (3.13)$$

$$\frac{dr_p}{dt} = \frac{Dk}{D + kr_p} [a^3 - b^3 r_p^3], \quad (3.14)$$

where $a^3 = V_M(C_0 - C_{eq})$. Integration of equation (3.14) leads to an implicit equation for $t(r)$

$$t - t_0 = \frac{1}{6a^2b^2Dk} \left[(bD + ak) \left\{ \ln \frac{a^2 + abr_p + b^2r_p^2}{(a - br_p)^2} - \ln \frac{a^2 + abr_{p0} + b^2r_{p0}^2}{(a - br_{p0})^2} \right\} \right. \\ \left. + 2\sqrt{3}(bD - ak) \left\{ \arctan \left(\frac{a + 2br_p}{\sqrt{3}a} \right) - \arctan \left(\frac{a + 2br_{p0}}{\sqrt{3}a} \right) \right\} \right]. \quad (3.15)$$

The governing equations of this section and the solution (3.15) are quoted in numerous papers on nanocrystal growth, see Refs. [17, 23, 71, 102] for example, but here we have explicitly written down the contribution of the initial condition, such that $t(r_{p0}) = t_0$. We refrain from specifying $t_0 = 0$ since a number of authors report the growth occurring in two distinct stages, then t_0 could represent the start time of the second stage and $r_p(t_0) = r_{p0}$ the corresponding particle radius. As is frequently stated this equation cannot be inverted in order to express $r(t)$.

A list of typical values used in the standard model or obtained by fitting to experimental data is provided in Table 3.1. Numbers in bold have been estimated from figures in the respective papers or calculated. If we take the example of Chuang *et al.* [23], they have graphs for Cd in $\mu\text{mol/g}$, we convert this to mol/m^3 by multiplying by the solution density 0.9g/cm^3 . Their graph, Fig. 4, shows a maximum $C_0 \approx 10.5 \mu\text{mol/g} = 9.45 \text{ mol/m}^3$. The final concentration, when growth has stopped, is $C_{eq} \approx 0.08 \text{ mol/m}^3$. From this we calculate $a^3 = V_M(C_0 - C_{eq}) \approx 3.1 \times 10^{-4}$. Their experimental maximum radius $r_m = 2.89\text{nm}$ where $r_m = a/b$, hence $b^3 = 1.28 \times 10^{22}$. To determine C_∞ requires the value of the capillary length $\alpha = 2\sigma V_M/(R_G T)$, which is calculated using the values quoted in [89]: $\sigma = 0.44\text{J/m}^2$, $R_G = 8.31 \text{ J/mol/K}$, $V_M = 3.3 \times 10^{-5} \text{ m}^3/\text{mol}$ and the temperatures provided in the table then $C_\infty = C_{eq}e^{-\alpha/r_m}$. The values of N_0 (init.) are the numbers quoted in the paper, usually estimated from a concentration curve, the value N_0 (fin.) is calculated from the value of $b^3 = 4\pi N_0/3$ obtained by fitting to experimental data. For Ref. [102] we only present data for their "curve 2". The choice of region is discussed later.

3.4 Diffusion and kinetics driven cases

Various authors have assumed that the process is driven solely by diffusion or surface kinetics, which leads to a slightly simpler solution form. In either case during the derivation of equation (3.14) the number of expressions for the flux is reduced which then

Param./Units	Su [102]	Chuang [23]	Pan [85]	Bullen [17]
N_0 (init.) [No. m^{-3}]	3.92×10^{22}	4.8×10^{21}	-	-
N_0 (fin.) [No. m^{-3}]	8.19×10^{22}	3.02×10^{22}	3.19×10^{21}	4.6×10^{22}
C_0 [mol m^{-3}]	-	9.45	2.5	50
C_{eq} [mol m^{-3}]	-	8×10^{-2}	6.1×10^{-4}	3.29
C_∞ [mol m^{-3}]	-	7.9×10^{-3}	8.95×10^{-6}	0.131
a^3 [1]	6.59×10^{-5}	3.1×10^{-4}	8.25×10^{-5}	1.54×10^{-3}
b^3 [m^{-3}]	3.43×10^{22}	1.28×10^{22}	1.34×10^{22}	1.93×10^{23}
D [$\text{m}^2 \text{s}^{-1}$]	9.10×10^{-18}	1.5×10^{-16}	no D	no D
k [m s^{-1}]	7.97×10^{-9}	no k	9.74×10^{-10}	2.2×10^{-8}
T [K]	503	523	473	538
r_m [nm]	1.24	2.89	1.75	2.015
α [nm]	6.95	6.68	7.39	6.5

Table 3.1: Comparison of the parameters for nanocrystal growth in different studies.

prevents the determination of the unknown concentration, C_i , required in the boundary condition.

In the diffusion limited case there can be no flux due to surface reaction, this requires either setting $C_i = C_{eq}$ or $k = 0$. Setting $k = 0$ in (3.14) leads to zero growth, hence the diffusion limit can only be theoretically achieved by adjusting the concentration. That is, for purely diffusion driven growth the value of the concentration in the solute adjacent to the particle must be exactly equal to the equilibrium concentration of the particle throughout the process. In the surface reaction driven case the diffusion term tends to zero provided $C_i = C_b$ or $D = 0$. Again we may immediately rule out $D = 0$ and so in this case the value of C_i must be exactly the bulk concentration throughout the process. Further, equation (3.4) indicates that if $C_b = C_i$ then $\partial C / \partial r = 0$ and hence $C = C_b$ everywhere: the surface kinetics limit requires that the concentration is constant in space throughout the process. From this point of view it seems clear that the reductions are physically unrealistic. However, if we do apply them then the surface reaction driven solution of Refs. [17, 85, 102] is obtained by setting $ak = 0$ in (3.15), the diffusion driven solution of Refs. [23, 71, 102] is obtained

by setting $bD = 0$.

3.5 Validity of the assumptions

The particle growth and solute concentration equations form the basis of LSW theory [7]. To correctly describe nanocrystal growth and Ostwald ripening and so better control the process it is essential that the governing equations are correctly derived and analysed. In the following we will highlight a number of errors common to the literature and show how they may be corrected and interpreted. Finally we illustrate the conclusions by comparison with experimental data.

The pseudo-steady assumption relies on the fact that diffusion occurs over a much faster time-scale than growth, hence the concentration has sufficient time to equilibrate to its steady-state value as the growth slowly proceeds, that is, the diffusion time-scale is much smaller than the growth time-scale $t_D \ll t_G$. From the diffusion equation we can see how time scales with distance, $t_D \sim r^2/D$. From equation (3.8) the growth time-scale $t_G = r^2/(V_M D \Delta C)$, and so $t_D/t_G = V_M \Delta C$. Since $V_M \Delta C$ is of the order of a^3 we see from Table 3.1 that $V_M \Delta C \sim a^3 \ll 1$ hence the standard pseudo-steady approximation will be accurate.

Now consider the approximation $\delta \gg r_p$, inherent to all analyses, where $\delta(t)$ is the thickness of the boundary layer and for a well-mixed solution $\delta(0) = 0$. Immediately it is clear that the approximation is invalid at small times. The question is then, what constitutes small time? As discussed above for diffusion it is well-known that in spherical problems time and distance scale as $t_D \sim r^2/D$, which then indicates that the boundary layer grows as $\delta \sim \sqrt{Dt}$. If we assume $\delta = 30r_p$ is sufficiently large to satisfy $\delta \gg r_p$, taking D from the first two columns of Table 3.1 and a typical value $r_p = 1\text{nm}$ then the time taken to achieve $\delta \gg r_p$ is $t = (30r_p)^2/D$ which varies approximately between 10-100s. That is, we can expect the approximation $\delta \gg r_p$ to be accurate beyond times of the order 100s. In fact this is clear from inspection of published experimental data. In [102, Fig 5] the first five data points (up to around 200s) follow a distinct curve to those for larger t , thus forcing the authors to find two sets of fitting parameters, for "curve 1" and "curve 2" (using the D value of Table 3.1 gives t of order 100s). The evolution of the diameter shown in [23,

Fig.3] also shows a distinct form for $t < 50$ s (their D value gives t of order 10s). Mendez *et al.* [71] discuss zones 1 and 2 for three different sets of results, the change occurs around 125s for two and 250s for the third. Without discussing specific zones, Brauser *et al.* [15, Fig.2a] presents a 'short time' solution, valid to around 100s. Bullen *et al.* [17] state that at early times the 'radius grows almost linearly'. Of course not all data shows such a clear demarcation, but there appears to be sufficient evidence to verify our assertion of a two-stage growth process, where the boundary layer increases in size until becoming significantly larger than the particle. So, from now on we will refer to Stages 1 and 2 to denote early and late time regimes respectively, and our analysis shows that when calculating system parameters data from Stage 1 should be neglected.

The Gibbs-Thomson equation (3.1) specifies the variation of the particle solubility with the radius. With the exception of [104] the variation is generally neglected based on the assumption that $\alpha \ll r_p$ [63, 103]. However, in Table 3.1 we have $\alpha \in [6.5, 7.39]$ nm, while in the experiments $r_p(0) \approx 1$ nm, this results in a typical factor of $e^7 \approx 10^3$ difference between taking the exponential form at early times or simply setting $C_s = C_\infty$, indicating the importance of the Gibbs-Thomson relation. To be clear, *neglecting the exponential variation will lead to huge errors in the model predictions*. So, how is it possible that previous researchers appear to have good agreement with data when making such a poor approximation? To understand this consider the data of Chuang *et al.* [23] from Table 3.1: $C_0 = 9.45$ mol/m³, $C_s = 7.9 \times 10^{-3} e^{6.68/r_p}$. If we take the initial radius $r_p = 1$ nm then $C_s(0) = 6.29 \approx 0.7C_0$, however due to the exponential dependence C_s rapidly decreases as r_p increases to its maximum of 2.89nm: when $r_p = 2$ nm $C_s = 0.22$, which is now negligible. As we will see in the comparison to experiment Stage 2 only starts when $r_p \approx 2.5$ nm. Consequently, although the Gibbs-Thomson relation plays a controlling role in particle growth during the Stage 1 this is when the standard model is not applicable. In modelling the growth of a single crystal, in Stage 2, the solubility plays a minor role and could be set to $C_s = C_\infty$ with negligible effect on the results. However, despite its minor contribution to growth of a single particle it does play an important role in the growth of a group of nanocrystals. With a single crystal growth stops when the maximum radius is reached, with a group of crystals one particle may have reached its limit while others are still growing, this acts to reduce the bulk concentration and then $C_b - C_\infty e^{\alpha/r_p}$ can become negative,

leading to the particle shrinking. In this way the growth or death of particles can depend crucially on the value of e^{α/r_p} .

3.6 An explicit solution for $r(t)$

Bullen *et al.* [17] state that while the evolution equation (3.14) is simple its solution is not, which makes the fitting of data a non-trivial task. Below we detail how the solution may be inverted to provide a simple form for $r_p(t)$, with a negligible error.

Since we only work in Stage 2 of the growth process we may neglect the exponential variation and define $C_{eq} = C_{\infty}e^{\alpha/r_m}$ as constant, then equation (3.15) which describes the relation $t(r_p)$ contains two distinct terms, involving arctan and log. This combination of terms prevents the inversion to $r_p(t)$. The ratio of these terms is

$$\lambda = \frac{2\sqrt{3}(bD - ak)}{(bD + ak)} \left[\frac{\arctan\left(\frac{a+2br_p}{\sqrt{3}a}\right) - \arctan\left(\frac{a+2br_{p0}}{\sqrt{3}a}\right)}{\ln\left(\frac{a^2+abr_p+b^2r_p^2}{a-br_p^2}\right) + \ln\left(\frac{a^2+abr_{p0}+b^2r_{p0}^2}{a-br_{p0}^2}\right)} \right]. \quad (3.16)$$

Taking the parameter values of Su *et al.* [102] this has a maximum value of approximately 2.5×10^{-3} which is achieved at $t = 0$, it then decreases monotonically to zero as $r_p \rightarrow a/b$, when the log term has a singularity. This means that the arctan term is always negligible compared to the log term and if it is dropped from the model the errors will be of the order 0.1%. Removing this term we find that both diffusion and kinetic driven processes are accurately approximated by a solution of the form

$$\begin{aligned} t - t_0 &= \frac{1}{6ab} \frac{ak + bD}{akbD} \left[\left\{ \ln \frac{a^2 + abr_p + b^2r_p^2}{(a - br_p)^2} - \ln \frac{a^2 + abr_{p0} + b^2r_{p0}^2}{(a - br_{p0})^2} \right\} \right] \\ &= G \ln \frac{f(r_p)}{f(r_{p0})}. \end{aligned} \quad (3.17)$$

Equation (3.17) is easily inverted to determine the radius as a function of time

$$f(r_p) = f(r_{p0}) \exp\left(\frac{t - t_0}{G}\right), \quad (3.18)$$

where $f(x) = (a^2 + abx + b^2x^2)/(a - bx)^2 = (r_m^2 + r_mx + x^2)/(r_m - x)^2$, where r_m is the radius when growth stops. This is a quadratic equation for r_p with solution

$$r_p = \frac{r_m}{2} \frac{\left[1 + 2f(r_{p0}) \exp\left(\frac{t-t_0}{G}\right) - \sqrt{-3 + 12f(r_{p0}) \exp\left(\frac{t-t_0}{G}\right)}\right]}{\left[-1 + f(r_{p0}) \exp\left(\frac{t-t_0}{G}\right)\right]}. \quad (3.19)$$

A feature made clear from the parameter $G = (ak + bD)/(6ab(akbD))$ is that ak and bD are interchangeable: it does not matter if we define them the opposite way round, the result is the same. Physically this means that *the model cannot distinguish between diffusion or reaction driven growth*. Consequently in the literature authors have been able to approximate experimental data, irrespective of the assumed driving mechanism. The equivalence may be confirmed by examination of the data of Table 3.1: only Su *et al.* [102] calculates both k and D to find $ak \approx 3.2 \times 10^{-10}$, $bD \approx 3 \times 10^{-10}$, which only differ by a few percent. In fact, as we discuss later, the small difference is most likely related to their solver or rounding errors.

The goal in developing a theoretical model is to determine how the controlling parameters influence the process and so understand how to optimise the growth. Part of this involves the determination of the diffusion and/or surface kinetic coefficients as well as the parameters a, b by fitting the model to the experimental data. Previous researchers have used the data to solve for all four, or just three in the diffusion or surface kinetic driven limit. In fact Su *et al.* [102] solve for eight parameters, four in each of their two stages. It is well-known that the more parameters there are to fit the less the chance of an accurate or even correct solution. For non-linear equations such as we have here there may be infinitely many solutions and the fitting algorithm may easily settle on an incorrect one. The non-uniqueness can be seen from the results of Mendez *et al.* [71], who calculate $a^3 = 2.21 \times 10^6$, $b^3 = 2.7 \times 10^{32}$, $D = 9.99 \times 10^{-28}$. The first two values are ten orders of magnitude greater than the values quoted by Su *et al.* [102] and Chuang *et al.* [23], the diffusion coefficient ten orders smaller yet they provide an excellent fit to their experimental data (shown in their Fig. 5 G3.5 solution). However the time-scale to reach the state where $\delta \gg r_p$ is of the order $10^{11}\text{s} \approx 32,000$ years as opposed to the observed 125s. Their solver has settled on a theoretically possible but physically unrealistic solution.

If we examine equation (3.19) we see that, provided r_m is measured, there is in fact just a single unknown, G , to solve for: this is a relatively simple task and with much less chance of settling on an incorrect solution. If r_m is not measured then there are two unknowns, which again is significantly simpler and more reliable than fitting to three or four unknowns. For the present study we take r_m to be the maximum value obtained in the experiments, for

certain cases this must be viewed as an approximation: with Chuang *et al.* [23] it is clear that the growth process has stopped, whereas with Pan *et al.* [85] it appears the crystal could slightly increase in size if the experiment were carried on for longer. We then apply a simple least-squares fit to the data in the Stage 2. In certain cases this stage is easily identified, for others it is not clear. However, if t_0 is chosen to be too large it should not make a difference to results, provided we are in Stage 2 the value obtained for G should remain approximately constant, regardless of the number of experimental points. As an example we note that in the results shown below the value obtained for G when using the data of Chuang *et al.* [23] changed by 1% when starting at the 5th or 6th data points.

Given that we cannot use growth data alone to determine important parameters such as the diffusion coefficient or surface reaction rate it is clear that we must employ other experimental data to complete the system. In this case we propose using the measured concentration data. If we take the example of Chuang *et al.* [23] we have so far determined $G = 28.28$, using their measured $r_m = 2.89\text{nm}$. Their initial concentration $C_0 = 9.45\text{mol/m}^3$ and the process stops when $C_{eq} = C_\infty e^{\alpha/r_m} = 0.08\text{mol/m}^3$, the molar volume is $V_M = 3.3 \times 10^{-5}\text{m}^3/\text{mol}$. This allows us to calculate $a^3 = V_M(C_0 - C_{eq}) = 3.09 \times 10^{-4}$ and hence $b^3 = (a/r_m)^3 = 1.28 \times 10^{22}$. Since $ak = bD$ then $r_m = a/b = D/k$ and $G = r_m/(3a^3k) = r_m^2/(3a^3D)$ indicates $k = 1.1 \times 10^{-7}$, $D = 3.3 \times 10^{-16}$ (note, they obtain a value $D = 1.5 \times 10^{-16}$).

In Figures 3.1 and 3.2 we compare the results of the present model with experimental data from Refs. [17, 23, 85, 102]. The dots represent the experimental data, the solid line the curve described by equation 3.19 with G provided by the least squares calculation, the dashed line is obtained by using the parameter values quoted in the respective papers in (3.19). Fig 3.1(a) shows the crystal growth reported by Chuang *et al.* [23]. The first four points approximately follow a straight line, so we assume they occupy Stage 1 and so take r_{p0}, t_0 as the position of the fifth data point. The maximum radius measured is $r_m = 2.89\text{nm}$, after substituting this into equation (3.19) and carrying out a least-squares fit to the final six points we obtain $G = 28.28$. Note, in some experiments there is a clear demarcation between zones but this is not always the case. However, provided we only use data from Stage 2 the choice of starting point should be irrelevant. For example, if we only use the final five points in the least squares calculation then we obtain $G = 28.56$,

which is a 1% increase on the previous value. Taking the values from Table 3.1 we obtain $G = r_m^2/(3a^3D) \approx 60$, which leads to a rather poor fit. In fact their paper shows a better fit to data, but unfortunately they do not state the values of a, b obtained, only the value of D and the ratio $a/b = 2.885$ (which is slightly below the experimental value), so it is not possible to reproduce their fitting curve. Our result suggests $D = r_m^2/(3a^3G) \approx 3.18 \times 10^{-16}$ which is more than double their quoted value. The fact they obtain a good fit with a different value for D is indicative of the non-uniqueness of solutions and the difficulties of fitting to a number of parameters. For the data of Bullen *et al.* [17] we take r_{p0}, t_0 from the 4th point, although from the figure it appears that the 3rd would be an equally good starting point. This leads to $G = 18.82$. The data of Table 3.1 indicates a value $G = r_m/(3a^3k) \approx 19.66$ which also leads to good agreement between the data and equation (3.19).

Figures 3.2(a) and 3.2(b) show the comparisons between the data of Refs. [85, 102]. In these two cases the growth is much slower than the previous examples and G increases accordingly. For Pan *et al.* [85] we take Stage 2 as starting at the 5th point ($n = 5$, the first four points follow a clear straight line) to obtain $G = 1166$, the data quoted in Table 3.1 gives $G = 7602$ which leads to very poor agreement with the data. Note Pan *et al.* [85] calculate a, b from their concentration data and only use the growth data to determine k . Using their value for $a^3 = 8.25 \times 10^{-5}$ and taking the final radius $r_p = 1.75\text{nm}$ as being approximately the maximum radius and $G = 1166$, we obtain $k = 6.06 \times 10^{-9}$ as opposed to their quoted value of 9.74×10^{-10} . This new value is consistent with that quoted by Su *et al.* [102]. For the final figure we start at the 9th point, since the first eight points appear to follow a different trend. This leads to $G = 789.3$ which is very close to the value of Table 3.1, $G = 824$. Both G values provide an excellent approximation, although our prediction obviously leads to a lower least squares error.

We have presented results for the growth of Cd crystals although it is clearly applicable to other materials. Varghese *et al.* [107] study the growth of platinum. In their Figure 7 they show the evolution of the average diameter over time. They claim the data cannot be fitted using the diffusion model alone, so they add an extra term (and so an extra fitting parameter) to account for surface reaction and consequently find a good fit to the data. However, if we set $r_m = 2.4\text{nm}$ (although their growth has clearly not finished) we find an equally good fit to their final five data points, $t > 18$ minutes, with the one-parameter

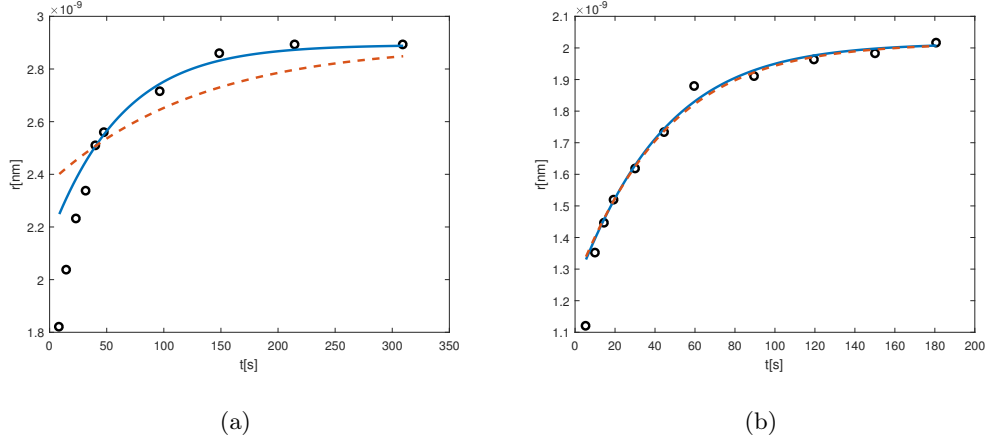


Figure 3.1: Chuang *et al.* [23] $G = 28.28$, $r_m = 2.892$, $n = 5$ ($n = 6$, $G = 28.56 = 1\%$ change), Bullen *et al.* [17] $G = 18.82$, $n = 4$, $r_m = 2.015$.

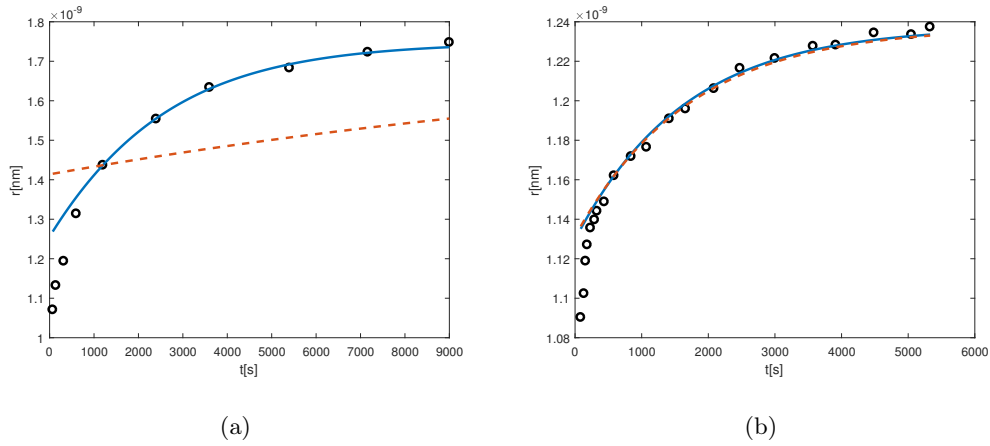


Figure 3.2: Pan *et al.* [85] $G = 1166$, $n = 5$, $r_m = 1.75$, Su *et al.* [102] $G = 789.3$, $n = 9$, $r_m = 1.24$.

model and $G = 22.12$.

3.7 Conclusion

The analysis of this paper leads to five important conclusions.

- The standard pseudo-steady model is not valid for early times. The definition of early time depends on the experimental conditions but, as has been noted by many researchers, there is a clear shift in the trend of the growth data: results prior to this shift constitute the early time. Only in the second stage may the pseudo-steady model be applied. In fact this is hardly surprising. The assumption of smooth spherically symmetric growth is far from realistic at early times, when the addition of new atoms or 'blobs' together with the presence of a co-ordinating solvent will ensure that the initial growth is not well approximated by a symmetric growth model.

If all growth data obtained from an experiment, including that at early time, is used to calculate the model parameters then these values will be incorrect and will not represent the physical quantities.

- Within the assumptions of the standard pseudo-steady model *it is not possible to distinguish between diffusion or surface reaction driven growth.* Consequently researchers have been able to fit experimental data equally well assuming either one as the dominant mechanism or retaining both.
- Within experimental error it is a simple matter to invert the well-known implicit growth relation $t = t(r_p)$ to the more practically useful form $r_p = r_p(t)$. This has not previously been presented in the literature. In fact, assuming $ak = bD$ then the inversion is exact.
- *At most the growth model can only determine two independent growth parameters. If the maximum radius is known then the growth data determines just a single parameter.* Previous work where a number of parameters are calculated have redundant elements: in Ref. [102] four parameters are calculated from the growth data, but $ak \approx bD$ and $r_m \approx a/b \approx D/k$ (due to the use of fitting routines some accuracy is lost and therefore

the relations are not exactly equal). Fitting to a single parameter is generally simpler and more accurate. For example, with more fitting parameters it is more likely that incorrect values are found: we presented an example where the parameters differed from those of other studies by an order of ten in magnitude.

- *Depending on the material or initial size of the crystal neglecting the variation of the particle solubility can be highly inaccurate.* This error has not been picked up before due to the fact that, certainly in the experiments examined in the present paper, it influences the results during the initial growth stage when the pseudo-steady model is incorrect anyway.

4 | Modelling nanocrystal growth via the precipitation method

C. Fanelli, V. Cregan, F. Font, T. G. Myers.

Modelling nanocrystal growth via the precipitation method.

To appear in International Journal of Heat and Mass Transfer (2020).

Impact factor: 4.346

Abstract

A mathematical model for the growth of a single nanocrystal is generalised to deal with an arbitrarily large number of crystals. The basic model is a form of Stefan problem, describing diffusion of monomer over a moving domain. Various levels of approximation (an analytical solution, an ordinary differential equation model and an N particle model) are compared and shown to agree well. The N particle model and analytical solution are then shown to have excellent agreement with experimental data for the growth of CdSe nanocrystals. The theoretical solution clearly shows the effect of problem parameters on the growth process and, significantly, that there is a single controlling group. By increasing the value of N it is shown that in the absence of Ostwald ripening the single particle model may be considered as representing the average radius of a system with a large number of particles. Consequently a system with $N = 2$ may represent either a two particle system or a bimodal initial distribution. The solution of the $N = 2$ model provides an understanding of Ostwald ripening. In general if Ostwald ripening is expected some form of the N particle

model should be employed. Finally it is shown how the analytical solution may be employed to represent a multi-stage growth process which can then guide and optimise crystal growth.

4.1 Introduction

Nanoparticles (NPs) are small units of matter with dimensions in the range 1-100 nm. They exhibit many advantageous, size-dependent properties such as magnetic, electrical, chemical and optical, which are not observed at the microscale or larger [11, 46, 74, 105]. Consequently the ability to produce monodisperse particles that lie within a controlled size distribution is critical.

There exist a number of NP synthesis methods, including gas phase and solution based synthesis techniques. Although the first method can produce large quantities of nanoparticles, it produces undesired agglomeration and nonuniformity in particle size and shape. Precipitation of NPs from solution avoids these problems and is one of the most widely used synthesis methods [69]. The typical strategy is to cause a short nucleation burst in order to create a large number of nuclei in a short space of time, and the seeds generated are used for the latter particle growth stage. The resulting system consists of varying sized particles. Small NPs are more unstable than larger ones and tend to grow or dissolve faster. Thus at relatively high concentrations size focussing occurs (leading to monodispersity). When the concentration is depleted by the growth some smaller NPs shrink and eventually disappear while larger particles continue to grow, thus leading to a broadening of the size distribution (which involves the process of Ostwald ripening). Ostwald ripening is the process whereby smaller crystals dissolve and the material from these crystals is redeposited onto the larger ones. Hence, below a certain size the crystals start to decrease in size until they disappear, while larger crystals increase in size. Perhaps the most well-known example of Ostwald ripening is the coarsening of crystals in ice cream, giving a different texture to old ice cream. Depending on the system Ostwald ripening can be rapid or very slow, as in the famous experiment of Faraday in the 1850's using colloidal gold which is still optically active.

The particle size distribution (PSD) can be refocused by changing the reaction kinetics. For example, Peng *et al.* [90] observed size focusing during Cadmium Selenide growth

following the injection of additional solute. Bastús *et al.* [10, 9] were also able to induce size focusing of gold and silver nanoparticles by the addition of extra solute and adjusting the temperature and pH. This type of technique for size focussing is still rather *ad hoc* in that the precise relationships between particle growth, system conditions and the final PSD are not fully understood [97]. Hence, in practice, the optimal reaction conditions are usually ascertained empirically or intuitively.

In the 1960's Lifshitz and Slyozov [62] and, independently, Wagner [115] were amongst the first to provide theoretical descriptions of Ostwald ripening. Their classical theory, hereafter referred to as LSW theory, consisted of a system of three coupled equations: a growth equation for a single particle, a continuity equation for the PSD and a mass conservation expression for the concentration. They solved the model to obtain pseudo-steady-state asymptotic solutions for the average particle radius and PSD. Lifshitz and Slyozov [62] focused on diffusion-limited growth, where growth is limited by the diffusion of reactants to the particle surface, while Wagner [115] considered growth limited by the reactions at the particle surface. In fact recent work described by Myers and Fanelli [79] has shown that, within the restrictions of the steady-state assumption, the models cannot distinguish between diffusion or reaction driven growth, so both approaches are equally valid. For this reasons authors using either mechanism, or both, have been equally successful in approximating experimental data.

Experimental studies on NP growth [23, 85, 102] show that LSW theory may provide good predictions for the particle size but the observed PSDs are typically broader and more symmetric. Possible explanations for this disparity is that LSW theory does not account for the finite volume of the coarsening phase ϕ , and that it assumes a particle's growth rate is independent of its surroundings. In addition, LSW theory does not indicate how long it takes to reach the final state. A further issue is that it purports to describe the dynamics in the initial stages of the growth process. In [79] it is proven that the pseudo-steady solution does not hold for small times.

Many studies have modified and built on the pioneering analysis of LSW theory. Ardell [4] and Sarian and Weart [96] extended LSW theory to systems where the mean distance between particles is finite. Several authors [14, 112, 113] have addressed the shortcomings of LSW theory by statistically averaging the diffusional interaction of a particle of a given

size with its surroundings to demonstrate that the resulting PSD becomes broader and more symmetric with increasing ϕ . The inclusion of stochastic effects, due to temperature and changes in concentration, in the modified population balance model of Ludwig *et al.* [67] led to broader PSDs in line with experimental data. The population balance approach of Igglund and Mazzotti [51] was used to examine the evolution of non-spherical particles at the beginning of growth.

Most of the above studies were in relation to micron or larger-sized particles. As measurement techniques have advanced many researchers have applied LSW theory and the related modifications to the study of nanoparticle growth. Talapin *et al.* [104] used a Monte Carlo approach to simulate the evolution of a nanoparticle PSD subject to diffusion-limited growth, reaction-limited growth and mixed diffusion-reaction growth. In contrast to other treatments, their simulations gave PSDs narrower than those predicted by LSW theory. This was explained by the fact that they considered much smaller particles. Their main conclusion was that Ostwald ripening occurs much more rapidly for nanoparticles while PSDs are narrower than in their microscale counterparts. Similarly, Mantzaris [69] used a population balance formulation and a moving boundary algorithm to study the diffusion and reaction-limited growth regimes.

Another issue which is particularly relevant in the context of nanoparticles is the applicability of the Ostwald-Freundlich condition which relates the radius of the particle, r_p^* , to its solubility, s^* . This condition can be written as

$$s^* = s_\infty^* \exp\left\{\left(\frac{2\sigma V_M}{r_p^* R_G T}\right)\right\} \equiv s_\infty^* \exp\left\{\left(\frac{\alpha}{r_p^*}\right)\right\}, \quad (4.1)$$

where s_∞^* is the solubility of the bulk material, σ the interfacial energy, R_G the universal gas constant, T the absolute temperature. The capillary length $\alpha = 2\sigma V_M/(R_G T)$ defines the length scale below which curvature-induced solubility is significant [104]. This equation shows that the particle solubility increases as the size decreases (which promotes Ostwald ripening). One approximation to the Ostwald-Freundlich condition is to assume that the exponential term in (4.1) can be linearised to give the two term expression $s^* \approx s_\infty^*(1 + \alpha/r_p^*)$ [62, 63, 103, 115]. Obviously this expansion, which is based on α/r_p^* , is invalid for nanoparticles where the capillary length is of the same order of magnitude as the particle radius [79]. Mantzaris [69] used an expansion for the exponential term in the

Ostwald-Freundlich condition with n terms and showed that increasing n led to higher average growth rates and a narrowing of the PSD. However, when comparing his simulation to experimental data for CdSe nanoparticles from [89], he applied a linear version for the solubility. Talapin *et al.* [104], noting that for nanoparticles of the order 1-5 nm the linearised Ostwald-Freundlich condition may be incorrect, applied the full condition.

In the following we begin by analysing the growth of a single particle. This is the basic building block for more complex models. The treatment leads to equations similar to those of standard LSW theory, however we arrive at them following a non-dimensionalisation which highlights dominant terms and those which may be formally neglected. In this way we can ascertain which standard assumptions are appropriate and, more importantly, which are not. Under conditions which appear easily satisfied for nanocrystal growth the governing ordinary differential equation has an explicit solution, in the form $r_p = r_p(t)$ and also shows that the growth is controlled by a single parameter which may be calculated by comparison with experiment. This section closely follows the work described in [79]. The single particle model is obviously incapable of reproducing Ostwald ripening, where larger particles grow at the expense of smaller ones. Consequently we then generalise the model to deal with a large number of particles. In the results section we compare the analytical solution with that of a full numerical solution and experimental data for the growth of a single particle and show excellent agreement between all three. By setting the number of particles to two in the general model we are able to clearly demonstrate Ostwald ripening. Simulations with $N = 10$ and 1000 particles demonstrate that increasing N leads to increasingly good agreement between the average radius and that predicted by the single particle model. The single particle model may thus be considered as a viable method for predicting the evolution of the average radius of a group of particles.

4.2 Growth of a single particle

As shown in Figure 4.1, we initially focus on a single, spherical nanoparticle, with radius r_p^* in a system of particles. The $*$ notation represents dimensional quantities. The assumption is that particles are separated at large but finite distances compared to their radius. Their

morphologies remain nearly spherical and particle aggregation is neglected. Thus, the mass flow from each particle can be represented as a monopole source located at the center of the particle [111] and the problem becomes radially symmetric. We assume the standard La Mer model [58], such that there has been a short nucleation burst and the system is now in the period of growth.

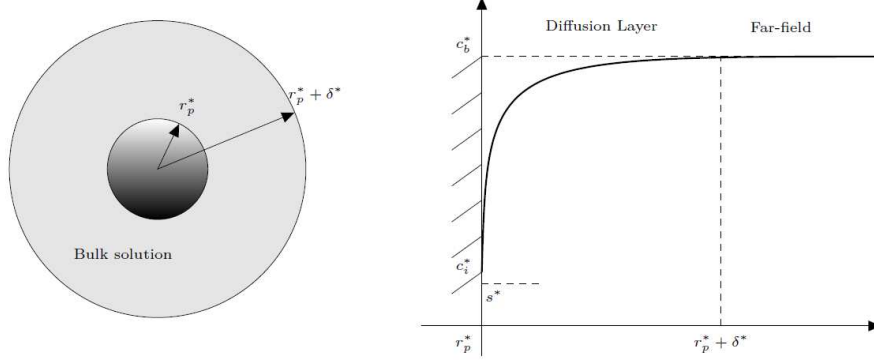


Figure 4.1: Schematic of a single nanoparticle with radius r_p^* and the surrounding monomer concentration profile where s^* , c_i^* and c_b^* are the particle solubility, the concentration at the surface of the particle and the far-field concentration, respectively.

The monomer concentration, c^* , is described by the classical diffusion equation in spherical coordinates

$$\frac{\partial c^*}{\partial t^*} = \frac{D}{r^{*2}} \frac{\partial}{\partial r^*} \left(r^{*2} \frac{\partial c^*}{\partial r^*} \right). \quad (4.2)$$

This holds in the diffusion layer $[r_p^*, r_p^* + \delta^*]$ where r^* is distance from the centre of the particle, t^* is time and D is the constant diffusion coefficient. To conform with standard literature (see for example [69, 103, 108]), we have included a diffusion layer of length δ^* around the particle, where the concentration adjusts from the value at the particle surface to the value in the far-field. Equation (4.2) is then subject to

$$\begin{aligned} c^*(r_p^*, t^*) &= c_i^*(t^*), & c^*(r_p^* + \delta^*, t^*) &= c_b^*(t^*), \\ c^*(r^*, 0) &= c_{b,0}^* & \text{for } r_p^* < r^* < r_p^* + \delta^*, \end{aligned} \quad (4.3)$$

where c_i^* is the concentration adjacent to the particle surface, c_b^* is the concentration in the far-field and $c_{b,0}^* = c_b^*(0)$ is a constant describing the initial concentration when the solution is well-mixed (and the crystal is at the initial size $r_p^*(0)$). The value at the particle surface

c_i^* is very difficult to measure [103], hence it is standard to work in terms of the particle solubility.

The particle solubility s^* (with the same dimensions as concentration) is given by the Ostwald–Freundlich condition (4.1). If $s^* < c_b^*$ then monomer molecules diffuse from the bulk towards the particle to react with the surface and the particle grows, whereas if $s^* > c_b^*$ the particle shrinks.

In order to determine an expression for the concentration at the particle surface, we consider two equivalent relations for the mass flux at the particle surface, J . Firstly, Fick's first law states that the flux of monomer passing through a spherical surface of radius r^* is

$$J = 4\pi r^{*2} D \frac{\partial c^*}{\partial r^*}. \quad (4.4)$$

At the surface of the sphere the flux must also follow a standard first order reaction equation

$$J = 4\pi r^{*2} k (c_i^* - s^*), \quad (4.5)$$

where k is the reaction rate, which is assumed to be constant for both growth and dissolution contributions. Equating (4.4) with (4.5) gives

$$c_i^* = s^* + \frac{D}{k} \frac{\partial c^*}{\partial r^*} \Big|_{r^*=r_p^*}, \quad (4.6)$$

which defines the concentration c_i^* for the surface condition of (4.3).

To complete the boundary conditions in the system, we require an expression for the time-dependent bulk concentration, $c_b^*(t^*)$. Mass conservation of the monomer in the particle and in the surrounding solution is

$$\frac{1}{N_0} M_p c_0^* = M_p c_b^*(t) \left[\frac{1}{N_0} - \frac{4\pi}{3} r_p^{*3} \right] + \frac{4\pi}{3} \rho_p r_p^{*3}, \quad (4.7)$$

where c_0^* is the initial monomer concentration (measured before seed crystals appear), ρ_p is density, M_p is molar mass and N_0 the population density. The left hand side represents the mass of monomer in the volume to be occupied by the single crystal. The right hand side contains two components, the first is the mass of monomer in the solution surrounding the crystal (this volume consists of the original region minus the volume occupied by the crystal). The second component is the mass of the crystal. If the system is dilute then

$4\pi N_0 r_p^{*3}/3 \ll 1$. Writing the molar volume $V_M = M_p/\rho_p$, equation (4.7) then leads to

$$c_b^*(t) \approx c_0^* - \frac{4\pi N_0}{3V_M} r_p^{*3}, \quad (4.8)$$

which will be used to represent the far-field concentration in (4.3).

The diffusion equation must be solved on a domain $r^* > r_p^*$, where the particle radius is an unknown function of time. The flux of monomer to the particle is responsible for the particle growth

$$V_M J = \frac{d}{dt^*} \left(\frac{4}{3} \pi r_p^{*3} \right) = 4\pi r_p^{*2} \frac{dr_p^*}{dt^*}. \quad (4.9)$$

Eliminating J between (4.9) and (4.4) yields

$$\frac{dr_p^*}{dt^*} = V_M D \left. \frac{\partial c^*}{\partial r^*} \right|_{r^*=r_p^*}, \quad (4.10)$$

which describes the particle radius evolution. Equation (4.10) is subject to the initial condition $r_p^*(0) = r_{p,0}^*$, where $r_{p,0}^*$ is the initial particle radius. The combination of the diffusion equation, (4.2), describing the monomer concentration which is solved over a moving domain, determined by equation (4.10), indicates that we are dealing with a Stefan problem. The classical Stefan problem models phase change due to temperature variation and so is described by the heat equation with the boundary defined by an energy balance. The phase change temperature is a specified constant. Since we do not consider the monomer concentration within the crystal while the interface concentration $c_i^*(t^*)$ is a function of time our model is mathematically equivalent to a one-phase Stefan problem with a supercooled liquid phase (also termed undercooled). A Cartesian version is studied in [35]. A similar two-phase problem is studied in [36] which deals with spherically symmetric nanoparticle melting, with a size-dependent melting temperature. In this case it may be seen that as the particle shrinks the boundary condition acts to speed up the melting process, in the limit of the radius tending to zero the shrinkage rate tends to infinity. In the present case the crystal is growing, hence the boundary condition acts to slow down the growth (as compared to a fixed concentration condition). The standard Stefan problem is highly nonlinear, with a single exception, exact solutions have little physical application. In the present case of a non-standard problem no exact solution is available.

The governing system is now fully defined and consists of equation (4.2), subject to the initial and boundary conditions (4.3), where c_i^* is defined by (4.6) and c_b^* by (4.8), and the unknown particle radius satisfies (4.10). As widely known, there are a very few practically useful exact solutions to moving boundary problems due to the non-linearity caused by the Stefan condition. A general approach involves the use of approximate methods in order to analyse Stefan problems when no analytical solution exists, as in this case. Therefore, we proceed to simplify the problem and use numerical approximations in order to understand the behaviour of the solution.

4.2.1 Nondimensionalisation

The model is nondimensionalised via

$$r = \frac{r^*}{r_{p,0}^*}, \quad r_p = \frac{r_p^*}{r_{p,0}^*}, \quad t = \frac{t^*}{\tau^*}, \quad c = \frac{c^* - s_0^*}{\Delta c}, \quad s = \frac{s^* - s_0^*}{\Delta c}, \quad (4.11)$$

where $\Delta c = c_b^*(0) - s_0^*$ represents the driving force for particle growth, $s_0^* = s^*(0) = s_\infty^* \exp\{(\alpha/r_{p,0}^*)\}$ is the initial particle solubility. The concentration and growth equations yield two possible time scales $\tau_D^* = r_{p,0}^{*2}/D$ and $\tau_R^* = r_{p,0}^{*2}/(V_M D \Delta c)$, respectively. To focus on particle growth we choose the time scale $\tau^* = \tau_R^*$ and the system is now transformed to

$$\varepsilon \frac{\partial c}{\partial t} = \frac{1}{r^2} \frac{\partial}{\partial r} \left(r^2 \frac{\partial c}{\partial r} \right), \quad \frac{dr_p}{dt} = \frac{\partial c}{\partial r} \Big|_{r=r_p}, \quad (4.12)$$

$$c(r_p, t) = s + \text{Da} \frac{\partial c}{\partial r} \Big|_{r=r_p}, \quad c(r_p + \delta, t) = c_b(t) = c_0 - \beta r_p^3, \quad (4.13)$$

$$c(r, 0) = 1, \quad r_p(0) = 1, \quad (4.14)$$

where

$$\varepsilon = V_M \Delta c, \quad \delta = \frac{\delta^*}{r_{p,0}^*}, \quad \text{Da} = \frac{D}{k r_{p,0}^*}, \quad \omega = \frac{\alpha}{r_{p,0}^*}, \quad \beta = \frac{4\pi N_0 r_{p,0}^{*3}}{3V_M \Delta c}, \quad c_0 = \frac{c_0^* - s_0^*}{\Delta c}. \quad (4.15)$$

The above system contains a number of nondimensional groups. The first, ε , is generally very small for nanoparticle growth. For example, Peng *et al.* [89] studied Cadmium Selenide nanoparticles, with a capillary length of 6nm and initial radii in the range 1 – 100 nm, so that $\varepsilon = \mathcal{O}(10^{-3})$. In general it should be expected that $\varepsilon \ll 1$. If we look at the time

scales, we see that $\tau_D^*/\tau_R^* = V_M \Delta c = \varepsilon \ll 1$. Physically, this indicates that growth is orders of magnitude slower than the diffusion time scale, that is, the concentration adjusts much faster than growth occurs and so the system can be considered as pseudo-steady. In terms of the mathematical model, this means that the time derivative can be omitted from the concentration equation, but since time also enters into the problem through the definitions of r_p and c_b this is a pseudo-steady-state rather than a true steady-state.

The parameter Da is an inverse Damköhler number measuring the relative magnitude of diffusion to surface reactions [69]. In the past similar models have been simplified by considering diffusion-limited growth ($Da \ll 1$) or surface reaction limited growth ($Da \gg 1$). In practice both mechanisms play a role. So, we will place no restrictions on Da .

A common simplification is to assume $\omega \ll 1$ which reduces the Ostwald-Freundlich condition, (4.1), to a constant $s^* = s_\infty^*$ or a linear approximation is used, see [63, 103]. This significantly simplifies the analysis. However, for particles that have just nucleated or very small nanoparticles ω is not small and the simplification is not appropriate. Despite the large errors in the prediction of s^* caused by the small ω assumption authors obtain good matches to data. In [79] it is shown that this is because the pseudo-steady model is not valid for early times when the particle is small. By the time the model is valid so is the linearisation. Basically, the variation of s^* plays a minor role in the study of the growth of a single nanoparticle. However, this is not the case with multiple particles where Ostwald ripening is driven by the delicate balance between the bulk concentration and the particle solubility.

The reason why the pseudo-steady model is invalid at small times is due to the thickness of the boundary layer $\delta(t)$. The model involves the assumption $\delta(t) \gg r_p$ yet initially, when the fluid is well-mixed $\delta(0) = 0$. Only when the boundary layer is sufficiently thick is it reasonable to apply the pseudo-steady model. In [79] it is shown through comparison with experiments that the initial stage can last for the order of 100s. The shift to the pseudo-steady model can often be identified simply by looking at the trend in the data. In the following we will present the model with the full Ostwald-Freundlich condition and then an approximation where it is neglected. We will also neglect early data points when matching to experimental data.

4.2.2 Pseudo-steady state solution

Since $\varepsilon = \mathcal{O}(10^{-3})$ and all variables have been scaled to be $\mathcal{O}(1)$ neglecting terms of order ε should result in errors of the order 0.1%. Consequently, we neglect the time derivative in the diffusion equation and obtain the pseudo-steady state form

$$\frac{1}{r^2} \frac{\partial}{\partial r} \left(r^2 \frac{\partial c}{\partial r} \right) = 0. \quad (4.16)$$

After integrating and applying the boundary conditions we obtain

$$c = -\frac{A}{r} + B, \quad (4.17)$$

where

$$A = \frac{r_p^2(r_p + \cdot)(c_b - s)}{r_p + \text{Da}(r_p + \cdot)}, \quad B = s + A \left(\frac{1}{r_p} + \frac{\text{Da}}{r_p^2} \right). \quad (4.18)$$

There is no way to calculate $\delta(t)$ in the pseudo-steady approach. A time-dependent treatment, such as that described in [78] is required. Hence the standard method is to assume $r_p \ll \delta$, which reduces the concentration to

$$c = c_b - \frac{r_p^2(c_b - s)}{(r_p + \text{Da})r}. \quad (4.19)$$

Note, provided $\delta(t) \gg r_p$ the value of δ is irrelevant: we may neglect the time variation.

Substituting (4.17) into the growth condition (4.12) leads to

$$\frac{dr_p}{dt} = \frac{c_b(r_p) - s(r_p)}{\text{Da} + r_p} = \frac{c_0 - \beta r_p^3 - s(r_p)}{\text{Da} + r_p}. \quad (4.20)$$

Hence, the problem has been reduced to the solution of a single first-order ordinary differential equation for r_p . It is a highly nonlinear equation which must be solved numerically. The assumption that $r_p \ll \delta$ means it only holds for relatively large times. Approximate solutions, in various limits, may be found in the literature. For example if we take c_b constant and ω sufficiently small for the linear approximation to the exponential to hold then equation (4.20) may be integrated in the limits of large and small Da. In [79] it is shown that for sufficiently large times, for a single particle, the variation of e^{ω/r_p} is small in which case equation (4.20) may be integrated analytically to find an implicit solution of the form $t = t(r)$. By identifying negligible terms they are able to invert this to find an explicit solution, $r = r(t)$ which depends on a single parameter,

$$r_p = \frac{r_m}{2} \frac{\left[1 + 2f(r_{ps}) \exp\left(\frac{t-t_s}{G}\right) - \sqrt{-3 + 12f(r_{ps}) \exp\left(\frac{t-t_s}{G}\right)} \right]}{\left[-1 + f(r_{ps}) \exp\left(\frac{t-t_s}{G}\right) \right]}, \quad (4.21)$$

where r_m is the (non-dimensional) experimental maximum radius, t_s is the time at which the second growth stage is judged to have begun, r_{ps} the radius at this time and $f(r_{ps}) = (r_m^2 + r_m r_{ps} + r_{ps}^2)/(r_m - r_{ps})^2$. Provided t_s is chosen within the later growth stage the choice should not greatly affect the results. However, in general we would prefer to choose t_s as close to the switch between the initial and later stages as possible to maximise the number of data points for the fitting. This is discussed in further detail in [79]. The unknown parameter G is defined as

$$G = \frac{1}{6ab} \frac{ak + bD}{akbD}, \quad a^3 = V_m(c_0^* - c_{eq}^*), \quad b^3 = \frac{4}{3}\pi N_0. \quad (4.22)$$

Its value is obtained by comparison with experimental data. The parameter c_{eq}^* is an approximation. It is a constant which replaces the variable $s_\infty \exp(\alpha/r_p)$, in [79] the concentration at the end of the experiment is used to provide its value. Once G is determined, then the diffusion coefficient (D), the reaction rate (k), the solubility of the bulk material (s_∞) and population density (N_0) may be systematically retrieved. In [79] it is stated that $ak \approx bD$, hence $G \approx 1/(3a^2bk) = 1/(3ab^2D)$. Further, since $c_0^* \gg c_{eq}^*$ a reasonable approximation is $a^3 = V_m c_0^*$. Growth stops when the maximum radius $r_m^* = a/b$ is achieved.

4.3 Evolution of a system of N particles

We now extend the above single particle model to a system of N particles where N is arbitrarily large and may decrease with time due to Ostwald ripening. The particle radii, initial radii and solubilities are denoted r_i^* , $r_{i,0}^*$ and s_i^* , respectively, where $i = 1, \dots, N$ represents the i^{th} particle. We nondimensionalise via (4.11) with the only difference being that the length scale $r_{p,0}^*$ is replaced by the mean value $\bar{r}_{i,0}^* = \Sigma_{i=1..N}(r_{i,0}^*/N)$. It has to be noted that this affects the concentration scale through the initial solubility which now becomes $\bar{s}_{i,0}^* = s_\infty^* e^{\alpha/\bar{r}_{i,0}^*}$, then $\bar{\Delta c} = c_{b,0}^* - \bar{s}_{i,0}^*$. Hence in what follows, all dimensionless parameters defined in equation (4.15) carry an overbar to reflect the change in length scale.

Under the pseudo-steady approximation and assuming that there are no interparticle diffusional interactions, the growth of each particle is now described by an equation of the form (4.20). This requires an expression for the bulk concentration which must account for

the fact that all particles remove monomer and that the volume is now N times that of the single particle

$$\frac{N}{N_0} M_p c_0^* = M_p c_b^*(t^*) \left[\frac{N}{N_0} - \frac{4\pi}{3} \sum_{i=1}^N r_i^{*3} \right] + \frac{4\pi\rho_p}{3} \sum_{i=1}^N r_i^{*3}. \quad (4.23)$$

Again assuming that the solution is sufficiently dilute that $(4\pi N_0/3N) \sum_{i=1}^N r_i^{*3} \ll 1$, we obtain

$$c_b^*(t^*) \approx c_0^* - \frac{4\pi N_0}{3NV_M} \sum_{i=1}^N r_i^{*3}. \quad (4.24)$$

In the limit where all particles are identical $\sum_{i=1..N} r_i^{*3} = N r_i^{*3}$ and the single particle model of equation (4.8) is retrieved. In dimensionless form the problem is then governed by the system of differential equations

$$\frac{dr_i}{dt} = \frac{\bar{c}_b(r_i) - \bar{s}(r_i)}{\bar{D}a + r_i} = \frac{\bar{c}_0 - (\bar{\beta}/N) \sum_{i=1}^N r_i^3 - \bar{s}(r_i)}{\bar{D}a + r_i} \quad (4.25)$$

for each $i = 1, \dots, N$ and

$$\begin{aligned} \bar{D}a &= \frac{D}{k\bar{r}_{i,0}^*}, & \bar{\beta} &= \frac{4\pi N_0 \bar{r}_{i,0}^{*3}}{3V_M \bar{\Delta}c}, & \bar{c}_0 &= \frac{c_0^* - \bar{s}_{i,0}^*}{\bar{\Delta}c} \\ \bar{s}(r_i) &= \frac{s_\infty^*}{\bar{\Delta}c} \left(e^{\bar{\omega}/r_i} - e^{\bar{\omega}/r_{i,0}} \right), & \bar{\omega} &= \frac{\alpha}{\bar{r}_{i,0}}. \end{aligned} \quad (4.26)$$

Equation (4.25) represents a system of N non-linear ODEs which must be solved numerically.

4.4 Comparison of model with experiment

Using the full numerical solution, defined by (4.12)–(4.14), on the N particles model would be prohibitively expensive. For this reason the first goal of this section is to demonstrate that the pseudo-steady state model of equation (4.20) is a good approximation to (4.12)–(4.14), so justifying its use in our N particles model. We validate the models using experimental data on CdSe nanocrystals synthesis taken from [89]. Certain parameter values concerning the experiment and CdSe are provided in that paper, others, such as D, k, s_∞^*, N_0 must be inferred. Here they will be determined through fitting to equation (4.21). Since this only contains one free parameter the fitting is a very simple process.

4.4.1 Parameter estimation via the analytical solution

In Figure 4.2 we show the first eleven data points from [89]. As discussed earlier not all data points correspond to the pseudo-steady regime, here it is clear that the first three points follow a linear trend so these will be neglected. In the experiment extra monomer was added after three hours, so we have ignored all data beyond the eleventh point. Using the remaining eight data points in the nonlinear least-squares Matlab solver `lsqcurvefit` to fit to equation (4.21) we obtain $G \approx 958$. To determine the necessary parameters for the other models we first note that the maximum radius attained during this part of the experiment is $r_m^* \approx 3.8\text{nm} = a/b = D/k$. The experimental concentration at the end of the growth process is known, this defines $c_{eq}^* = s_\infty^* e^{\alpha/r_m^*} \approx 0.08 \text{ mol/m}^3$. This together with the definition $G = r_m/(3a^3k) = r_m^2/(3a^3D)$ and the information in Table 4.1 is sufficient to determine D, k, s_∞^*, N_0 . The values taken from [89] are shown as the first ten rows of Table 4.1, the final four (in italics) are the ones calculated after G has been determined.

The result of equation (4.21), with $G = 958$, is shown as the solid line in Figure 4.2. The dashed line represents the result predicted by the PSS model. Clearly there is excellent agreement between the two as well as with the data. This verifies the claim that the solubility may be set to a constant without greatly affecting the solution (provided the early time data is neglected).

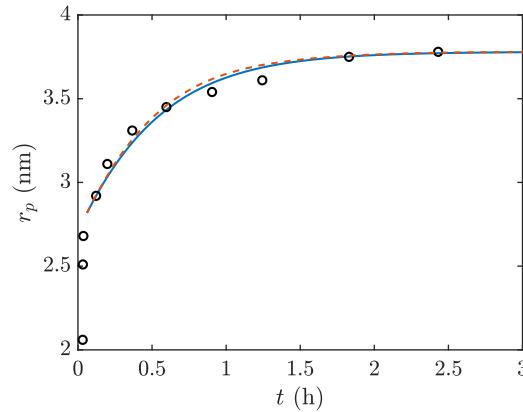


Figure 4.2: The circles represent the experimental data from Peng *et al.* [89] and the solid line the corresponding least-squares fit to the analytical solution, equation (4.21) with $G = 958$. The dashed line is the PSS model with the same value of G .

Quantity	Symbol	Value	Units
Universal gas constant	R_G	8.31	$\text{J mol}^{-1} \text{K}^{-1}$
Density	ρ_p	5816	kg.m^{-3}
Molar volume	V_M	3.29×10^{-5}	$\text{m}^3 \text{mol}^{-1}$
Molar mass	M_p	0.19	kg mol^{-1}
Solution temperature	T	573.15	K
Surface energy	σ	0.44	J mol^{-2}
Capillary length	α	6.00×10^{-9}	m
Initial bulk concentration	c_0^*	55.33	mol m^{-3}
Volume of the liquid	V	7.21×10^{-6}	m^3
Maximum particle radius	r_m	3.78×10^{-9}	m
<i>Diffusion coefficient</i>	D	3.01×10^{-18}	$\text{m}^{-2} \text{s}^{-1}$
<i>Reaction rate</i>	k	7.97×10^{-10}	m s^{-1}
<i>Solubility of bulk material</i>	s_∞^*	5.53×10^{-2}	mol m^{-3}
<i>Population density</i>	N_0	8.04×10^{21}	No. m^{-3}

Table 4.1: Physical parameters for the cadmium selenide (CdSe) nanoparticle synthesis method used by Peng *et al.* [89]. The parameters in italics are not given explicitly and are obtained via a fitting approach.

4.4.2 Validating the pseudo-steady state approximation

The PSS model is described by equations (4.17)-(4.20). Since this forms the basis for the N particle model it is important to verify its accuracy. We do this by comparison with the numerical solution of the full system (4.12)-(4.14) (referred to as the *full model*). Although we have already shown that the PSS is very well approximated by the analytical solution and that for a single crystal the solubility variation may be neglected, we must employ the PSS in the N particle model. This is because when an individual particle's solubility drops below the bulk concentration Ostwald ripening occurs. The analytical solution neglects variation in solubility, so cannot capture this behaviour.

Problems similar to the full model frequently occur in studies of phase change where it is termed the one-phase Stefan problem (one-phase because the temperature is neglected in one of the phases, this is analogous to neglecting the concentration in the crystal). Examples of one-phase problems occur in laser melting and ablation, Leidenfrost evaporation of a droplet and in supercooled materials. At the nanoscale there are many studies on nanoparticle melting and growth, see [33, 34, 81]. The nanoparticle studies are particularly relevant, since they deal with a spherical geometry and at the nanoscale the melt temperature varies in a manner similar to the variation of the solubility in the current problem. For this reason we follow the numerical scheme outlined in the studies of [33, 34]. For the numerical solution we choose a large, fixed domain (equivalent to stating δ is large and constant). The scheme involves a standard boundary immobilization transformation and then a semi-implicit finite difference scheme is applied to the resulting equations. The PSS model requires the solution of a single nonlinear ordinary differential equation, (4.20). To do this we simply use the Matlab ODE solver `ode15s`. Once r_p is determined the concentration is given by equation (4.19).

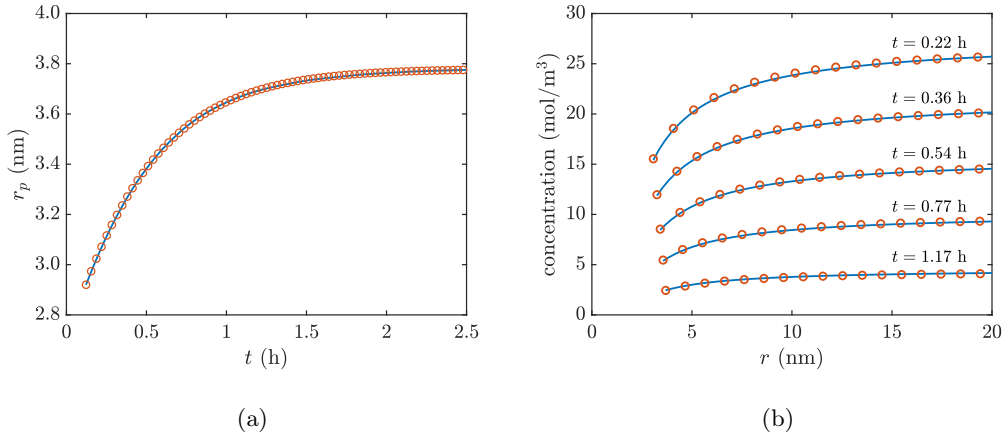


Figure 4.3: Solution of the full and the PSS models (represented by circles and by a solid line, respectively) for the growth of a single particle. Panel (a) shows the evolution of the particle radius and panel (b) the concentration of monomer around the particle at five different times.

In Figure 4.3 we compare the numerical solution of the full and PSS models using the parameters of Table 4.1, where panel (a) shows the evolution of the particle radius and panel (b) the concentration profile at five different times. In both cases the agreement

between the full and PSS models is excellent, thus justifying the use of the simpler PSS model in the N particle system. All subsequent calculations will be based on the PSS model. Panel (a) shows how the particle grows rapidly until around $t \approx 1$ hr when the growth rate decreases, subsequently the radius slowly approaches the maximum value of $r_p \simeq 3.8$ nm. This behaviour can be understood by analysing the concentration profiles presented in panel (b). The growth rate is proportional to the concentration gradient adjacent to the particle. From Figure 4.3(b) it is clear that the concentration gradient near the particle surface is relatively large at small times, leading to rapid growth. After $t \approx 1$ hr the concentration profile is practically flat, resulting in a slow growth rate.

4.4.3 Ostwald ripening with $N = 2$

With the single particle model the growth rate tends to zero as the solubility and bulk concentration approach each other. Initially all terms on the right hand side of Eq. (4.20) are positive, indicating a positive growth rate. The increase in r_p leads to a decrease in bulk concentration and the growth rate tends to zero as this concentration approaches the solubility. The analytical solution indicates that this approach is exponential and there is no mechanism for the growth rate to become negative. Hence Ostwald ripening, where a particle has a negative growth rate can only occur in a system with more than one particle. For certain materials Ostwald ripening may take a very long time and so be difficult to observe. Faraday's experiment shows time-scales on the order of decades, in [25] a broadening of the CdSe particle radii on the order 0.1nm occurs over a period of hours. To demonstrate that the current model can predict Ostwald ripening we now investigate the simplest possible case, with two particles. However, since we are using data for CdSe we anticipate a slow process.

The system is defined by equation (4.25) with $N = 2$. We take parameter values from Table 4.1 and choose initial radii 2 nm and 2.5 nm. The two governing equations may be easily solved using the Matlab ODE solver `ode15s`. Results are presented in Figure 4.4. The first figure shows the evolution of the radii for more than 25 hours. The solid line represents the evolution of the 2.5 nm particle, the dashed line is the 2 nm one. As can be seen, for small times both particles grow rapidly however, after around 1.7 hours the smaller particle starts to shrink, while the larger one grows linearly. In Figure 4.4(b) the variation of the

particle solubility and concentration is shown, solid and dashed lines correspond to the 2.5, 2nm particle's solubility respectively, while the dotted line is the bulk concentration. With reference to the variation of the radius it is clear that the rapid growth phase corresponds to a sharp decrease in the bulk concentration. Initially the solubility of each particle is below the bulk concentration and decreases as r_p increases. Ostwald ripening begins when the solubility of the smaller particle crosses the c_b curve, at $t \simeq 1.7$ h, and subsequently its size decreases. The solubility of the larger particle keeps slowly decreasing, in keeping with its slow growth, and remains below the bulk concentration until the end of the simulation. If we continued the simulation the smaller particle would eventually disappear, the rate of decrease in radius increasing with time.

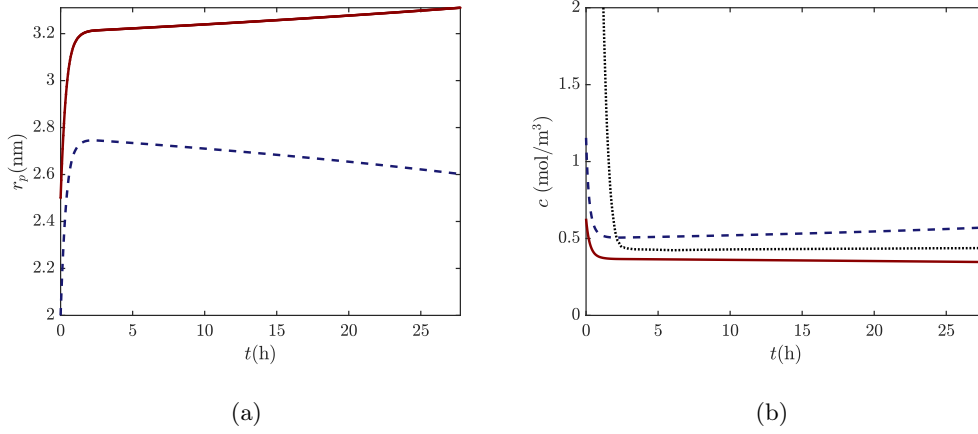


Figure 4.4: Evolution of two CdSe nanoparticles. (a) Change in time of the radii of two particles with initial radii of 2 nm (dashed line) and 2.5 nm (solid line). (b) Change in bulk concentration (dotted line) and solubilities of smaller (dashed line) and larger (solid line) particles.

4.4.4 N particles system

To simulate the experiments of [89] we consider a distribution of N nanoparticles where the initial distribution is generated by random numbers, with an initial mean radius $\bar{r}_{i,0}^*$ of 2.92 nm and a standard deviation of $\sigma_o = 8.9\%$. In the numerical solution if a particle decreases below 2 nm it is assumed to break up and all the monomer returns to the bulk concentration.

In Figure 4.5 we compare the prediction for the average radius of 10 and 1000 CdSe

particles (dashed lines) with the corresponding data of Peng *et al.* [89]. The single particle analytical solution for $r(t)$, equation (4.21), is shown as a solid line. The inset shows the difference between the N particle and analytical solution. In Figure 4.5(a) the maximum difference between the two solutions is of the order 1.5%, which decreases rapidly with time. The solution with $N = 1000$, shown in Figure 4.5(b), has a maximum difference of the order 0.15% from the analytical solution.

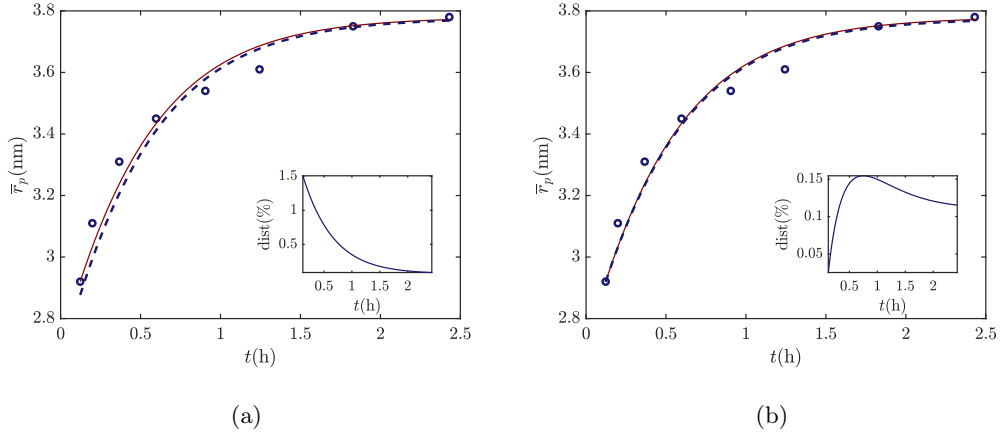


Figure 4.5: Comparison of the model for N particles (dashed lines) with experimental data from Peng *et al.*[89] (dots) using $N = 10$ in (a) and $N = 1000$ in (b). The solid lines represent the explicit solution for the one particle model, equation (4.21). The inset plots show the percentage difference between the models.

In practice N would be much higher. In Table 4.1 the population density is given as $N_0 = 8.04 \times 10^{21}$ crystals/ m^3 , so in a volume $V \approx 7 \times 10^{-6} \text{m}^3$ we would expect around 10^{16} crystals. The figure demonstrates that as N increases the solution tends to the analytical solution. Given that N is typically very high it is then clearly not necessary to solve the large system: the analytical solution is easier to understand and implement than a 10^{16} particle model. However, it is important to note that in the present example there is no significant Ostwald ripening. From Figure 4.4 we observe defocussing starts around 1.7 hours and after nearly 30 hours the radius of the smaller particle has only decreased by 7%. In the experimental data used here extra monomer is added to the solution after three hours and we stop our simulation then. So, in the absence of significant Ostwald ripening we may assume that the analytical solution may be used to predict the average evolution

of nanocrystal growth. In situations where Ostwald ripening is to be modelled some form of N particle model should be used, since this accounts for the solubility of each particle.

4.4.5 Optimal strategies for growth

For commercial applications crystal growth is a multi-stage process, with extra monomer being added whenever it is judged that the concentration is low. Generally this is an *ad-hoc* process, with no clear rules on when or how much to add. The solutions provided in the present study can help to inform this process.

Firstly, we note that equation (4.20) indicates a maximum growth rate when $c_b - s$ is maximum. This suggests maintaining a high bulk concentration. However, if too much is added the concentration will surpass the saturation level, leading to the nucleation of small crystals and a possible, undesirable, bimodal size distribution. This may be avoided since the radius is known, via equation (4.20), so the bulk concentration $c_b \approx c_0 - \beta r_p^3$ is also known. Hence at any given time we know how much monomer is in solution and consequently how much may be added.

In theory a continuous drip, which matches the rate at which monomer is lost, could be used to replace monomer and maintain the concentration at a constant high level. In practice monomer is usually added in distinct stages, our solution can determine the maximum possible amount. However, it must be noted that when using the present method, at each injection new initial conditions must be applied. This means that the initial radius for, say, the second stage would be the value at the end of the first stage and the initial time that of the injection. The value of a must be adjusted since the new initial concentration will be what remains at the end of the first stage plus what is added. This value then affects the value of G .

In Figure 4.6 we show the evolution of the radius for an experiment with similar conditions to those studied in Peng *et al.* [89]. Hence all parameter values from Table 4.1 are kept the same, with the single difference that we start with a value $c_0^* = 50 \text{ mol/m}^3$ and add 50 and 100 mol/m^3 at different times. The solid curves have an addition at 0.25 and 0.5 hours, the dashed curves after 1, 3 hours. In both cases the final radius is around 5.8nm, but in the first case this is achieved after 2 hours, in the second close to 5 hours.

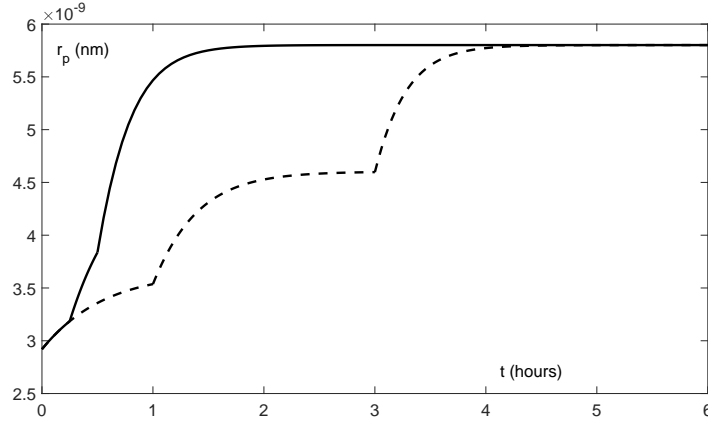


Figure 4.6: Evolution of the radius varying the time of further injections.

4.5 Conclusions

We have developed a model for the growth of a system of N particles, where N may be arbitrarily large. The model involves a system of first order nonlinear ordinary differential equations, which are easily solved using standard methods. The basis of the N particle model is the pseudo-steady approximation presented in [79] which was shown to be an excellent approximation to the full numerical solution. This model incorporates the particle solubility variation which then permits the model to capture Ostwald ripening.

The main drawback to a single particle model is that it cannot describe Ostwald ripening. By studying the system with $N = 2$ we were able to emulate Ostwald ripening on a very simple system. The method can be easily translated to any number of crystals.

By allowing N to become large and calculating the average particle radius we showed that the results approached the single particle explicit solution, which may thus be considered to represent the average growth of a large distribution of particles. A consequence of this is that the $N = 2$ model can equally well represent the average radii for an initially bimodal distribution of nanocrystals. An $N > 2$ model can represent a much larger distribution of particles.

The main advantage of the current method is that since the single particle model may be solved analytically, and this accurately describes the average radius of a distribution, then the controlling parameters are apparent. This allows us to adjust them and so optimise the

growth process. The method is easily adapted to multi-stage growth. Provided Ostwald ripening is prevented, which is the usual procedure in a controlled environment, we only have to deal with a single particle so the solution is rapid (almost instantaneous), as opposed to previous large scale, time-consuming calculations.

In future work we intend to combine this with a detailed experimental study to derive appropriate guidelines for nanocrystals production.

Part II

Drug delivery at the nanoscale

5 | Magnetic drug targeting

5.1 Introduction

Currently the main approaches in cancer therapy include surgery, chemotherapy, radiotherapy and hormone therapy [6]. However, since the latter three are non-specific their efficacy is not only reduced but sometimes the cure is more aggressive than the disease itself. There are two major disadvantages of a non-specific therapy for cancer treatment: first of all, the systemic distribution of the drug normally generates several side effects as the drugs attack healthy cells in addition to the tumour cells; secondly, the high dosage of drugs required to target malignant cells. The goal of improving the efficacy of the therapy was widely studied by researchers in the late 1970s, who proposed to use magnetic carriers to target specific areas where the disease was concentrated [86]. In order to specifically target tumours there are currently two standard techniques. The first involves the inhibition, by various means, of drug delivery to healthy non-cancerous cells while the second involves the direct conduction of drugs into the tumour site. It is now accepted that one way to achieve the second technique is by using nanoparticles to deliver the drugs directly to the tumour cells which results in minimum drug leakage into normal cells [118]. The technique of magnetically targeted drug delivery involves binding a drug to small biocompatible magnetic nanoparticles, injecting them into the bloodstream and then using a high gradient magnetic field to direct them to the target region. Once they arrive to the endothelium part near the tumour, they diffuse into the tumour tissue through and deliver the encapsulated drug molecules into tumour sites [121].

The interest in the nanoscale began thanks to the discovery that tumours have a highly

porous vasculature which allows access to nano-sized particles delivering therapeutic agents [91]. There are several types of structures, called *nanovectors*, that can be filled with anticancer drugs or can be used to attach molecules to their surface. Both methods are used for *in vivo* visualization of markers of diseases and targeted delivery of therapeutic agents in order to reduce collateral effects. The first example of successful nanovectors containing inorganic nanoparticles, like gold, are a particular lipid system called liposomes. They are FDA-approved and nowadays widely used for breast cancer treatments [87], and represent the first generation of a huge field of on-going development of drug carriers [56, 88]. A particularly interesting case is the one of metal-based nanovectors, called *nanoshells*, which are composed of a silica core surrounded by a gold layer. As explained in the first part of this thesis, gold nanoparticles can be precisely tuned in order to reach the result desired: in this case this property is used to build a gold layer of different thickness that can be selectively activated through tissue irradiation for therapeutic thermal ablation, a procedure widely performed in cancer therapy which uses heat to remove tissue by burning it [5]. In fact, each colour can be conjugated with antibodies to different molecular targets and, when irradiated, a precise map of the distribution of many molecular markers is generated [31]. Moreover, the size of the particle is crucial in the margination dynamics, which is the movement of particles in the flow toward the walls of a channel, due to the risk of being filtered out of the blood or via extravasation from a tumour [19]. It has been shown by Decuzzi *et al.* [27] how particles used for drug delivery should have a radius smaller than a critical value (which is $\approx 100\text{nm}$) to facilitate margination and interaction with the endothelium, as a result of the balance of the forces acting on the particles.

However, there are several open questions in this novel technique. From a chemical point of view, the toxicity released by nanoparticles injected in the body and the possibility of embolization of the blood vessel in the target region due to accumulation of magnetic carriers are major concerns [28]. Moreover, the characteristics of the external magnetic field (like intensity and position) is also still a topic of discussion, but it is widely recognised that it can be used only with tumours near the surface of the body and not too far from the target site [98]. At the present, there are many promising studies, both *in vivo* and *in vitro* [2, 75, 116]. To our knowledge, only a few successful trials for magnetically drug delivery on human patients have been carried on. A first study conducted a trial on 14 patients

with advanced tumours unsuccessfully treated with other methods [66]; a second one used this technique in order to improve the delivery of a magnetic targeted chemotherapy agent in the treatment of inoperable hepatocellular carcinoma [117]; finally, in the same year 11 patients were examined with MRI before and after magnetic drug targeting [61]. All this experimental studies have shown that, under particular circumstances, magnetic forces can attract particles in the region near the magnet but there is a lack of knowledge about the mechanism of this accumulation [32]. For this reason it is still difficult to scale-up the results from small animals to human.

The focus of this chapter is based on physical aspects of this technique, and in particular the delicate balance of the hydrodynamic and magnetic forces which cause the movement and directing of the particles in drug delivery systems while modelling the blood as a non-Newtonian fluid. The goal is to reach a deep understanding of the process in order to optimize the success of the therapy by controlling the motions of the nanoparticles in the bloodstream.

In the past, several authors studied the movement of particles subjected to a magnetic field in the bloodstream considering different models for the flow of the blood. In order to simplify calculations most of them used the approximation for a Newtonian fluid or the very popular power-law model. Moreover, previous studies worked mostly at microscale, which has the advantage to respond strongly to the external magnetic field (since magnetic force scales with particle volume [82]), but in this case particles tend to agglomerate during the delivery. Grief and Richardson [45] and then Richardson *et al.* [94] developed a continuum model for the motion of particles subjected to a magnetic field, both using a Newtonian flow model for the blood. In [45] it was shown, via a simple network model, that it is impossible to specifically target interior regions of the body with an external magnetic field; the magnet can be used only for targets close to the surface. The second work analysed the boundary layers in which particles tend to concentrate during the delivery. Nacev *et al.* [82] analysed this same process using a sophisticated numerical solver to simulate particle behaviour under the influence of a magnetic field using a power-law assumption for the flow of the blood in the vessels. Yue *et al.* [122] implemented a stochastic ODE model for clusters of nanoparticles in a Hagen-Poiseuille flow in order to find the optimal injection point. Cherry and Eaton [20] developed a comprehensive model for the motion of magnetic

particles using a fitted value for the viscosity from experimental data given by Brooks *et al.* [16] with a shear thinning model, then used a power-law expression for the behaviour of the fluid in the case of a dilute suspensions of microscale particles suspended in blood. Lunnoo and Puangmali [68] used a generalized power-law model for the rheology of the blood in order to investigate the parameters which play a crucial role in the magnetic drug targeting, showing how difficult it can be to keep small particles in the desired region. More recently, Rukshin *et al.* [95] developed a stochastic system of differential equations in order to simulate the behaviour of magnetic particles in small vessels, where the velocity of the blood is described by a power-law profile. They claim to simulate the movement of superparamagnetic nanoparticles, which have a radius smaller than 30nm, but then use a value of the order of 10^{-7} for the simulations. Most of the literature shows that small particles have a better chance to reach the target but a lack of accurate size determination has been found in several studies [40]. In the same year, Boghi *et al.* [13] show a complete numerical simulation of drug delivery in the blood in the coeliac trunk, where nanoparticles are dragged into the liver by an external magnetic field, considering a Newtonian fluid.

The aim of this project is to analyse the forces and the parameters involved in the process of magnetic drug delivery and to highlight the importance to consider realistic models for both the flow of the blood and the motion of the nanoparticles in it. In particular, it is crucial to consider the non-Newtonian behaviour of the blood in order to predict if particles are able to reach the desired area. A mathematical model in a 2D channel is introduced in Section 5.2. In Section 5.3, it is explained how choosing an oversimplified approximation constitutive law for the fluid in the vessel or a wrong value for the viscosity in the centre of the channel can lead to significant errors. Once obtained an accurate approximation for the behaviour of the blood in the vessels, in Section 5.4 we show how magnetic forces act on particles depending on their size. In fact, it is clear that in order to reduce the toxicity of this method, particles need to be superparamagnetic and to lose their magnetism as soon as the external magnetic field is removed. Numerical simulations by varying some key parameters are presented in Section 5.5 and conclusions are drawn.

5.2 A mathematical model for magnetic drug delivery

The physical process that we model here is related to the very promising technique of magnetic drug targeting. Drugs bound to magnetic nanoparticles are injected into the bloodstream and driven by an external magnetic field with the aim to reach the disease area. In order to model this complex process, a clear understanding of the blood circulation throughout the human body is needed. In Figure 5.1 it is shown how blood flows through a system of vessels, called the circulatory system. As the heart beats, blood full of oxygen and nutrients is carried away throughout the aorta, the main artery, to the tissues. Arteries branch several times in arterioles which become smaller as they carry blood further from the heart until becoming capillaries. At this point, they have thin walls which allow oxygen and nutrients to pass through the tissue cells. Capillaries connect the arteries with the veins, where blood flows back from the body to the heart. They become larger and larger, from being venules to reach the size of the so-called vena cava, the largest vein that brings the blood back into the heart. The average lengths (L) and widths (R) of the five types by which blood vessels are classified can be found in Table 5.1, together with the values for the aorta and the vena cava. Moreover, the average number of these vessels in the human body (N) is given.

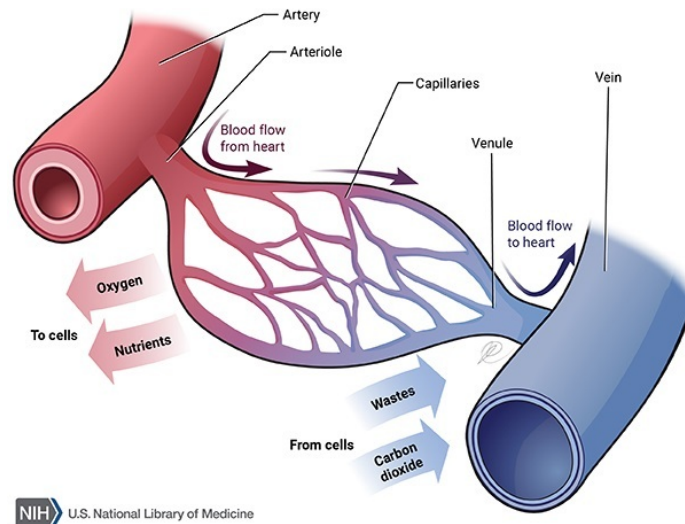


Figure 5.1: Different types of vessels in the circulatory system. Image credits to the U.S. National Library of Medicine [92].

Vessel	L (m)	R (m)	N
Aorta	0.4	1.25×10^{-2}	1
Artery	0.1	1.5×10^{-3}	159
Arteriole	7×10^{-4}	2.5×10^{-5}	5.7×10^7
Capillary	6×10^{-4}	4×10^{-6}	1.6×10^{10}
Venule	8×10^{-4}	1×10^{-5}	1.3×10^9
Vein	0.1	2.5×10^{-3}	200
Vena cava	0.22	1.5×10^{-2}	2

Table 5.1: Typical values for the various types of vessels in human body: average length (L) and width (R), estimation of the average number of a specific vessel in the circulatory system (N). All values are adapted from [38].

The main assumption that we will make in order to simplify the system of equations is that the width of the vessel is significantly smaller than its length. From the values in Table 5.1 it is clear that each type of vessel verify this property. Hence, this project is focused on the simulation of magnetically drug delivery in an artery, since many of the parameters needed for the simulation in this case have been extensively measured in literature and, therefore, it is a good example for a realistic study. However the model can be easily used to simulate different types of vessel since its dependence from their size is widely explained.

As represented in Figure 5.2, we approximate the vessel as a rectangular channel, with the width significantly smaller than its length. We also assume that the magnetic particles are injected from the left border and their motion is driven by the magnetic field generated by a magnet located below the domain which counteracts the drag force on the particles due to the blood.

A key issue in magnetic drug delivery is whether the applied magnetic forces can compete with convective blood (drag) forces that tend to wash particles away. These drag forces have different effects on the particle varying with the particles position in the blood vessel. A particle at the vessel centerline will experience a higher drag force than a particle near the wall, because the latter will be surrounded by a near zero blood velocity. The ‘no-slip’ condition is assumed at the walls, which means that the velocity of the blood is zero there.

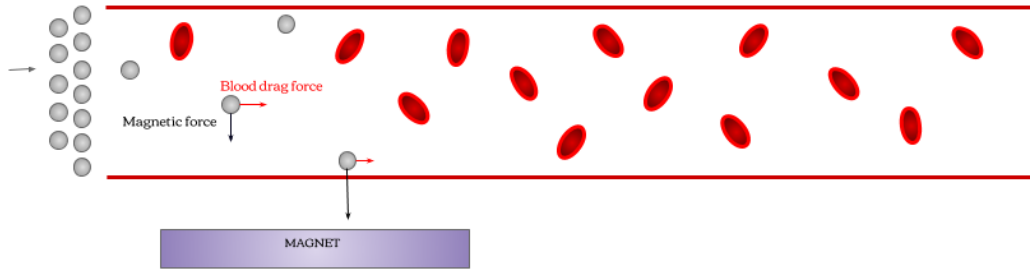


Figure 5.2: Sketch of the injection of magnetic nanoparticles in a vessel in the presence of red blood cells and subject to an magnetic field.

Therefore, a particle near the vessel wall experiences a smaller drag force and is attracted more severely by the magnetic field. Furthermore, the model takes into account the interactions and collisions between moving red blood cells (RBCs) in the bloodstream which cause a, so-called, shear-induced diffusive motion of the magnetic particles [45]. Moreover, the aggregation of RBCs strongly influences the blood flow characteristics, being the major cause of the non-Newtonian nature of blood [53]. Brownian motion can also be important due to the small size of the particles while gravity is assumed negligible.

We also have to pay attention to the rate at which the drug diffuses from the bloodstream into the extravascular space, that is the permeability of the wall which varies according to the types of the vessels. According to the definition of the Medical Subject Headings (MeSH), the vascular permeability is *the property of blood vessels that allows for the selective exchange of substances between the blood and surrounding tissues and through membranous barriers*. This, however, is not easy to measure. Also, if the drug is lipid-insoluble, that is capable of dissolving in fatty tissues, the capillary membrane permeability controls the rate at which the drug is distributed between the blood and tissue regions. The distribution of the drug is then said to be diffusion-rate limited [39].

Since blood containing nanoparticles can be considered a sort of nanofluid, its motion is usually described by a coupled set of partial differential equations describing the fluid flow, widely known as Navier-Stokes equations, and the particle concentration, whose behaviour is described by an advection-diffusion equation. The general model describing the flow of a

nanofluid in a vessel subject to an external magnetic field is then:

$$\nabla \cdot \mathbf{u}_F = 0, \quad (5.1)$$

$$\rho \left[\frac{\partial \mathbf{u}_F}{\partial t} + \mathbf{u}_F \cdot \nabla \mathbf{u}_F \right] = -\nabla p + \nabla \cdot \boldsymbol{\tau} + \mathbf{F}_F, \quad (5.2)$$

$$\frac{\partial c}{\partial t} + \nabla \cdot [(\mathbf{u}_F + \mathbf{u}_p)c] = \nabla \cdot (D \nabla c), \quad (5.3)$$

where \mathbf{u}_F is the fluid velocity, ρ is the fluid density, p is pressure, $\boldsymbol{\tau}$ is the stress tensor, \mathbf{F}_F the magnetic force acting on the fluid, c the particle concentration, \mathbf{u}_p the particle velocity and D the particle diffusion coefficient. In order to simplify the model for the blood flow we will consider \mathbf{F}_F sufficiently small and we neglect it. In fact, even if it has been shown that blood viscosity can reduce due to the magnetic field under certain circumstances (see for example [106]), natural blood has negligible magnetization [3] and its overall character is found to be paramagnetic [109]. On the wall of the vessel, the fluid obeys the no-slip condition, while the particles are assumed to be able to pass through the vessel according to some permeability coefficient κ . The particles are injected on the left of the domain (inlet) during some injection interval T_{inj} , while the end of the vessel is sufficiently far from the magnet that its effect is almost zero.

In the next sections, we will study the flow of the blood comparing different constitutive laws in a vessel and their effect on the concentration of magnetic nanoparticles.

5.2.1 The magnetic field

The interest in magnetic nanoparticles as drug carriers stems from several of their properties that are useful in medicine. The combination of the advantages of the small size with the possibility to control them via an external magnetic field which can easily penetrate human tissue makes them good candidates for drug delivery. However, an important question is how near the magnetic field has to be to the target area in order to achieve the targeting. In fact, since the magnetic gradient rapidly decreases with increasing the distance to the target, alternative methods like implant magnets or ferromagnetic microwires has been used as alternatives to external magnetic fields [68]. Moreover, the fact that due to this decreasing in distance the area where magnetic forces can compete with drag forces is limited has been one of the main difficulty in moving from animal to human trials [32].

In order to evaluate the magnetic force acting on the particles in the vessel, let us consider the Maxwell's equations for stationary or slowly varying magnetic fields:

$$\nabla \times \mathbf{H} = j, \quad (5.4)$$

$$\nabla \cdot \mathbf{B} = 0, \quad (5.5)$$

$$\mathbf{B} = \mu_0 (\mathbf{H} + \mathbf{M}), \quad (5.6)$$

where \mathbf{H} is the intensity of the magnetic field \mathbf{B} , j is the current density, μ_0 is the permeability of the vacuum and \mathbf{M} is the materials magnetization. The magnetization is usually correlated to the magnetic moment $\mathbf{m} = V_m \mathbf{M}$, where V_m the volume of the material, or it can be defined in terms of the magnetic susceptibility χ by the Clausius–Mossotti formula for a spherical particle [95]

$$\mathbf{M} = \frac{\chi}{1 + \chi/3} \mathbf{H}. \quad (5.7)$$

The susceptibility describes how the magnetization is induced in a material by the the magnetic field. Most materials display little magnetism, with a low value of χ in the range of $[10^{-6}, 10^{-1}]$ in the case of paramagnets and depends not only on the temperature but also on \mathbf{H} . As mentioned earlier, the size of the magnetic particle plays a crucial role in this physical process. In fact, only when the particle is smaller than a critical diameter (which is about 30nm), does it exhibit superparamagnetic behaviour, which is the capacity of its magnetization to be on average zero in the absence of an external magnetic field [68]. In this case, the magnetic moment of the particle is free to fluctuate in response to thermal energy while the individual atomic moments maintain their ordered state relative to each other [86].

In order to exert a magnetic force on magnetic nanoparticles in the vessels, a magnetic field gradient is required at a distance. We can define the magnetic force \mathbf{F}_{mag} on a single particle in a magnetic field \mathbf{B} as

$$\mathbf{F}_{\text{mag}} = (\mathbf{m} \cdot \nabla) \mathbf{B}, \quad (5.8)$$

that is the derivative of the magnetic field \mathbf{B} in the direction of \mathbf{m} . One possible approximation is to use the expression $\mathbf{B} = \mu_0 \mathbf{H}$ in order to rewrite equation (5.8) as

$$\mathbf{F}_{\text{mag}} = V_m \mu_0 (\mathbf{M} \cdot \nabla) \mathbf{H} = \frac{4\pi a^3}{3} \frac{\mu_0 \chi}{1 + \chi/3} (\mathbf{H} \cdot \nabla) \mathbf{H} = \frac{2\pi a^3}{3} \frac{\mu_0 \chi}{1 + \chi/3} \nabla |\mathbf{H}|^2, \quad (5.9)$$

where a is the radius of the particle and (5.7) has been applied. Equation (5.9) shows two important features of the magnetic force: first of all, it is proportional to the particle volume, which makes the nanoscale case so different from the microscale; secondly, it is proportional to the gradient of the magnetic field intensity squared, which is one of the parameters compared in several studies.

In the particular case of superparamagnetic nanoparticles, the magnetic moment depends on the local magnetic flux density and we can use the Langevin function

$$\mathbf{m} = \frac{m_{\text{sat}} \mathbf{B}}{|\mathbf{B}|} L(|\mathbf{B}|) = \frac{m_{\text{sat}} \mathbf{B}}{|\mathbf{B}|} \left[\coth\left(\frac{m_{\text{sat}} |\mathbf{B}|}{k_B T}\right) - \frac{k_B T}{m_{\text{sat}} |\mathbf{B}|} \right] \quad (5.10)$$

where k_B is Boltzmann's constant and T is the absolute temperature. The variable m_{sat} is the magnetic saturation of the particle given by

$$m_{\text{sat}} = \frac{4\pi a^3}{3} \rho M_{\text{sat}}, \quad (5.11)$$

where ρ is the density of the magnetic particles and M_{sat} is the mass saturation magnetization. Grief and Richardson [45] have shown that for sufficiently weak fields on superparamagnetic particles we can consider the approximation

$$\mathbf{F}_{\text{mag}} \approx \frac{m_{\text{sat}}^2}{3k_B T} (\mathbf{B} \cdot \nabla) \mathbf{B} = \frac{m_{\text{sat}}^2}{6k_B T} \nabla |\mathbf{B}|^2. \quad (5.12)$$

Nacev *et al.* [82] have shown that for a magnet held at a long distance compared to the width of the vessel, we can assume the magnetic force is approximately constant in the vertical direction which avoid the need to solve Maxwell's equations. Richardson *et al.* [94], for example, use a constant value for the magnetic force given by

$$F_0 = \frac{4}{3} \pi a^3 \rho \mathbf{M} \Upsilon B_g, \quad (5.13)$$

where Υ is the magnetite volume fraction and B_g is the gradient magnetic field. This is what we are going to assume in this work.

5.3 Blood as a non-Newtonian fluid

If we imagine the flow of the blood in a reduced space, it is clear that its behaviour will be more complex than a simpler fluid such as water. To understand the reason of this

complexity, we have to study what is defined as the viscosity of a fluid. In fluid dynamics, the viscosity of the fluid is a measure of its resistance to deformation by shear stress. We can note that in a Newtonian fluid

$$\boldsymbol{\tau} = \mu (\nabla \mathbf{u} + \nabla \mathbf{u}^T), \quad (5.14)$$

the shear stress $\boldsymbol{\tau}$ is proportional to the strain. According to Newton's law of viscosity, this momentum flow occurs across a velocity gradient, and the magnitude of the corresponding momentum flux is determined by the viscosity μ , which is constant.

We can define a Newtonian fluid under constant temperature and pressure following the description from Owen and Phillips [84]:

- The only stress generated in simple shear flow is the shear stress τ , the two normal stresses being zero.
- The shear viscosity does not vary with shear rate.
- The viscosity is constant with respect to the time of shearing and the stress in the liquid falls to zero immediately after the shearing is stopped.
- The viscosities measured in different types of deformation are always in a simple proportion to one another.

Any liquid that deviates from the above behaviour is said to be *non-Newtonian*. Typical examples of non-Newtonian fluids in nature are most of the body fluids, such as blood, saliva, eye fluid, as well as many manufactured ones, such as toothpaste, paints, etc.

In particular, blood is a concentrated suspension of particles in plasma, which is mainly made of water. There are three most important particles that constitute blood: red blood cells (or erythrocytes), white cells (or leukocytes) and platelets (or thrombocytes). The first ones, which are the most numerous, are the main responsible for the mechanical properties of the blood [38]. In fact, their tendency to form (and then break down) 3D microstructures at low shear rates and to align to the flow at high shear rates cause the blood's shear thinning behaviour, characterized by the monotonic decrease of the viscosity that tends to some limit for very high shear-rates [39]. In the case of blood, the formed structures lead to significant changes in its rheological properties and several models have been developed during the past

50 years in order to catch the complexity of this behaviour (some examples can be found in [8, 21, 22, 50, 53, 99]). However, none of those models has been universally accepted.

In mathematical terms, we define a fluid as non-Newtonian if the extra-stress tensor cannot be expressed as linear function of the components of the velocity gradient. The nonlinear relation between the shear stress and shear rate can be written as

$$\boldsymbol{\tau} = \eta(\dot{\gamma})\dot{\gamma}, \quad (5.15)$$

where $\eta(\dot{\gamma})$ is the viscosity and

$$\dot{\gamma} = (2e_{ij}e_{ij})^{1/2} = \left[\frac{1}{2} \left(\frac{\partial u_i}{\partial x_j} + \frac{\partial u_j}{\partial x_i} \right) \left(\frac{\partial u_i}{\partial x_j} + \frac{\partial u_j}{\partial x_i} \right) \right]^{1/2} \quad (5.16)$$

is the shear rate. For shear thinning fluids η is approximated by constant value as the shear rate tends to zero. This indicates a Newtonian behaviour at very low shear rates. As the shear rate is increased the viscosity varies in a non-linear manner until it reaches a second plateau value η_∞ , where the fluid behaviour can be considered Newtonian again.

The aim of this section is to compare different types of non-Newtonian fluids, focusing on the accuracy of the approximation when varying $\eta(\dot{\gamma})$. In particular, three famous models for a non-Newtonian fluid are compared with the Newtonian case. These are:

1. Power-law model

The power-law model describes the viscosity by

$$\eta_p(\dot{\gamma}) = m |\dot{\gamma}|^{n_p-1}, \quad (5.17)$$

where m is constant and $\dot{\gamma}$ is the shear rate. If $n_p < 1$ the fluid is pseudoplastic or shear thinning and if $n_p > 1$ it is dilatant or shear thickening. If $n_p = 1$ we obtain the Newtonian viscosity.

2. Carreau model

The Carreau model describes the viscosity by

$$\eta_c(\dot{\gamma}) = \eta_\infty + (\eta_0 - \eta_\infty) [1 + \lambda^2 \dot{\gamma}^2]^{(n_c-1)/2}, \quad (5.18)$$

where λ is a constant and η_0 and η_∞ are the limiting viscosities at low and high shear rates, respectively. This model is very accurate to predict the shear thinning behaviour due to its

ability to predict the two Newtonian plateaux values and the intermediate region observed in experiments.

3. Ellis model

The Ellis model describes the viscosity in terms of shear stress

$$\frac{1}{\eta_e} = \frac{1}{\eta_0} \left(1 + \left| \frac{\tau}{\tau_{1/2}} \right|^{\alpha-1} \right), \quad (5.19)$$

where η_0 is the viscosity at zero shear and $\tau_{1/2}$ is the shear stress at which the viscosity is $\eta_0/2$. We note that this model cannot predict the viscosity in the second transition region to the Newtonian plateaux value η_∞ . However, it is still very accurate for blood simulations since very high level of shear strain are not reached.

In Figure 5.3 it is shown the behaviour of the models explained above in a logarithmic scale.

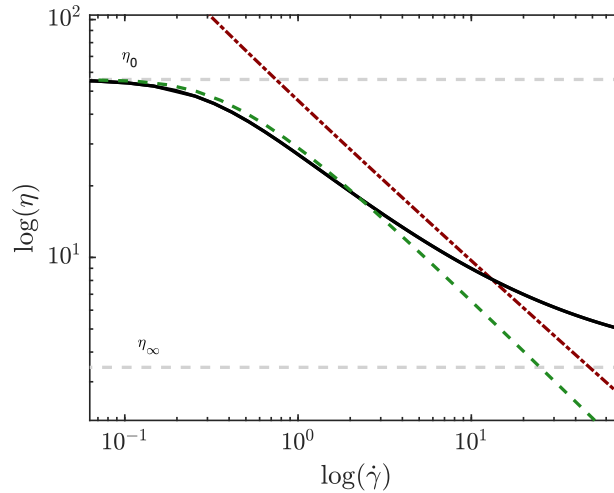


Figure 5.3: The viscosity/shear rate plot in logarithmic scale for the power law (red dotted-dashed line), the Carreau (black solid line) and the Ellis models (green dashed line). The light grey dashed lines represents the constant limit viscosities η_0 and η_∞ .

Several theoretical studies to compare the accuracy of these models have been made considering different types of fluids (see for example [52, 76, 100]). Typical values for the blood case can be found in Table 5.2 and will be used in the simulations.

In the next section we compare the results obtained from the different models and demonstrate the importance of choosing the right model for the blood flowing under the influence of an external magnetic force.

Quantity	Symbol	Value	Units	References
Newtonian viscosity	μ	0.00345	Pa s	[52]
Power-law viscosity	m	0.0035	Pa s	[76]
Power-law exponent	n_p	0.3568	No.	[76]
Carreau coefficient	λ	3.313	No.	[39]
Carreau viscosity at low shear rates	η_0	0.056	Pa s	[39]
Carreau viscosity at high shear rates	η_∞	0.00345	Pa s	[39]
Carreau exponent	n_c	0.3568	No.	[39]
Ellis viscosity at low shear rate	η_0	0.056	Pa s	[76]
Ellis shear stress at $\eta_0/2$	β	0.026	Pa	[76]
Ellis exponent	α	3.4	No.	[76]

Table 5.2: Typical parameters for the blood flow equations for each model.

5.3.1 Governing equations and nondimensionalisation

In order to approximate the physical behaviour, we study the motion of the blood in a vessel assuming that the vessel is a rectangular domain of length L and width $2R$, where $R \ll L$. Lubrication theory can describe the flow when the diameter of the vessel is significantly smaller than its length [83]. We will consider the lubrication model a good approximation of the problem since all the vessels in the circulatory system comply this assumption, as we can see from Table 5.1. As briefly introduced in Section 5.2, the flow is governed by the Navier-Stokes equations (5.1)–(5.2). Equation (5.1) is the continuity equation and equation (5.2) is the conservation of momentum. In our domain, the equations become:

$$\frac{\partial u}{\partial x} + \frac{\partial v}{\partial y} = 0, \quad (5.20)$$

$$\frac{\partial u}{\partial t} + u \frac{\partial u}{\partial x} + v \frac{\partial u}{\partial y} = -\frac{1}{\rho} \frac{\partial p}{\partial x} + \frac{1}{\rho} \left[\frac{\partial \tau_{xx}}{\partial x} + \frac{\partial \tau_{yx}}{\partial y} \right], \quad (5.21)$$

$$\frac{\partial v}{\partial t} + u \frac{\partial v}{\partial x} + v \frac{\partial v}{\partial y} = -\frac{1}{\rho} \frac{\partial p}{\partial y} + \frac{1}{\rho} \left[\frac{\partial \tau_{xy}}{\partial x} + \frac{\partial \tau_{yy}}{\partial y} \right]. \quad (5.22)$$

The velocity of the fluid is subject to the no-slip conditions at the vessel wall, so the fluid has zero velocity at $y = \pm R$. We compare three models where blood is consider as a different non-Newtonian fluid. In order to understand the order of magnitude of the terms in equations (5.20)–(5.22), we proceed with a standard non-dimensionalisation process for the steady state flow. Consider the non-dimensional variables

$$x = L\hat{x}, \quad y = R\hat{y}, \quad u = U\hat{u}, \quad v = V\hat{v}, \quad p = P\hat{p}, \quad \tau = \mathcal{T}\hat{\tau}. \quad (5.23)$$

Substituting (5.23) into (5.20) and dropping the hats, we have

$$\frac{U}{L} \frac{\partial \hat{u}}{\partial \hat{x}} + \frac{V}{R} \frac{\partial \hat{v}}{\partial \hat{y}} = 0 \quad (5.24)$$

and rearranging the terms we obtain

$$\frac{R}{L} \frac{\partial \hat{u}}{\partial \hat{x}} + \frac{V}{U} \frac{\partial \hat{v}}{\partial \hat{y}} = 0. \quad (5.25)$$

From (5.25) it is clear that we can balance the equation setting $V = \varepsilon U$, where $\varepsilon := R/L \ll 1$. This suggests that there are very small changes in the y direction. Hence, the nondimensional continuity equation is

$$\frac{\partial \hat{u}}{\partial \hat{x}} + \frac{\partial \hat{v}}{\partial \hat{y}} = 0. \quad (5.26)$$

Substituting (5.23) into (5.21), we have

$$\frac{U^2}{L} \hat{u} \frac{\partial \hat{u}}{\partial \hat{x}} + \frac{VU}{R} \hat{v} \frac{\partial \hat{u}}{\partial \hat{y}} = -\frac{P}{\rho L} \frac{\partial \hat{p}}{\partial \hat{x}} + \frac{\mathcal{T}}{\rho} \left[\frac{1}{L} \frac{\partial \hat{\tau}_{\hat{x}\hat{x}}}{\partial \hat{x}} + \frac{1}{R} \frac{\partial \hat{\tau}_{\hat{y}\hat{x}}}{\partial \hat{y}} \right]. \quad (5.27)$$

Considering $V = \varepsilon U$ and choosing $P = L\mathcal{T}/R$, we can write

$$\varepsilon U^2 \left[\hat{u} \frac{\partial \hat{u}}{\partial \hat{x}} + \hat{v} \frac{\partial \hat{u}}{\partial \hat{y}} \right] = \frac{\mathcal{T}}{\rho} \left[-\frac{\partial \hat{p}}{\partial \hat{x}} + \varepsilon \frac{\partial \hat{\tau}_{\hat{x}\hat{x}}}{\partial \hat{x}} + \frac{\partial \hat{\tau}_{\hat{y}\hat{x}}}{\partial \hat{y}} \right] \quad (5.28)$$

and making the the further assumption

$$\frac{\varepsilon U^2 \rho}{\mathcal{T}} \ll 1, \quad (5.29)$$

at leading order we can neglect most of the terms obtaining

$$\frac{\partial \hat{p}}{\partial \hat{x}} = \frac{\partial \hat{\tau}_{\hat{y}\hat{x}}}{\partial \hat{y}}. \quad (5.30)$$

Notice that equation (5.29) is equivalent to assume that the reduced Reynolds number is small for the classical lubrication theory [83]. Following the same idea we can neglect almost all the terms of equation (5.22), since we have

$$\varepsilon^3 U^2 \left[\hat{u} \frac{\partial \hat{v}}{\partial \hat{x}} + \hat{v} \frac{\partial \hat{v}}{\partial \hat{y}} \right] = \frac{\mathcal{T}}{\rho} \left[-\frac{\partial \hat{p}}{\partial \hat{y}} + \varepsilon^2 \frac{\partial \hat{\tau}_{\hat{x}\hat{y}}}{\partial \hat{x}} + \varepsilon \frac{\partial \hat{\tau}_{\hat{y}\hat{y}}}{\partial \hat{y}} \right]. \quad (5.31)$$

Therefore, dropping the hats, the non-dimensional system (5.20)–(5.22) at the leading order can be written as

$$\frac{\partial u}{\partial x} + \frac{\partial v}{\partial y} = 0 \quad (5.32)$$

$$\frac{\partial p}{\partial x} = \frac{\partial \tau_{yx}}{\partial y} \quad (5.33)$$

$$\frac{\partial p}{\partial y} = 0 \quad (5.34)$$

which is a much simpler problem.

The final non-dimensional scales are $V = \varepsilon U$ and $P = \mathcal{T}/\varepsilon$, where \mathcal{T} depends on the fluid chosen. That is, equations (5.20)–(5.22) will differ in the only term in the shear tensor that appears in the equations, which is τ_{yx} . In this case we assume the shear rate given by definition as the gradient of the velocity as in equation (5.16) and we are considering that the fluid fluctuations in the x -direction are negligible due to the particular geometry, which means $\dot{\gamma} \approx |u_y|$.

In the simple case of a *Newtonian* fluid, the shear stress (5.14) can be written as

$$\tau_{yx} = \mu \left| \frac{\partial u}{\partial y} \right|, \quad (5.35)$$

where μ is constant.

For the *power law* model (5.17), we have

$$\tau_{yx} = m \left| \frac{\partial u}{\partial y} \right|^{n_p}, \quad (5.36)$$

where m is a constant.

For the *Carreau* model (5.18), then

$$\tau_{yx} = \eta_\infty + (\eta_0 - \eta_\infty) \left(1 + \lambda^2 \left| \frac{\partial u}{\partial y} \right|^2 \right)^{\frac{n_c - 1}{2}} \left| \frac{\partial u}{\partial y} \right|, \quad (5.37)$$

where η_0 is the initial shear rate and η_∞ the equilibrium shear rate.

For the *Ellis* model (5.19), we have an implicit equation relating the viscosity with the stress-tensor

$$\frac{1}{\eta_e} = \frac{1}{\eta_0} \left(1 + \left| \frac{\tau_{yx}}{\beta} \right|^{\alpha-1} \right) \quad (5.38)$$

where η_0 is the constant viscosity at zero shear and β is the value of τ_{yx} when $\eta = \eta_0/2$. In this case, we will use the value fitted in [76].

Therefore, we will consider

$$\mathcal{T} = \begin{cases} \mu \frac{U}{R} & \text{if we choose } \tau \text{ as in (5.35),} \\ m \left(\frac{U}{R} \right)^{n_p} & \text{if we choose } \tau \text{ as in (5.36),} \\ \eta_0 \left(\frac{U}{R} \right)^{n_c} & \text{if we choose } \tau \text{ as in (5.37),} \\ \eta_0 \left(\frac{U}{R} \right)^{\alpha} & \text{if we choose } \tau \text{ as in (5.38).} \end{cases} \quad (5.39)$$

5.3.2 Comparison of the models

In order to choose the most accurate non-Newtonian law for our physical problem we start from the simplest model for a Newtonian fluid. This was used in several previous works in order to simplify the calculation. We then compare the result with more complex and more accurate models with a non-Newtonian fluid. In all cases we consider a Hagen-Poiseuille flow in a channel, which is driven by a pressure gradient $\Delta p/L$. Since the movement of the fluid in the y -direction is quite small compared with the x -direction, we will approximate our solution by a uni-directional flow with $u_x = 0$. Moreover, the flow has a constant volumetric flow rate Q .

The Newtonian fluid model

The solution for the simplest model that we can use is given by solving equations (5.32)–(5.34) where the shear-stress is described by (5.35). Since equation (5.34) implies that the pressure does not vary with y , integrating (5.33) twice with respect to y , we can find

$$u(y) = \frac{1}{2\mu} \left(-\frac{\partial p}{\partial x} \right) (R^2 - y^2). \quad (5.40)$$

Therefore, we can consider the flux

$$Q = \int_{-R}^R u(y) dy = \left(-\frac{\partial p}{\partial x} \right) \frac{2R^3}{3\mu}. \quad (5.41)$$

and, since mass is conserved, Q is constant. Hence, we can write

$$\frac{\partial p}{\partial x} = -\frac{3\mu Q}{2R^3}, \quad (5.42)$$

and substitute this expression in (5.40), obtaining the velocity as a function of the flux

$$u(y) = \frac{1}{2\mu} \left(\frac{3\mu Q}{2R^3} \right) (R^2 - y^2) = \frac{3Q}{4R^3} (R^2 - y^2). \quad (5.43)$$

The power law model

The steady state equations of the motion of a non-Newtonian flow, considering the power-law form for the viscosity, equation (5.33) is now replaced with

$$\frac{\partial p}{\partial x} = \frac{\partial}{\partial y} \left(m \left| \frac{\partial u}{\partial y} \right|^n \right). \quad (5.44)$$

Considering $u_y|_{y=0} = 0$ and the no-slip condition at $y = \pm R$, we can integrate (5.44) twice with respect to y and obtain the solution for the velocity

$$u(y) = \left(-\frac{1}{m} \frac{\partial p}{\partial x} \right)^{\frac{1}{n}} \left(\frac{n}{n+1} \right) \left(R^{\frac{n+1}{n}} - |y|^{\frac{n+1}{n}} \right). \quad (5.45)$$

Similarly to the Newtonian flow, we can find that Q is given by

$$Q = \int_{-R}^R u \, dy = \left(-\frac{1}{m} \frac{\partial p}{\partial x} \right)^{\frac{1}{n}} \left(\frac{n}{2n+1} \right) R^{\frac{2n+1}{n}}. \quad (5.46)$$

Therefore, we can write

$$\left(-\frac{1}{m} \frac{\partial p}{\partial x} \right)^{\frac{1}{n}} = \left(\frac{2n+1}{n} \right) \frac{Q}{R^{\frac{2n+1}{n}}}, \quad (5.47)$$

and this gives the velocity as function of the flux

$$u(y) = \frac{Q}{R^{\frac{2n+1}{n}}} \left(\frac{2n+1}{2n+2} \right) \left(R^{\frac{n+1}{n}} - |y|^{\frac{n+1}{n}} \right). \quad (5.48)$$

One of the main advantages of this model is that it is easy to obtain the analytical solution to the governing equation. However, there are two major disadvantages with make it appropriate for the blood modelling: the viscosity is unbounded as $\dot{\gamma} \rightarrow 0$ and the limit as $\dot{\gamma} \rightarrow \infty$ is zero.

The Carreau model

Choosing the Carreau model for the viscosity (5.37), the equations of the flow are reduced to (5.32) and (5.34) coupled with

$$\frac{\partial p}{\partial x} = \frac{\partial}{\partial y} \left[\eta_{\infty} + (\eta_0 - \eta_{\infty}) \left(1 + \lambda^2 \left| \frac{\partial u}{\partial y} \right|^2 \right)^{\frac{n-1}{2}} \left| \frac{\partial u}{\partial y} \right| \right]. \quad (5.49)$$

This expression cannot be integrated analytically and we will have to solve it numerically via the in-built `bvp5c` function in MATLAB.

The Ellis model

When choosing the Ellis model (5.38), the equations of the flow are (5.32) and (5.34) coupled with

$$\frac{\partial u}{\partial y} = \left(\frac{\partial p}{\partial x} \frac{1}{\eta_0} \right) \left[1 + \left| \left(\frac{\partial p}{\partial x} \right) \frac{y}{\beta} \right|^{\alpha-1} \right] y. \quad (5.50)$$

Following [76], assuming $u_y(0) = 0$, we can write an explicit expression for the velocity of the fluid

$$u(y) = \frac{1}{\eta_0} \frac{\partial p}{\partial x} \left[\frac{R^2 - |y|^2}{2} + \left(\frac{1}{\beta} \frac{\partial p}{\partial x} \right)^{\alpha-1} \frac{R^{\alpha+1} - |y|^{\alpha+1}}{\alpha + 1} \right], \quad (5.51)$$

where η_0 is the viscosity at low shear rate. The flux is then calculated by

$$Q = \frac{1}{\eta_0} \frac{\partial p}{\partial x} \left[\frac{R^3}{3} + \left(\frac{1}{\beta} \frac{\partial p}{\partial x} \right)^{\alpha-1} \frac{R^{\alpha+2}}{\alpha + 2} \right], \quad (5.52)$$

which gives only one real solution for the pressure gradient.

5.3.3 Velocity and viscosity

In order to compare the four models and their velocity field we have to pay attention to the choice of the parameter values. As already explained, the viscosity strongly depends on temperature, so for the whole chapter we use parameters consistent with temperature equal to 37°C, which is a reasonable choice for the human body.

The geometry parameters are common for all the models and represents an artery with length and width as in Table 5.1. The flow entering in a small artery can be approximated by $Q \approx 1.9 \times 10^{-6} \text{ m}^3/\text{s}$ [39]. Therefore, the pressure gradient driven the flow is obtained from either (5.42), (5.47) or (5.52). The rest of parameters used for the simulations of

the velocity and of the viscosity in the vessel are listed in Table 5.2. The parameters for the Newtonian, power-law and Carreau models are widely used in the literature (see for example [22, 38, 52]), while the parameters for Ellis model are taken from [76].

The velocity profiles and the corresponding viscosity profiles for blood obtained from the four different models of Section 5.3.2 are compared in Figures 5.4(a) and 5.4(b), respectively. We can observe that, even if a good agreement for the velocity behaviours is observed, the relative viscosities can differ significantly. For the purpose of this project, the value for the viscosity of the blood will be crucial in the calculation of the velocity of the particles which will determinate whether the drug is able to reach the wall of the vessel or not. Figure 5.4(b) shows clearly that, for example, the viscosity of the power-law model, represented by the red dashed-dotted line, tends to infinity as $y \rightarrow 0$ while the other viscosities have a very different value there. Both Ellis and Carreau models give similar approximations for the blood flow given their capacity to catch its shear thinning behaviour. The Carreau model is generally preferred due to its ability to predict both Newtonian plateaux but, in the cases when high shear rates are not reached and considering this particular geometry, the Ellis model can be treated analytically, which is a powerful tool.

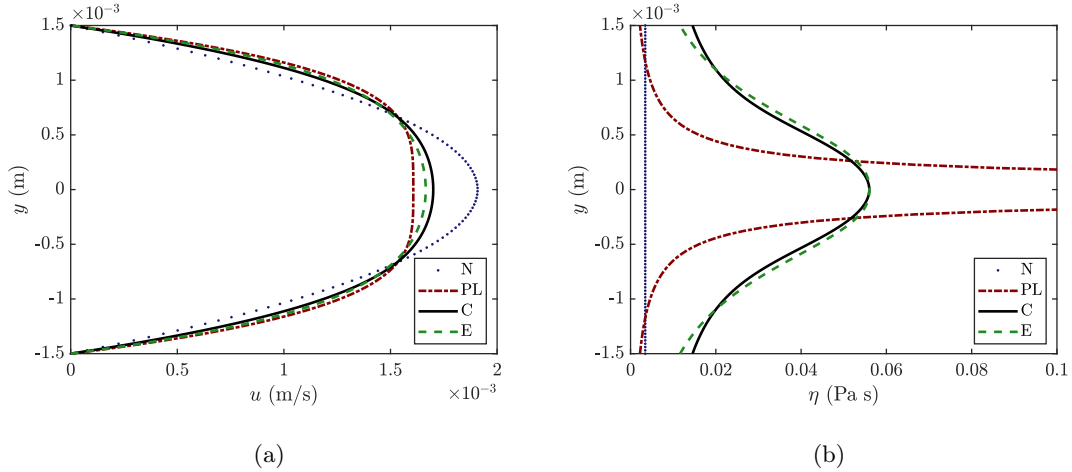


Figure 5.4: Comparison of (a) velocity and (b) viscosity profiles of Newtonian (represented by the letter N and the blue dotted line), power-law (represented by PL and the red dashed-dotted line), Carreau (represented by the letter C and the black solid line) and Ellis model (represented by the letter E and the green dashed line).

5.4 Concentration of nanoparticles in a non-Newtonian flow subject to an external magnetic field

The behaviour of the concentration of magnetic nanoparticles in the bloodstream is obtained following the continuum model developed by Grief and Richardson [45]. The governing equation describing the motion of magnetic particles in the blood stream is an advection-diffusion equation for the particle concentration $c(x, y, t)$:

$$\frac{\partial c}{\partial t} + \nabla \cdot [(\mathbf{u}_F + \mathbf{u}_p)c] = \nabla \cdot (D \nabla c) \quad (5.53)$$

where \mathbf{u}_F is the fluid velocity given by the solution of (5.32)–(5.34), \mathbf{u}_p is the particle velocity and D is the diffusion coefficient. We can decouple equation (5.53) from the equations for the flow because we assume that we are in a dilute limit where the particles concentration does not affect the flow.

The diffusive character of the equation is given by the contributions of the Brownian motion, which is the random motion of particles under thermal fluctuations, and the shear-induced diffusion, which is due to the fact that the red blood cells suspended in plasma collide with each other causing random motion with a diffusive character. As recently demonstrated by Liu and coworkers [64, 65] via a lattice-Boltzmann based multiscale simulation, the diffusion due to the Brownian motion in the case of nanoparticles transport in a small vessel can be important and, in some cases, even the predominant diffusion process. Using the Stokes-Einstein equation for the diffusion of spherical particles through a shear thinning fluid [39], we can write the Brownian diffusion coefficient as

$$D_{\text{Br}} = \frac{k_B T}{6\pi \eta(\dot{\gamma}) a}, \quad (5.54)$$

where k_B is Boltzmann constant, T the absolute temperature, $\eta(\dot{\gamma})$ is the viscosity of the blood (which depends on the model chosen) and a the particle radius. On the other hand, the shear-induced diffusion contribution can be approximated by

$$D_{\text{sh}} = K_{\text{sh}} (r_{\text{RBC}})^2 \dot{\gamma}, \quad (5.55)$$

where K_{sh} is a dimensionless coefficient that depends on the blood cell concentrations, r_{RBC} is the red blood cell radius and $\dot{\gamma}$ is the fluid shear rate defined in (5.16). The coefficient

K_{sh} is difficult to measure but the value used in Table 5.3 is considered representative in literature [45]. Hence, the total diffusion will be $D_{\text{tot}} = D_{\text{Br}} + D_{\text{sh}}$, obtaining:

$$\mathbf{J}_{\text{diff}} = -D_{\text{tot}} \nabla c = - \left(\frac{k_{\text{B}} T}{6\pi \eta(\dot{\gamma}) a} + K_{\text{sh}} (r_{\text{RBC}})^2 \dot{\gamma} \right) \nabla c. \quad (5.56)$$

The particle velocity is found by balancing hydrodynamic and magnetic forces. We can use the definition of the Stokes drag, which is the force of viscosity on a spherical particle of radius a moving through a viscous fluid, which is

$$\mathbf{F}_{\text{St}} = 6\pi a \eta(\dot{\gamma}) \mathbf{u}_p, \quad (5.57)$$

where $\eta(\dot{\gamma})$ depends on the model chosen for the blood. The particles reaches its equilibrium velocity when \mathbf{F}_{St} balances the magnetic force \mathbf{F}_{mag} and this leads us to the expression

$$\mathbf{u}_p = \frac{\mathbf{F}_{\text{mag}}}{6\pi a \eta(\dot{\gamma})}. \quad (5.58)$$

Hence, finally the governing equation can be written as

$$\frac{\partial c}{\partial t} + \nabla \cdot (\mathbf{u}_{\text{tot}} c) = \nabla \cdot (D_{\text{tot}} \nabla c), \quad (5.59)$$

where $\mathbf{u}_{\text{tot}} = \mathbf{u}_F + \mathbf{u}_p$.

As introduced in Section 5.2.1, we can consider $\mathbf{u}_p = (0, v_p(y))$ for a magnet situated at a long distance compared to the vessel width. Considering that the particles can flow out of the vessel through the walls with a certain vascular permeability κ , we will impose Robin boundary conditions at the top and the bottom of the channel of the form

$$\left(v_p c - D_{\text{tot}} \frac{\partial c}{\partial y} \right) \Big|_{y=\pm R} = \kappa c|_{y=\pm R}. \quad (5.60)$$

We also need to specify the inlet and the outlet conditions. Assuming that the flux entering in the channel is constant and equal to the inlet concentration c_{in} for a certain interval of time $[0, T_{\text{inj}}]$, we set

$$c(x, y, t)|_{x=0} = \begin{cases} c_{\text{in}} & \text{if } 0 \leq t \leq T_{\text{inj}}, \\ 0 & \text{otherwise,} \end{cases} \quad (5.61)$$

and

$$\left(u_F c - D_{\text{tot}} \frac{\partial c}{\partial x} \right) \Big|_{x=L} = 0, \quad (5.62)$$

assuming that at the end of the channel we are sufficiently far from the magnet that its effect is almost zero. The initial value problem is well-posed with the initial condition $c(x, y, 0) = 0$.

5.4.1 Nondimensionalisation of the advection-diffusion equation

As already noted in Section 5.3.1, due to the particular geometry chosen, in the y -direction the movement of the fluid is quite small compared to the horizontal direction. In order to simplify our problem we then assume in the analysis of the particle concentration that the flow of the blood is horizontal and we can write $\mathbf{u}_F = (u_F(y), 0)$. Moreover, since $\mathbf{u}_p = (0, v_p(y))$, the governing equation (5.59) becomes

$$\frac{\partial c}{\partial t} + u_F \frac{\partial c}{\partial x} + \frac{\partial(v_p c)}{\partial y} = D_{\text{tot}} \frac{\partial^2 c}{\partial x^2} + \frac{\partial}{\partial y} \left(D_{\text{tot}} \frac{\partial c}{\partial y} \right), \quad (5.63)$$

since $D_{\text{tot}} = D_{\text{tot}}(y)$. In this case, we will study the unsteady advection-diffusion equation for the concentration, which will change more quickly in time with respect to the fluid. Substituting the non-dimensional variables detailed in (5.23) and

$$t = T \hat{t}, \quad c = c_0 \hat{c}, \quad u_F = U \hat{u}_F, \quad v_p = W \hat{v}_p, \quad D_{\text{tot}} = D \hat{D}_{\text{tot}}, \quad (5.64)$$

into (5.63) we obtain

$$\frac{c_0}{T} \frac{\partial \hat{c}}{\partial \hat{t}} + \frac{U c_0}{L} \hat{u}_F \frac{\partial \hat{c}}{\partial \hat{x}} + \frac{W c_0}{R} \frac{\partial(\hat{v}_p \hat{c})}{\partial \hat{y}} = \frac{D c_0}{L^2} \left(\hat{D}_{\text{tot}} \frac{\partial^2 \hat{c}}{\partial \hat{x}^2} \right) + \frac{D c_0}{R^2} \frac{\partial}{\partial \hat{y}} \left(\hat{D}_{\text{tot}} \frac{\partial \hat{c}}{\partial \hat{y}} \right). \quad (5.65)$$

Rearranging the terms, choosing $T = L/U$ in order to balance the time derivative with the advection term, we can write

$$\frac{\partial \hat{c}}{\partial \hat{t}} + \hat{u}_F \frac{\partial \hat{c}}{\partial \hat{x}} + \frac{\delta}{\varepsilon} \frac{\partial(\hat{v}_p \hat{c})}{\partial \hat{y}} = \frac{1}{\varepsilon \text{Pe}} \left[\varepsilon^2 \left(\hat{D}_{\text{tot}} \frac{\partial^2 \hat{c}}{\partial \hat{x}^2} \right) + \frac{\partial}{\partial \hat{y}} \left(\hat{D}_{\text{tot}} \frac{\partial \hat{c}}{\partial \hat{y}} \right) \right], \quad (5.66)$$

where $\delta = W/U$ and $\text{Pe} = D/(RU)$ is the Péclet number and depends on the model chosen since the Brownian diffusion is a function of $\eta(\dot{\gamma})$. According to the values in Table 5.3, $\mathcal{O}(\varepsilon \text{Pe})^{-1} \approx [10^{-6}, 10^{-5}]$ depending on the fluid chosen, while $\varepsilon = \mathcal{O}(10^{-2})$, hence both terms of the right side of the equation are quite small. Therefore, as commonly happens, the advective terms are dominant and when analysing them, it is important to understand the order of magnitude of the fraction δ/ε . In particular we can distinguish three regions in the domain (symmetric with respect to the center of the vessel): a central region where $\mathcal{O}(\delta) < \mathcal{O}(\varepsilon)$, which is the broadest one where the drag force is winning over the magnetic force; a second region where $\mathcal{O}(\delta) \approx \mathcal{O}(\varepsilon)$ where both advective terms are order one and balance each other; finally, very near to the wall of the vessel, we can find a narrow boundary layer where $\mathcal{O}(\delta) > \mathcal{O}(\varepsilon)$ and the vertical motion is the dominant in the equation.

5.4.2 Analytical solutions

In order to have an idea about the behaviour of the concentration, it can help to find analytical solutions for some simpler problem. Firstly, since the diffusion contribution is quite small, we will look for the solution of the associated advection equation with constant coefficients. Secondly, constant diffusion terms are added and the equation is solved for a particular initial condition.

Advection equation

Since in all of the realistic cases the diffusion coefficient is quite small, the advection terms are going to dominate. In order to have an idea of the behaviour of the concentration, we want to find the analytical solution of the advection equation in an unbounded domain with constant coefficients

$$\frac{\partial c}{\partial t} + u_0 \frac{\partial c}{\partial x} + v_0 \frac{\partial c}{\partial y} = 0, \quad (5.67)$$

with a certain initial condition $c(x, y, 0) = c_0(x, y)$. It is well-known that in the case of constant transport, the method of characteristics is a widely used technique which leads to write the solution in terms of the initial condition, in the form

$$c(x, y, t) = c_0(x - u_0 t, y - v_0 t). \quad (5.68)$$

If we choose the initial condition in order to simulate a point injection at (x_0, y_0) which corresponds to a function of the form $c_0(x, y) = M\delta(y - y_0)\delta(x - x_0)$, where M is constant. The solution is then easily found as

$$c(x, y, t) = M\delta(x - x_0 - u_0 t)\delta(y - y_0 - v_0 t). \quad (5.69)$$

Taking into account that the goal of this analysis is to plot the analytical solution in order to have an initial idea of the original system, we consider the smoother function

$$c_0(x, y) = \exp \left[-\frac{(x - x_0)^2}{r_{0x}} - \frac{(y - y_0)^2}{r_{0y}} \right], \quad (5.70)$$

which gives

$$c(x, y, t) = \exp \left[-\frac{(x - x_0 - u_0 t)^2}{r_{0x}} - \frac{(y - y_0 - v_0 t)^2}{r_{0y}} \right]. \quad (5.71)$$

Constant advection–diffusion equation

Let us consider now the full advection-diffusion equation in an unbounded domain with constant coefficients

$$\frac{\partial c}{\partial t} + u_0 \frac{\partial c}{\partial x} + v_0 \frac{\partial c}{\partial y} = D_x \frac{\partial^2 c}{\partial x^2} + D_y \frac{\partial^2 c}{\partial y^2}. \quad (5.72)$$

where $c(x, y, 0) = c_0(x, y)$ represents a point injection at some (x_0, y_0) , i.e. $c_0(x, y) = M\delta(y - y_0)\delta(x - x_0)$, where M is constant. Let us take $(x_0, y_0) = (0, 0)$ and $M = 1$. Then, as suggested in [123], we will look for a solution of the form

$$c(x, y, t) = g_1(x, t)g_2(y, t). \quad (5.73)$$

Hence, g_1 satisfies

$$\frac{\partial g_1}{\partial t} + u_0 \frac{\partial g_1}{\partial x} = D_x \frac{\partial^2 g_1}{\partial x^2}, \quad (5.74)$$

with $g_1(x, 0) = \delta(x)$. Applying the change of variables $z = x - u_0 t$ we obtain the classical diffusion equation

$$\frac{\partial g_1}{\partial t} = D_x \frac{\partial^2 g_1}{\partial z^2}. \quad (5.75)$$

In the same way explained in Chapter 2, we can proceed with another coordinate transformation via the similarity variables $\eta = At^\alpha z$ and $g_1(z, t) = At^\alpha f(\eta)$. The transformed derivatives become

$$g_{1_t} = (At^\alpha)_t f + f_\eta \eta_t = \alpha At^{\alpha-1} (f + \eta f_\eta), \quad (5.76)$$

$$g_{1_z} = At^\alpha f_\eta \eta_z = A^2 t^{2\alpha} f_\eta, \quad (5.77)$$

$$g_{1_{zz}} = (g_{1_z})_z = A^2 t^{2\alpha} (f_\eta)_\eta \eta_z = A^3 t^{3\alpha} f_{\eta\eta}, \quad (5.78)$$

and putting these expressions into (5.75) we have

$$\alpha At^{\alpha-1} (f + \eta f_\eta) = DA^3 t^{3\alpha} f_{\eta\eta}, \quad (5.79)$$

which when simplified gives

$$\alpha (f + \eta f_\eta) = DA^2 t^{2\alpha+1} f_{\eta\eta}. \quad (5.80)$$

In order to remove the time dependence, we set $\alpha = -1/2$ and $A = 1/\sqrt{2D}$, obtaining

$$f_{\eta\eta} + \eta f_\eta + f = 0. \quad (5.81)$$

It is easy to notice that $\eta f_\eta + f = (\eta f)_\eta$, hence we can rewrite (5.81) as

$$\frac{\partial}{\partial \eta} (f_\eta + \eta f) = 0, \quad (5.82)$$

which implies that $f_\eta + \eta f$ has to be constant. It can be shown that without loss of generality, we can assume $f_\eta + \eta f = 0$, and integrate

$$\int \frac{\partial f}{f} = - \int \eta \partial \eta, \quad (5.83)$$

which finally gives the solution for the function f as

$$\log(f) = -\frac{\eta^2}{2} + C_1 \quad \Rightarrow \quad f = C_2 e^{\frac{\eta^2}{2}}. \quad (5.84)$$

It can be shown that, for mass conservation motivations, $C_2 = 1/(2\sqrt{\pi})$ and recalling the initial change of variables

$$\eta = \frac{z}{\sqrt{2D_xt}}, \quad g_1(z, t) = \frac{f(\eta)}{\sqrt{D_xt}} \quad (5.85)$$

we can write the solution

$$g_1(z, t) = \frac{1}{2\sqrt{2\pi D_xt}} \exp\left(-\frac{z^2}{4D_xt}\right). \quad (5.86)$$

Finally, we can return to the original coordinates, obtaining the solution for the advection diffusion equation (5.74)

$$g_1(x, t) = \frac{1}{2\sqrt{2\pi D_xt}} \exp\left(-\frac{(x - ut)^2}{4D_xt}\right). \quad (5.87)$$

This result is analogous for the function $g_2(y, t)$ and the solution can be generalized through (5.73) for the two dimensional problem as

$$c(x, y, t) = \frac{1}{4\pi t \sqrt{D_x D_y}} \exp\left[-\frac{(x - u_0 t)^2}{4D_x t} - \frac{(y - v_0 t)^2}{4D_y t}\right]. \quad (5.88)$$

Analytical solutions for the bounded problem in two dimensions would be more accurate but also more complicated. For the purpose of this project they are not necessary but they can be found in [30, 70]. The analytical solutions give us an idea about how the concentration of particles will behave in the original problem and, especially, will be useful to understand the behaviour for small times. This information will be used to avoid difficulties for the initial condition in the numerical scheme.

5.5 Numerical approximations

5.5.1 Small time analysis

A well-known difficulty when solving several problems numerically is to adapt the rapidly changes in the variables that a continuum solution can include to the numerical code. In this case, at the beginning of the process, there are no drugs flowing in the vessel, that is $c(x, y, 0) = 0$, but as soon as $t > 0$ we inject a concentration of particles $c(x_0, y_0, t) = c_{\text{in}}$. To overcome this issue, a small time analysis on the related equation with constant coefficients is performed. Let us consider a constant diffusion coefficient \bar{D}_{tot} , where the bar represents the average value of the sum of the Brownian and shear-induced diffusive contributions divided by Pe. Since the interest is to understand the solution for small times and close to the inlet, let $t = \varepsilon \bar{t}$ and $x = \varepsilon^b \bar{x}$, where $\varepsilon \ll 1$ and b is going to be determined.

Introducing these new variables in equation (5.66), we have

$$\frac{1}{\varepsilon} \frac{\partial c}{\partial \bar{t}} + \frac{1}{\varepsilon^b} \bar{u}_F \frac{\partial c}{\partial \bar{x}} + \frac{\delta}{\varepsilon} \bar{v}_p \frac{\partial c}{\partial y} = \frac{\bar{D}_{\text{tot}}}{\varepsilon} \left(\frac{\varepsilon^2}{\varepsilon^{2b}} \frac{\partial^2 c}{\partial \bar{x}^2} + \frac{\partial^2 c}{\partial y^2} \right), \quad (5.89)$$

which can be rewritten as

$$\frac{\partial c}{\partial \bar{t}} + \varepsilon^{1-b} \bar{u}_F \frac{\partial c}{\partial \bar{x}} + \delta \bar{v}_p \frac{\partial c}{\partial y} = \bar{D}_{\text{tot}} \left(\varepsilon^{2-2b} \frac{\partial^2 c}{\partial \bar{x}^2} + \frac{\partial^2 c}{\partial y^2} \right). \quad (5.90)$$

In order to remove the dependence on ε , we impose $b = 1$, i.e. $x = \varepsilon \bar{x}$ is scaled exactly like the time variable. With the new scale, the leading order of equation (5.90) will be

$$\frac{\partial c}{\partial \bar{t}} + \bar{u}_F \frac{\partial c}{\partial \bar{x}} + \delta \bar{v}_p \frac{\partial c}{\partial y} = \bar{D}_{\text{tot}} \left(\frac{\partial^2 c}{\partial \bar{x}^2} + \frac{\partial^2 c}{\partial y^2} \right). \quad (5.91)$$

In an unbounded domain, as explained in Section 5.4.2, the solution of (5.91) is

$$c(\bar{x}, y, \bar{t}) = \frac{1}{4\pi \bar{t} \bar{D}_{\text{tot}}} \exp \left[-\frac{(\bar{x} - \bar{u} \bar{t})^2}{4\bar{D}_{\text{tot}} \bar{t}} - \frac{(y - \delta \bar{v}_p \bar{t})^2}{4\bar{D}_{\text{tot}} \bar{t}} \right], \quad (5.92)$$

and since for small times the particles are far from the vessel walls, we can use this information for the initial value of the system and avoid numerical problems due to the initial jump of the continuum.

5.5.2 Parameter estimation

Several parameters are playing a crucial role in this dynamic. However, in order to show the importance of the viscosity of the blood, the focus of the simulations will be to understand

the behaviour of the particle concentration comparing the Newtonian and non-Newtonian approximations of the flow. In this section, we will justify and estimate the others key parameters, such as the dimensions of the vessel, the strength of the magnetic field and the permeability of the vessel's wall.

As many authors observed (see for example [31, 68, 95]), very different scenarios can arise when looking at different types of vessel. In fact, the technique of magnetic drug targeting is hard to conduct in the main vessels where particles must overcome a strong flow and long distances, and on the other hand the smaller vessels have the complication derived from the possible agglomeration of particles occluding the stream. Moreover, in the case of capillaries, red blood cells are of the same dimension of the width of the vessel itself and their elastic properties should be taken into account in the model. In arteries, even if normally considered large vessels where the effect of RBCs aggregation is reduced, we can observe the non-Newtonian behaviour due to the presence of spots of low shear rates, such as bends and bifurcation junctions, or in the case of pathological conditions. For this reason we choose to focus our study on them.

As highlighted in Section 5.4.1, if the magnetic force is too weak to overcome the strength of the fluid drag, particles will be "washed away" with the blood along the vessel. On the other hand, a too strong magnetic field cannot be applied in order to avoid damage to human body. Hence, a balance that also takes into account the distance from the particles to the wall needs to be found. In addition to the viscosity of the blood, the strength of the magnetic field is a key parameter in the calculation of the velocity of the particles. It is noted that the application of the magnetic field is dictated by international rules, in order to minimise side effect damage. The World Health Organization states that a person moving within a field above 2T can experience adverse effects such as nausea and vertigo but static magnetic fields can cause acute effects only likely within fields in excess of 8T (for example, MRI scanners produces one of about 3T). International guidelines for public exposure to magnetic fields set an upper limit of 40mT which is around 1000 times stronger than the Earth's magnetic field. However, in the case of magnetic fields applied in drug targeting therapies, between 0.1T–1.5T in animal trials and 0.2T–0.8T in human clinical trials were used [28]. Most of the simulations cited in this thesis follow this range and all the approximations explained in Section 5.2.1 lead to similar values for the magnetic force

acting on particles. In both [45, 94] particles with a magnetite volume fraction $\Upsilon = 0.1$, i.e. that the particles contain the 10% magnetite by volume, are considered. They set the mass magnetization $M_{\text{sat}} = 50 \text{ A m}^2 \text{ kg}^{-1}$ and density $\rho = 5 \times 10^3 \text{ kg m}^{-3}$, under a magnetic field gradient $B_G = 10 \text{ T m}^{-1}$. Taking the case of the artery, using equation (5.13), they obtain a magnetic force $F_0 \in [10^{-15}, 10^{-12}] \text{ N}$, depending on the size of the particle, which is in the range of μm . In [82], iron oxide nanoparticles are subjected to a magnetic force of about $1.9 \times 10^{-13} \text{ N}$, whose value is obtained using equation (5.9) where $a = 250 \text{ nm}$, $\mu_0 = 4\pi \times 10^{-7} \text{ N A}^{-2}$, $\chi = 20$ and the magnetic spatial gradient of the order of 10^7 A/m^2 . The experiment is produced by a permanent magnet with $\mathbf{B} = 0.5\text{T}$ which produces a magnetic field intensity $\mathbf{H} = 3.7 \times 10^5 \text{ A/m}$. It is important to notice that while smaller particles have as advantage to avoid agglomeration once magnetic field is removed, we will need a stronger magnetic field gradient in order to compete with the drag force, since magnetic force scales with volume. In Section 5.5, simulations show how particles are affected by a magnetic force of the order $\mathcal{O}(10^{-13}) \text{ N}$. The fact that a stronger magnetic field is needed, with respect to the microscale choices, it is also explained by the size of the particles. In fact, magnetic forces scale with volume, in contrast to the drag force, therefore at the nanoscale a stronger field is needed to provide the same result.

Another key value is the permeability of the vessel. In fact, in the blood circulatory system certain types of vessels have stronger walls, reducing the possibility of particles to get out of the blood stream and into the surrounding tissue. The permeability coefficient κ represents the capacity of the vessel to let the concentration of particles pass through the wall. As theoretically predicted from Richardson *et al.* [94] via the matched asymptotic technique, the parameter κ plays an important role in the determination of the position of the particles deposited onto the vessel wall. In fact, their outer solution shows how small values of the permeability are responsible for the formation of a boundary layer region in the immediate vicinity of the wall where the advective flux balances the diffusive flux and the thickness of the vessel wall prevents particles from flowing out. In this project, a representative value for $\kappa = \mathcal{O}(10^{-4})$ is chosen in order to represent a type of wall where particles are able to pass through but a small boundary layer is observed.

In Table 5.3 all the parameters needed for the advection-diffusion equation are listed.

Quantity	Symbol	Value	Units	References
Blood cell radius	r_{RBC}	4.2×10^{-6}	m	[45]
Coeff. blood cell conc.	K_{sh}	5×10^{-2}	No.	[45]
Inlet concentration	c_{in}	1	mol m ⁻³	[82]
Particle radius	a	15×10^{-9}	m	[45]
Boltzmann constant	k_{B}	1.38×10^{-23}	m ² kg s ⁻² K ⁻¹	[39]
Temperature	T	310.15	K	[39]

Table 5.3: Dimensional parameters for the particles concentration equation.

5.5.3 Finite difference scheme

In order to simulate the behaviour of the concentration of particles, we will define a finite difference scheme for the advection–diffusion equation (5.63), subject to the boundary conditions (5.60)–(5.62) and initial condition $c(x, y, 0) = 0$. Advection terms will dominate in the equation but the diffusive contribution becomes important near the wall of the vessel, where the fluid have near zero velocity. Diffusion terms also help to stabilize the numerical scheme. The finite difference scheme includes the approximation by forward Euler in time, first order upwind for the advection terms and central differences for the second derivatives. The velocity of the fluid u_F , its derivatives and the velocity of the particles v_p are known values at each time step.

Let us consider a grid of length L and width $2R$ composed by $n_x \times n_y$ nodes. The spatial steps will be $\Delta x = L/(n_x - 1)$ and $\Delta y = 2R/(n_y - 1)$, and Δt is chosen in order to satisfy the stability condition of the scheme. We will use the intuitive notation

$$c_{i,j}^n := c(x_i, y_j, t^n), \quad u_{F_j} := u_F(y_j), \quad v_{p_j} := v_p(y_j), \quad D_{T_j} := D_{\text{tot}}(y_j). \quad (5.93)$$

The choice of the direction of the upwind step is made considering that the solution of the velocity of the fluid is always non negative and the direction of the velocity of the particle is always negative (since we have positioned the magnet below the vein). Then, equation

(5.63) can be approximated as

$$\begin{aligned} & \frac{c_{i,j}^{n+1} - c_{i,j}^n}{\Delta t} + u_{F_j} \left(\frac{c_{i,j}^n - c_{i-1,j}^n}{\Delta x} \right) + \left(\frac{v_{p_{j+1}} c_{i,j+1}^n - v_{p_j} c_{i,j}^n}{\Delta y} \right) = \\ & + D_{T_j} \left(\frac{c_{i+1,j}^n - 2c_{i,j}^n + c_{i-1,j}^n}{\Delta x^2} \right) + D_{T_{j+\frac{1}{2}}} \left(\frac{c_{i,j+1}^n - c_{i,j}^n}{\Delta y^2} \right) - D_{T_{j-\frac{1}{2}}} \left(\frac{c_{i,j}^n - c_{i,j-1}^n}{\Delta y^2} \right), \end{aligned} \quad (5.94)$$

where $D_{T_{j \pm \frac{1}{2}}}$ are evaluated by the arithmetic mean. We also need to specify the inflow boundary conditions at $x = 0$ and $y = \pm R$. On the left border, where the concentration of drugs is injected for a limited interval of time, we have that

$$c_{1,j}^n = \begin{cases} c_{\text{in}} & \text{for } 0 \leq t^n \leq T_{\text{inj}}, \\ 0 & \text{otherwise,} \end{cases} \quad (5.95)$$

for $j = 1, \dots, n_y$, since we stop injecting nanoparticles at T_{inj} .

On the wall of the vessel, that is the upper and the lower side of the rectangle, we approximated conditions (5.60), by which particles can pass through the vein with a constant permeability coefficient equal to κ , through the three-point backward difference formula

$$v_{p_{n_y}} c_{i,n_y}^{n+1} - D_{T_{n_y}} \left(\frac{3c_{i,n_y}^{n+1} - 4c_{i,n_y-1}^{n+1} + c_{i,n_y-2}^{n+1}}{2\Delta y} \right) = -\kappa c_{i,n_y}^{n+1} \quad (5.96)$$

and the three-point forward difference formula

$$v_{p_1} c_{i,1}^{n+1} - D_{T_1} \left(\frac{-c_{i,3}^{n+1} + 4c_{i,2}^{n+1} - 3c_{i,1}^{n+1}}{2\Delta y} \right) = \kappa c_{i,1}^{n+1} \quad (5.97)$$

for $i = 1, \dots, n_x$.

The right border is approximated again through the three-point forward difference formula

$$u_{F_j} c_{n_x,j}^{n+1} - D_{T_j} \left(\frac{-c_{n_x-2,j}^{n+1} + 4c_{n_x-1,j}^{n+1} - 3c_{n_x,j}^{n+1}}{2\Delta x} \right) = 0 \quad (5.98)$$

for $j = 1, \dots, n_y$.

5.5.4 Results

In this section we present the results obtained by comparing the effects that the different choices of the fluid models have on the motion of the particles in the bloodstream.

The geometry chosen represents a simplification of a small artery having width and length like in Table 5.1. The velocity of the blood and the relative viscosity will be

approximated by the solutions (5.40) and (5.51) and by the numerical approximation of the solution of (5.49) for the Newtonian, the Ellis and the Carreau models, respectively. The power-law model is not presented, since it has been shown that its viscosity approximation does not fit the blood behaviour. The velocity of the particles v_p will be calculated via equation (5.58) considering a constant magnetic force F_0 and a viscosity $\eta(\dot{\gamma})$ given by the constant value μ in the case of a Newtonian fluid, or calculated via (5.19) and (5.18) for the Ellis and the Carreau models. A five seconds long initial injection at $x = 0$ is applied (that is $T_{\text{inj}} = 5\text{s}$). The plots for the particles concentration are obtained implementing the numerical scheme detailed in Section 5.5.3 in MATLAB where the parameters listed in Tables 5.2 and 5.3 are used. The aim of all the simulations is to understand how the approximation can vary according to the model chosen for the blood. Moreover, special attention will be paid to the strength of the magnetic force needed in order to target particles to the disease area.

Figure 5.5 shows the behaviour of the concentration of nanoparticles in the vessel where the Newtonian approximation for blood is considered. The first plot represents the velocity field, which is given by the contribution of the drag of the fluid and the magnetic force acting on the system. Since the velocity of the particles depends on the viscosity of the fluid and the Newtonian approximation implies a constant value for $\eta(\dot{\gamma})$, the changes in the velocity field are only due to the parabolic profile of u_F and, therefore, only in the x -direction. The other images show the snapshots of the concentration of particles at six fixed times under the influence of a constant magnetic force $F_0 = 1 \times 10^{-13}$ N. We can observe how all the particles entering the bloodstream from the left border are driven to the lower wall of the vessel and captured into the tissue halfway through the channel in about 30s.

In Figures 5.6 and 5.7 the equivalent plots to those of Figure 5.5 are shown but now using the Carreau and the Ellis models, respectively, instead of the Newtonian one. Both models give a very similar approximation for the behaviour of the concentration of particles, which is a direct consequence of what was demonstrated in Section 5.3.2. However, we can clearly see that the same magnetic force used in the previous simulation is now unable to drive the particles towards the same region. In fact, even if a slight movement in the y -direction can be observed and the particles very near to the vessel's wall are able to get into the tissue, most of the particles are "washed away" by the drag force. This change can be observed

in the first image of both figures, where the velocity field highlights the differences with the previous case. This clearly shows that using a Newtonian fluid model can result in the wrong conclusion that a magnetic force of that strength is able to target a specific region.

As shown in Figures 5.8 and 5.9, we will need a magnetic force eight times greater than in the Newtonian case in order to be able to attract particles to the lower wall of the vessel when considering the Carreau and the Ellis model, respectively. Looking at the first image of both figures, the velocity field shows clearly how the different profiles for the viscosity strongly changes the behaviour of the concentration. Furthermore, we can observe how the particles near the vessel wall experience a much smaller drag force with respect to those at the center of the vessel and, therefore, will react strongly to the magnetic force and deviate from the typical parabolic behaviour of the fluid. Moreover, the diffusive contribution plays an important role in this region and influence the motion of the particles at this scale. In the six snapshots of the concentration for six different times we can observe how particles driven by the balance of all the forces acting on this system are attracted by the external magnetic field to the wall of the vessel and pass through it in about 40s. In these plots, especially at $t = 6s$ and $t = 15s$, we can also observe a thin boundary layer where particles accumulate in the immediate proximity to the wall, as theoretically predicted in [94].

All the simulations confirm the importance of choosing the appropriate fluid model, specifically one where the viscosity follows the shear-thinning behaviour of the blood in order to correctly predict whether a specific magnetic field is able to attract particles to the desired area and in which amount of time. Moreover, even if Brownian diffusion seems negligible for the majority of the domain, it is important near the wall of the vessel and can even be the predominant diffusive contribution for small particles.

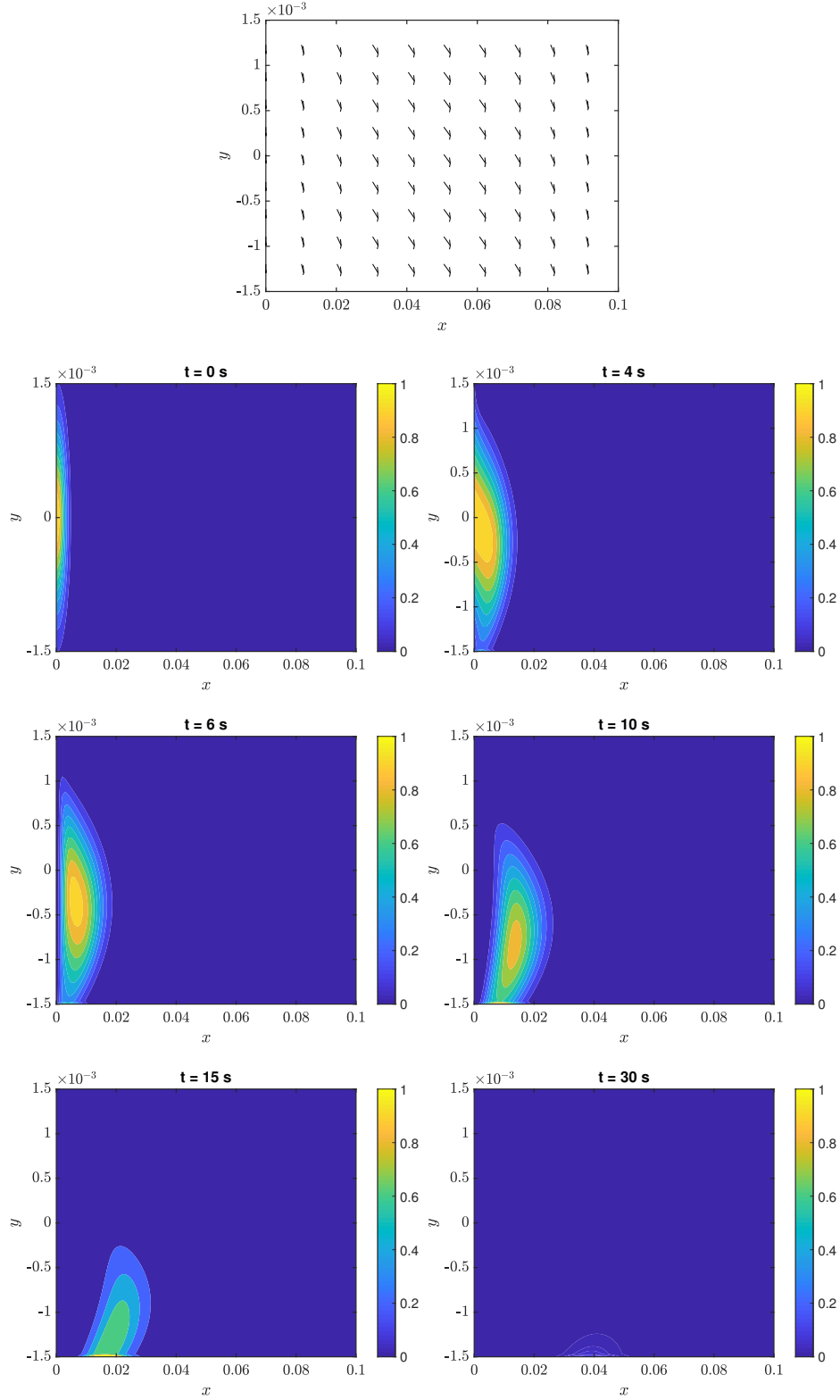


Figure 5.5: Snapshots of the concentration of particles in an artery at six different times ($t = 0\text{ s}$, $t = 4\text{ s}$, $t = 6\text{ s}$, $t = 10\text{ s}$, $t = 15\text{ s}$, $t = 30\text{ s}$), choosing the Newtonian model for the blood flow and with a constant magnetic force equal to $F_0 = 1 \times 10^{-13}\text{ N}$. The first image represents the velocity field.

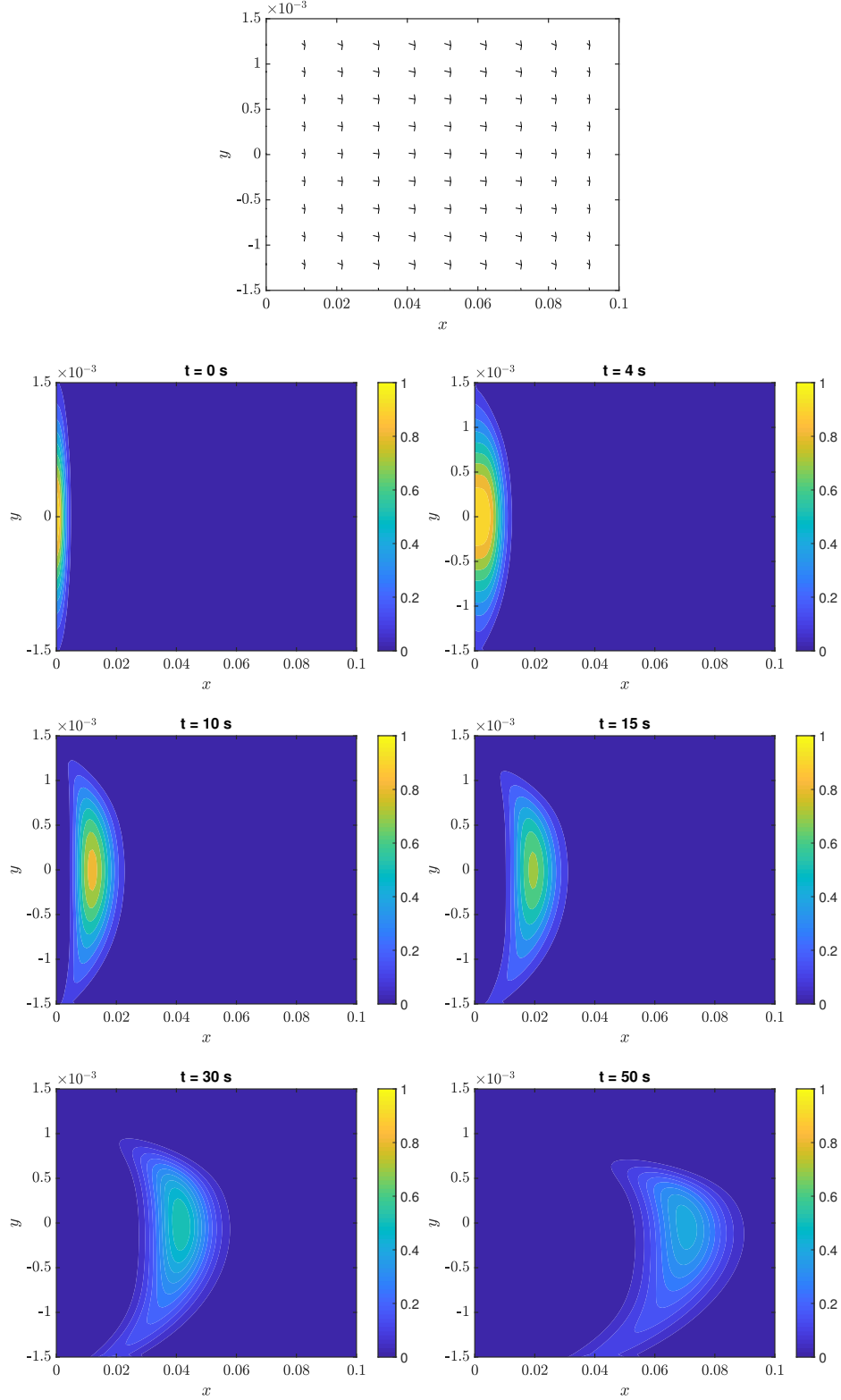


Figure 5.6: Motion of magnetic nanoparticles in an artery at six different times ($t = 0\text{s}$, $t = 4\text{s}$, $t = 6\text{s}$, $t = 10\text{s}$, $t = 15\text{s}$, $t = 30\text{s}$ and $t = 40\text{s}$), choosing the Carreau model for the blood flow and with a constant magnetic force acting on particles equal to $F_0 = 8 \times 10^{-13}$ N. The first image represents the velocity field.

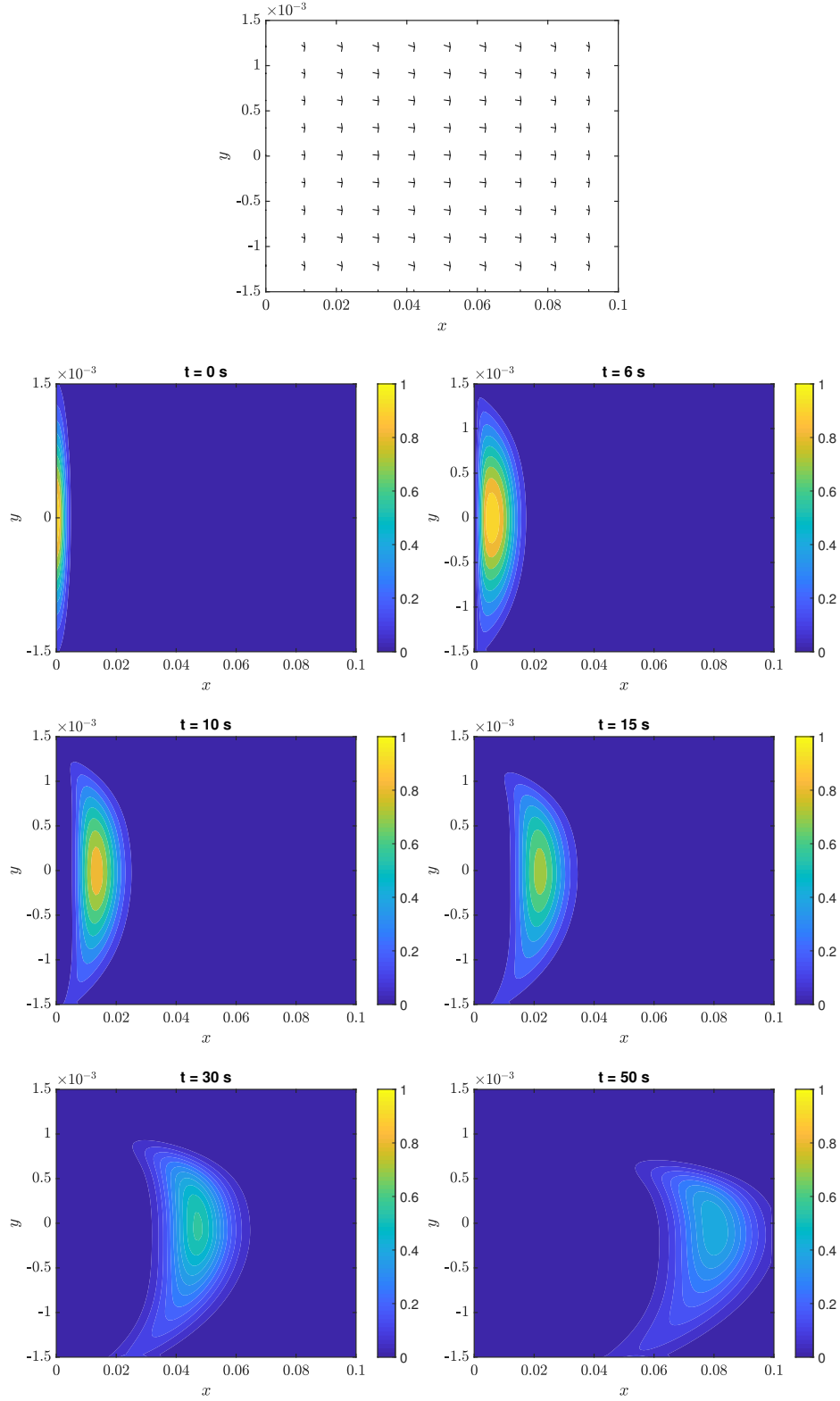


Figure 5.7: Snapshots of the concentration of particles in an artery at six different times ($t = 0\text{ s}$, $t = 4\text{ s}$, $t = 6\text{ s}$, $t = 10\text{ s}$, $t = 15\text{ s}$, $t = 30\text{ s}$), choosing the Ellis model for the blood flow and with a constant magnetic force equal to $F_0 = 1 \times 10^{-13}\text{ N}$. The first image represents the velocity field.

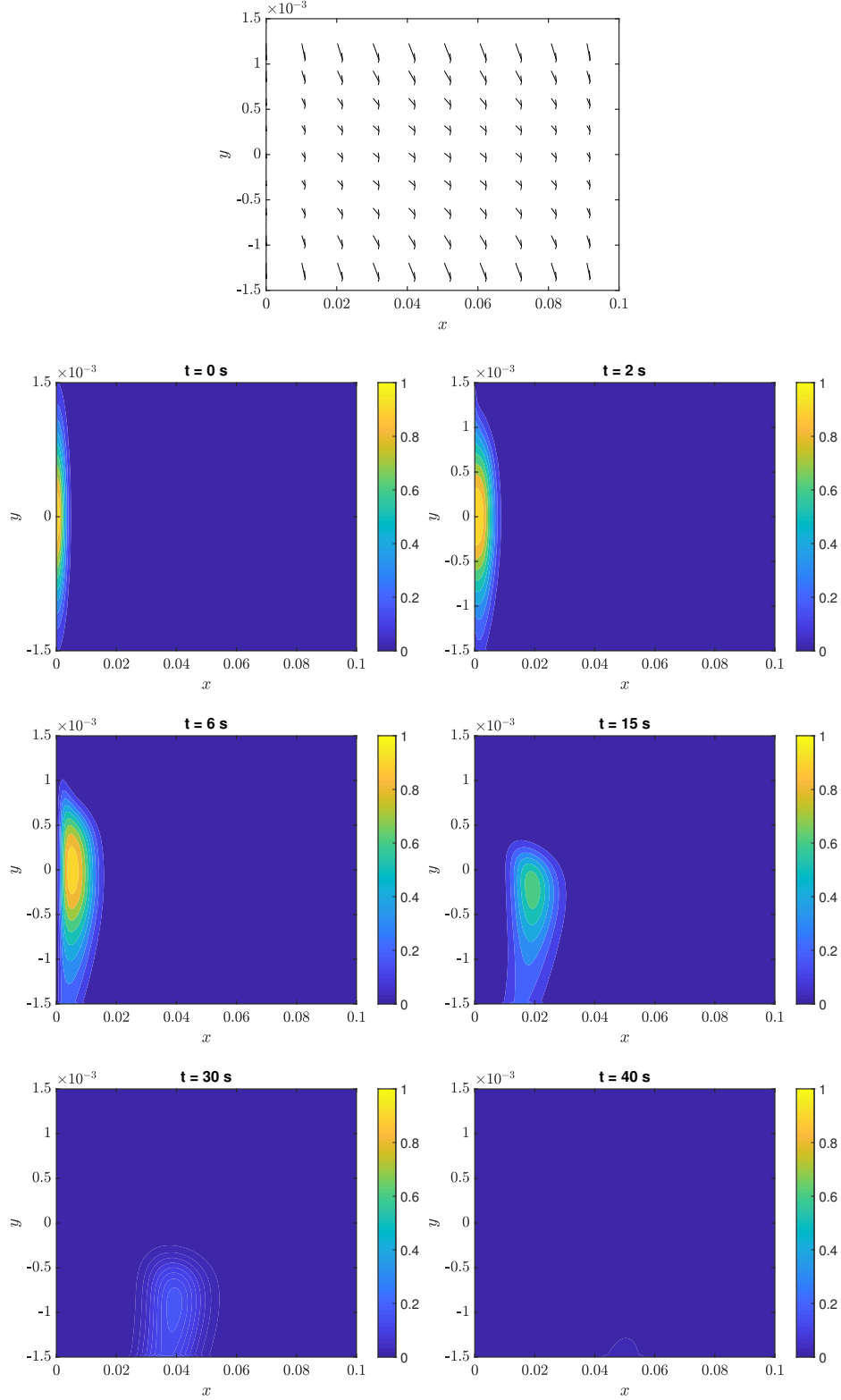


Figure 5.8: Motion of magnetic nanoparticles in an artery at six different times ($t = 0\text{ s}$, $t = 4\text{ s}$, $t = 6\text{ s}$, $t = 15\text{ s}$, $t = 30\text{ s}$ and $t = 40\text{ s}$), choosing the Carreau model for the blood flow and with a constant magnetic force acting on particles equal to $F_0 = 8 \times 10^{-13}\text{ N}$. The first image represents the velocity field.

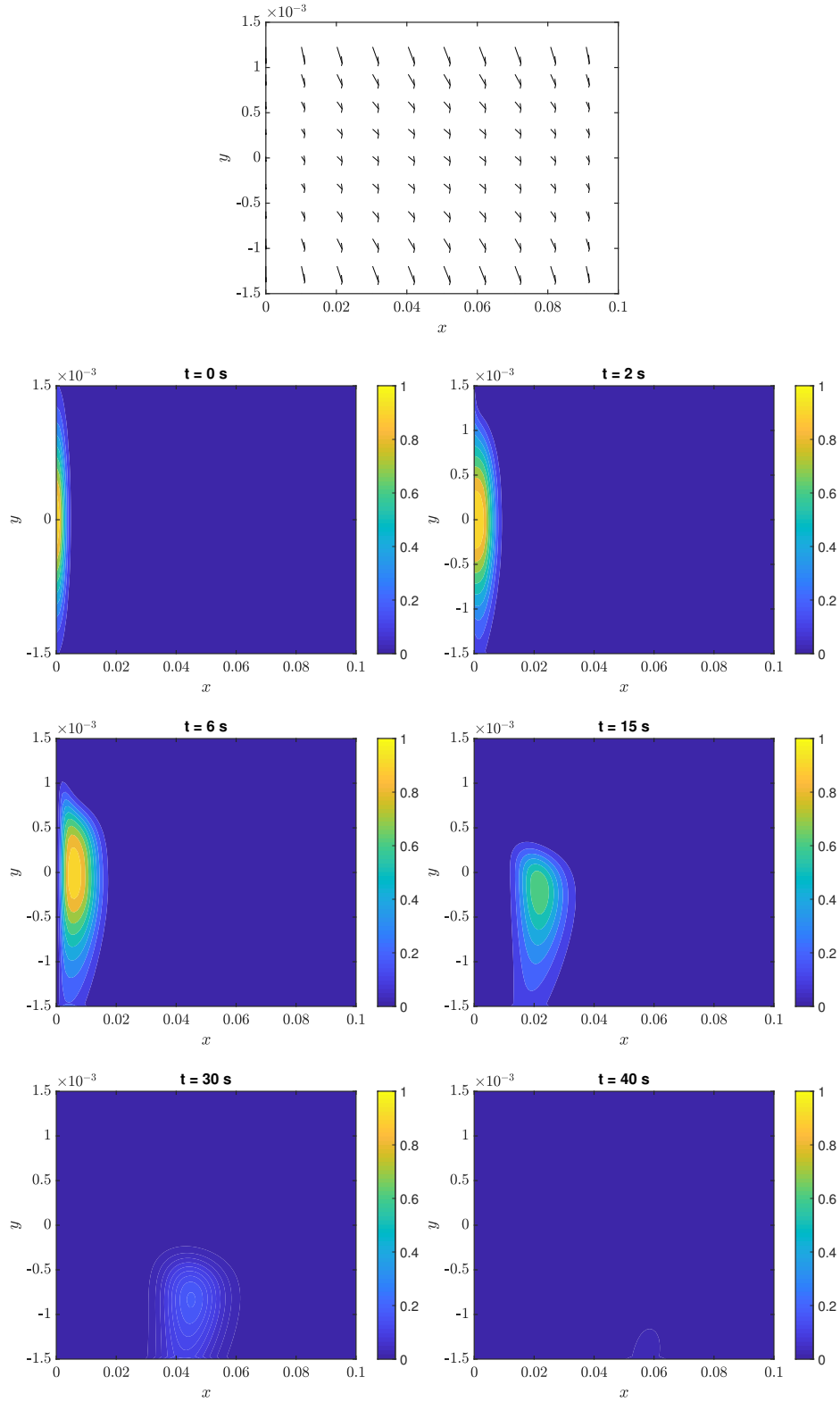


Figure 5.9: Motion of magnetic nanoparticles in an artery at six different times ($t = 0\text{ s}$, $t = 4\text{ s}$, $t = 6\text{ s}$, $t = 15\text{ s}$, $t = 30\text{ s}$ and $t = 40\text{ s}$), choosing the Ellis model for the blood flow and with a constant magnetic force acting on particles equal to $F_0 = 8 \times 10^{-13}\text{ N}$. The first image represents the velocity field.

5.6 Conclusion

We have formulated a model for the motion of magnetic nanoparticles in a vessel subject to an external magnetic field in order to optimize the technique of magnetic drug targeting. The model consists of a system of nonlinear partial differential equations formed by the Navier-Stokes equations for the flow of blood coupled with an advection-diffusion equation for the concentration of nanoparticles. Choosing a 2D vessel, the equations are simplified and the system is solved via analytical and numerical techniques.

The aim of this project has been to account for all the forces acting in the physical process, combined with realistic choices for parameters. It has been shown that, in order to correctly simulate the delicate balance between hydrodynamic and magnetic forces in the vessel, it is crucial to choose an accurate model for blood behaviour. Moreover, the correct size for superparamagnetic nanoparticles is used, that is $\approx 30\text{nm}$ in diameter, which affects the strength of the magnetic field needed and the effects given by the diffusion contribution.

The first part of this chapter describes the non-Newtonian behaviour of blood and the importance of choosing the right model for the viscosity and the velocity of the fluid. Newtonian approximations are inaccurate and the more commonly used power-law model also has a critical unbounded value for the viscosity at the center of the vessel. The Carreau and the Ellis model are found to be the best approach to simulate blood behaviour. While the first one is able to capture the shear-thinning behaviour of the fluid in both Newtonian plateaux and in the transition region between them, the second one allows to find an analytical solution for particular choices of the geometry.

Secondly, the solutions for the flow are used to model the motion of the particles. In order to reduce agglomeration and toxicity levels, superparamagnetic nanoparticles are found to be good candidates, since they reduce their magnetism as soon as the magnetic field is turned off. It is also shown that, since magnetic forces scale with volume, a stronger magnetic field is needed with respect to the microscale to overcome the drag force of the blood. Moreover, at the nanoscale the Brownian motion and the shear-induced diffusion can be important in the proximity of the vessel's wall. The main result demonstrated that the approximations made by the different models for the blood flow strongly affect the simulation for the concentration. In fact, under the influence of the same external

magnetic field, while the Newtonian model predicted the movement of the particle from the bloodstream into the tissue, both the Carreau and the Ellis model showed that the strength of the magnetic force generated was not able to attract particles to the wall of the vessel.

In future work this theoretical model can be improved including for example pulsatile flow, the elasticity of the vessels due to the change in pressure and more realistic geometries. Furthermore, it can be combined with detailed experimental studies to optimize the deliver of drugs to specific regions or other applications.

6 | Conclusions

The goal of this thesis was to analyse two innovative processes in the developing field of nanotechnology. In the first part, the growth of nanoparticles by precipitation has been deeply studied, identifying the main features of the process in order to avoid Ostwald ripening and optimise the growth. In the second part of the thesis, we focused on a practical applications in nanomedicine namely magnetic drug targeting and how the non-Newtonian characteristics of the blood are found to be key to correctly modelling this medical technique.

Like many industrial applications, the growth of nanoparticles in solution can be modelled by means of a so-called moving boundary value problem, where the evolution of the radius of the particles depends on time and has to be found as a part of the solution. In particular, at the nanoscale the variation in solubility in the current problem varies in a similar manner to the behaviour of the melt temperature in the classical applications of this kind of problems. In the first part of the thesis the idea was to identify the key features of the growth of a single particle and then extend these results to solve the full problem.

In Chapter 3 we analysed the growth of a single, spherical crystal in solution. The main aim was to correctly interpret the governing equations of the process in order to optimise the growth. We found that the standard model was applied incorrectly over the years, for more than one reason. First of all, the particle growth occurs in two distinct stages and the standard model holds only during the second one. The common procedure to fit experimental data from the very beginning of the synthesis leads to incorrect values for the parameters of the system. Secondly, we found via mathematical tools that the model is not able to distinguish between diffusion and surface kinetics driven growth, within the assumptions of the pseudo-steady state. This has also been possible thanks to the

identification of an approximate explicit solution for the particle radius, a new easy tool not previously presented in literature. This solution only depends on two independent parameters strongly reducing the errors in the fitting process. The importance of the particle solubility is also demonstrated. The Gibbs-Thompson equation gives the variation of the particle solubility with the radius r_p and this contribution is generally neglected based on the assumption that the capillary length $\alpha \ll r_p$. However, since α is of the order nanometres, at early times it is bigger than the particle radius, and therefore plays a controlling role in particle growth at that stage. This effect has not been spotted before in the growth of a single particle due to the fact that the model is not valid at early times but it gives an important contribution when considering the growth of a group of particles.

The important role of the solubility in a system of particles has been widely demonstrated in Chapter 4. It was found crucial in order to control the phenomenon known as Ostwald ripening, where larger particles grow at the expense of smaller ones, and to optimise the growth process. A model for the growth of N particles was developed and dominant terms of the system were identified. The basis of this model is found in the pseudo-steady approximation, already used in the model for the growth of a single particle and based on the fact that the concentration adjusts much faster than growth occurs. However, the problem is still time-dependent due to the definition of the particle radius and the bulk concentration. The Ostwald-Freundlich condition shows how the particle solubility s increases as size decreases and, when this value crosses the curve of the bulk concentration c_b , Ostwald ripening is observed. In fact, when $s < c_b$ then monomer molecules diffuse from the bulk towards the particle to react with the surface and the particle grows, whereas if $s > c_b$ the particle shrinks. Simulations with $N = 2$, which may represent an initially bimodal distribution, clearly showed the role played by the changes in solubility. As the process starts both values for the solubility are below the bulk concentration and decrease as each r_p increases, but when the solubility of the smaller particle crosses the c_b curve, its size decreases and Ostwald ripening occurs. This extended model is able to predict in which range of parameters this undesired phenomenon can be avoided. Moreover, making N arbitrarily large, the prediction of the particles size distribution showed excellent agreement with experimental data and with the analytical solution for the mean radius of the group of particles.

As extensively highlighted in the first part of this thesis, the ability to control the particles growth is crucial in a wide variety of industrial applications. Considering the particular application in cancer therapy, nanotechnology-based approaches strongly rely on precise sizes of the particles, depending on the technique developed and the unique biological characteristics of each patient. The main aim of the second part of the thesis was to show the great potential of the nanoscale contribution in cancer treatments and the importance of a mathematical approximation when modelling such a delicate biological situation.

In Chapter 5 a mathematical model for the movement of drug nanocarriers in human vessels under the influence of an external magnetic field was analysed. The main results involved the solution of Navier-Stokes equations for the blood flow by means of geometry simplifications and the approximation of the advection-diffusion equation for the concentration of particles in the bloodstream via numerical techniques. The comparison between four different models for the behaviour of the blood showed the importance of including the variation of the viscosity, since the velocity of the particles in the vessel strongly depends on it. Among the non-Newtonian models for the blood flow, the power law approximation, the Carreau and the Ellis models have been used and discussed. While the first one showed a criticality at the center of the vessel where the viscosity goes to infinity as $\dot{\gamma} \rightarrow 0$, the other two models were found to be both good approximations. In particular, the Carreau model was found to be very accurate to predict the shear-thinning behaviour of the blood, while the Ellis model is unable to capture the second Newtonian plateaux, typical of this kind of fluids. However, since very high value of the shear rates are not reached in our situation, their approximation are quite similar and the Ellis model is preferred due to the possibility to write down an analytical solution for the flow in our simplified geometry. Finally, the behaviour of the concentration of drugs bound to magnetic nanoparticles was studied comparing the results obtained for the fluid. Particular attention has been paid to correctly identify all the acting forces on the system at this scale, which include the diffusive contributions given by both Brownian motion and the scattering diffusion induced by the collisions of red blood cells, and the delicate balance between the drag and the magnetic force needed in order to successfully attract particles to the disease area. The identification of the dominant force strongly depends on the position of the particles in the vessel. In the center of the stream the drag of the blood

generally prevails over the magnetic forces but, as soon as we approach the wall of the vessel, the external magnetic field is able to compete with the fluid flow, attracting the particles to the desired region. Ideally, once they have reached the wall, particles extravasate from the blood vessel to the tissue through the leaky vasculature and release the therapeutic agent. However, we found that, if the approximation of the flow of blood does not take into account its shear-thinning behaviour, the model can lead to wrong conclusion regarding whether the particles are able to reach the disease region or not.

In summary, we have presented two mathematical models to study the features and the applications of nanotechnology in real-life problems. The main goal was to show how mathematical-based approaches are required to fully understand and optimise physical, chemical and biological processes, allowing to make several steps forward even in the fight against cancer.

Bibliography

- [1] F. Ahmad, A.K. Pandey, A. B. Herzog, J.B. Rose, C.P. Gerba, and S.A. Hashsham. Environmental applications and potential health implications of quantum dots. *J. Nanoparticle Res*, 14:1038, 2012.
- [2] C. Alexiou, R. Jurgons, R. Schmid, A. Hilpert, C. Bergemann, F. Parak, and H. Iro. In vitro and in vivo investigations of targeted chemotherapy with magnetic nanoparticles. *Journal of Magnetism and Magnetic Materials*, 293:389–393, 05 2005.
- [3] H. Alimohamadi and M. Imani. Transient non-Newtonian blood flow under magnetic targeting drug delivery in an aneurysm blood vessel with porous walls. *International Journal for Computational Methods in Engineering Science and Mechanics*, 15(6):522–533, 2014.
- [4] A.J. Ardell. The effect of volume fraction on particle coarsening: theoretical considerations. *Acta Metallurgica*, 20(1):61–71, 1972.
- [5] Z. Ashikbayeva, D. Tosi, D. Balmassov, E. Schena, P. Saccomandi, and V. Inglezakis. Application of nanoparticles and nanomaterials in thermal ablation therapy of cancer. *Nanomaterials*, 9:1195, 08 2019.
- [6] B. Bahrami, M. Hojjat-Farsangi, H. Mohammadi, E. Anvari, G. Ghalamfarsa, M. Yousefi, and F. Jadidi-Niaragh. Nanoparticles and targeted drug delivery in cancer therapy. *Immunology letters*, 190:64–83, 2017.
- [7] A. Baldan. Review progress in Ostwald ripening theories and their applications to nickel-base superalloys Part I: Ostwald ripening theories. *Journal of Materials Science*, 37(11):2171–2202, 2002.

-
- [8] P.D. Ballyk, D.A. Steinman, and C. Ethier. Simulation of non-Newtonian blood flow in an end-to-side anastomosis. *Biorheology*, 31:565–86, 09 1994.
- [9] N.G. Bastús, F. Merkoçi, J. Piella, and V. Puentes. Synthesis of highly monodisperse citrate-stabilized silver nanoparticles of up to 200 nm: kinetic control and catalytic properties. *Chemistry of Materials*, 26(9):2836–2846, 2014.
- [10] N.G. Bastús, J. Comenge, and V. Puentes. Kinetically controlled seeded growth synthesis of citrate-stabilized gold nanoparticles of up to 200 nm: size focusing versus Ostwald ripening. *Langmuir*, 27(17):11098–11105, 2011.
- [11] A.T. Bell. The impact of nanoscience on heterogeneous catalysis. *Science*, 299:1688–1691, 2003.
- [12] C. M. Bender and S. A. Orszag. *Advanced mathematical methods for scientists and engineers I: Asymptotic Methods and Perturbation Theory*. McGraw-Hill, 1978.
- [13] A. Boghi, F. Russo, and F. Gori. Numerical simulation of magnetic nano drug targeting in a patient-specific coeliac trunk. *Journal of Magnetism and Magnetic Materials*, 437:86 – 97, 2017.
- [14] A.D. Brailsford and P. Wynblatt. The dependence of Ostwald ripening kinetics on particle volume fraction. *Acta Metallurgica*, 27(3):489–497, 1979.
- [15] E. M. Brauser, T. D. Hull, J. D. McLennan, J. T. Siy, and M. H. Bartl. Experimental evaluation of kinetic and thermodynamic reaction parameters of colloidal nanocrystals. *Chemistry of Materials*, 28(11):3831–3838, 2016.
- [16] D.E. Brooks, J.W. Goodwin, and G.V. Seaman. Interactions among erythrocytes under shear. *Journal of Applied Physiology*, 28(2):172–177, 1970.
- [17] C. R. Bullen and P. Mulvaney. Nucleation and growth kinetics of CdSe nanocrystals in octadecene. *Nano Letters*, 4(12):2303–2307, 2004.
- [18] J. Caldwell and Y.Y. Kwan. On the perturbation method for the Stefan problem with time-dependent boundary conditions. *International Journal of Heat and Mass Transfer*, 46:1497–1501, 2003.

-
- [19] E. Carboni, K. Tschudi, J. Nam, X. Lu, and A. Ma. Particle margination and its implications on intravenous anticancer drug delivery. *AAPS PharmSciTech*, 15, 04 2014.
- [20] E. K. Cherry and J. Eaton. A comprehensive model of magnetic particle motion during magnetic drug targeting. *International Journal of Multiphase Flow*, 59:173–185, 02 2014.
- [21] S. Chien. Shear dependence of effective cell volume as a determinant of blood viscosity. *Science (New York, N.Y.)*, 168:977–9, 06 1970.
- [22] Y. Cho and K. Kensey. Effects of the non-Newtonian viscosity of blood on flows in a diseased arterial vessel. part 1: Steady flows. *Biorheology*, 28:241–62, 02 1991.
- [23] X. Chuang, H. Hongxun, C. Wei, and W. Jingkan. Crystallization kinetics of CdSe nanocrystals synthesized via the top–topo–hda route. *Journal of Crystal Growth*, 310(15):3504 – 3507, 2008.
- [24] M.D. Clark, S.K. Kumar, J.S. Owen, and E.M. Chan. Focusing nanocrystal size distributions via production control. *Nano Letters*, 11(5):1976–1980, 2011.
- [25] J. Crank. *Free and moving boundary problems*. Oxford University Press, 1984.
- [26] M.C. Daniel and D. Astruc. Gold nanoparticles: assembly, supramolecular chemistry, quantum-size-related properties, and applications toward biology, catalysis, and nanotechnology. *Chemical Reviews*, 104(1):293–346, 2004.
- [27] P. Decuzzi, S. Lee, B. Bhushan, and M. Ferrari. A theoretical model for the margination of particles within blood vessels. *Annals of biomedical engineering*, 33:179–90, 03 2005.
- [28] J. Dobson. Magnetic nanoparticle for drug delivery. *Drug Dev. Res.*, 67:1–2, 01 2006.
- [29] C. Fanelli, V. Cregan, F. Font, and T. G. Myers. Modelling nanocrystal growth via the precipitation method. *To appear in International Journal of Heat and Mass Transfer*, arXiv:1901.08990, 2019.

- [30] A. Fedi, M. Massabó, O. Paladino, and R. Cianci. A new analytical solution for the 2D advection-dispersion equation in semi-infinite and laterally bounded domain. *Applied Mathematical Sciences (Ruse)*, 4, 01 2010.
- [31] M. Ferrari. Cancer nanotechnology: Opportunities and challenges. *Nature reviews. Cancer*, 5:161–71, 04 2005.
- [32] S. Fiocchi, E. Chiaramello, M. Bonato, G. Tognola, D. Catalucci, M. Parazzini, and P. Ravazzani. Computational simulation of electromagnetic fields on human targets for magnetic targeting applications. In *2019 41st Annual International Conference of the IEEE Engineering in Medicine and Biology Society (EMBC)*, pages 5674–5677, 2019.
- [33] F. Font. A one-phase Stefan problem with size-dependent thermal conductivity. *Applied Mathematical Modelling*, 63:172–178, 2018.
- [34] F. Font, S. Afkhami, and L. Kondic. Substrate melting during laser heating of nanoscale metal films. *International Journal of Heat and Mass Transfer*, 113:237 – 245, 10 2017.
- [35] F. Font, S.L. Mitchell, and T.G. Myers. One-dimensional solidification of supercooled melts. *International Journal of Heat and Mass Transfer*, 62:411–421, 2013.
- [36] F. Font and T.G. Myers. Spherically symmetric nanoparticle melting with a variable phase change temperature. *Journal of Nanoparticle Research*, 15(12):1–13, 2013.
- [37] F. Font, T.G. Myers, and S.L. Mitchell. A mathematical model for nanoparticle melting with density change. *Microfluidics and Nanofluidics*, 18:233–243, 2015.
- [38] L. Formaggia, A. Quarteroni, and A. Veneziani. *Cardiovascular Mathematics: Modeling and Simulation of the Circulatory System*, volume 1. Springer-Verlag (Milano), 01 2009.
- [39] R. Fournier. *Basic Transport Phenomena in Biomedical Engineering*, 4th edition. CRC Press, 11 2017.

- [40] M. Gaumet, A. Vargas, R. Gurny, and F. Delie. Nanoparticles for drug delivery: The need for precision in reporting particle size parameters. *European Journal of Pharmaceutics and Biopharmaceutics*, 69(1):1 – 9, 2008.
- [41] P. Ghosh, G. Han, M. De, C.K. Kim, and V.M. Rotello. Gold nanoparticles in delivery applications. *Advanced Drug Delivery Reviews*, 60(11):1307–1315, 2008.
- [42] D.A. Giljohann, D.S. Seferos, W.L. Daniel, M.D. Massich, P.C. Patel, and C.A. Mirkin. Gold nanoparticles for biology and medicine. *Angewandte Chemie International Edition*, 49(19):3280–3294, 2010.
- [43] T. R. Goodman. Application of integral methods to transient nonlinear heat transfer. volume 1 of *Advances in Heat Transfer*, pages 51–122. Elsevier, 1964.
- [44] T.R. Goodman. The heat-balance integral and its application to problems involving a change of phase. *Trans. ASME*, 80(2):335–342, 1958.
- [45] A.D. Grief and G. Richardson. Mathematical modelling of magnetically targeted drug delivery. *Journal of Magnetism and Magnetic Materials*, 293(1):455–463, 2005.
- [46] K. Grieve, P. Mulvaney, and F. Grieser. Synthesis and electronic properties of semiconductor nanoparticles/quantum dots. *Current Opinion in Colloid & Interface Science*, 5:168–172, 2000.
- [47] S. C. Gupta. *The classical Stefan problem. Basic concepts, modelling and analysis*, volume 45. Elsevier, 2003.
- [48] J. M. Hill. *One-dimensional Stefan problems: an introduction*, volume 31. Longman Scientific & Technical, 1987.
- [49] M.H. Holmes. *Introduction to perturbation methods*, volume 30. Springer, 2013.
- [50] C.R. Huang and W Fabisiak. Thixotropic parameters of whole human blood. *Thrombosis research*, 8:1–8, 06 1976.
- [51] M. Iggland and M. Mazzotti. Population balance modeling with size-dependent solubility: Ostwald ripening. *Crystal Growth & Design*, 12(3):1489–1500, 2012.

- [52] B.M. Johnston, P.R. Johnston, S. Corney, and D. Kilpatrick. Non-Newtonian blood flow in human right coronary arteries: steady state simulations. *Journal of Biomechanics*, 37(5):709 – 720, 2004.
- [53] E. Kaliviotis, J. Sherwood, and S. Balabani. Local viscosity distribution in bifurcating microfluidic blood flows. *Physics of Fluids*, 30:030706, 03 2018.
- [54] G. Karanikolos, P. Alexandridis, G. Itskos, A. Petrou, and T.J. Mountziaris. Synthesis and size control of luminescent znse nanocrystals by a microemulsion-gas contacting technique. *Langmuir*, 20(3):550–553, 2004.
- [55] J. Kevorkian and J. D. Cole. *Perturbation methods in applied mathematics*. Springer, 1981.
- [56] J. Kudr, Y. Haddad, L. Richtera, Z. Heger, M. Cernak, V. Adam, and O. Zitka. Magnetic nanoparticles: From design and synthesis to real world applications. *Nanomaterials*, 7:243, 08 2017.
- [57] S. Kutluay, A.R. Bahadir, and A. Özdeş. The numerical solution of one-phase classical Stefan problem. *Journal of Computational and Applied Mathematics*, 81(1):135–144, 1997.
- [58] V.K. La Mer. Nucleation in phase transitions. *Industrial and Engineering Chemistry*, 44(6):1270–1277, 1952.
- [59] V.K. La Mer and R. Dinegar. Theory, production and mechanism of formation of monodispersed hydrosols. *Journal of the American Chemical Society*, 72(11):4847–4854, 1950.
- [60] D. Langford. The heat balance integral method. *International Journal of Heat and Mass Transfer*, 16(12):2424–2428, 1973.
- [61] A.J. Lemke, M.I. Pilsach, A. Lübke, C. Bergemann, H. Rieß, and R. Felix. MRI after magnetic drug targeting in patients with advanced solid malignant tumors. *European radiology*, 14:1949–55, 12 2004.

-
- [62] I.M. Lifshitz and V.V. Slyozov. The kinetics of precipitation from supersaturated solid solutions. *Journal of Physics and Chemistry of Solids*, 19(1):35–50, 1961.
- [63] Y. Liu, K. Kathan, W. Saad, and R.K. Prud’homme. Ostwald ripening of β -carotene nanoparticles. *Physical Review Letters*, 98(3):036102, 2007.
- [64] Z. Liu, J.R. Clausen, R.R. Rao, and C.K. Aidun. Nanoparticle diffusion in sheared cellular blood flow. *Journal of Fluid Mechanics*, 871:636–667, 2019.
- [65] Z. Liu, Y. Zhu, R.R. Rao, J.R. Clausen, and C.K. Aidun. Nanoparticle transport in cellular blood flow. *Computers and Fluids*, 172:609 – 620, 2018.
- [66] A. Lübke, C. Bergemann, H. Rieß, F. Schriever, P. Reichardt, K. Possinger, M. Matthias, B. Dörken, F. Herrmann, R. Gürtler, P. Hohenberger, N. Haas, R. Sohr, B. Sander, J. Lemke, D. Ohlendorf, W. Huhnt, and D. Huhn. Clinical experiences with magnetic drug targeting: A phase I study with 4’-epidoxorubicin in 14 patients with advanced solid tumors. *Cancer research*, 56:4686–93, 11 1996.
- [67] F.P. Ludwig, J. Schmelzer, and J. Bartels. Influence of stochastic effects on Ostwald ripening. *Journal of Materials Science*, 29(18):4852–4855, 1994.
- [68] T. Lunoo and T. Puangmali. Capture efficiency of biocompatible magnetic nanoparticles in arterial flow: A computer simulation for magnetic drug targeting. *Nanoscale Research Letters*, 10:426, 10 2015.
- [69] N.V. Mantzaris. Liquid-phase synthesis of nanoparticles: particle size distribution dynamics and control. *Chemical Engineering Science*, 60(17):4749–4770, 2005.
- [70] M. Massabó, R. Cianci, and O. Paladino. An analytical solution of the advection dispersion equation in a bounded domain and its application to laboratory experiments. *J. Applied Mathematics*, 2011, 01 2011.
- [71] P.F. Méndez, S. Sepulveda, J. Manríquez, F.J. Rodríguez, E. Bustos, A. Rodríguez, and Luis A. Godínez. Growth dynamics of polyamidoamine dendrimer encapsulated CdS nanoparticles. *Journal of Crystal Growth*, 361:108 – 113, 2012.

- [72] S.L. Mitchell. Applying the combined integral method to one-dimensional ablation. *Applied Mathematical Modelling*, 36(1):127–138, 2012.
- [73] S.L. Mitchell and T.G. Myers. Improving the accuracy of heat balance integral methods applied to thermal problems with time dependent boundary conditions. *International Journal of Heat and Mass Transfer*, 53(17):3540–3551, 2010.
- [74] C.B. Murray, C.R. Kagan, and M.G. Bawendi. Synthesis and characterization of monodisperse nanocrystals and close-packed nanocrystal assemblies. *Annual Review of Materials Science*, 30(1):545–610, 2000.
- [75] M. Muthana, S. Scott, N. Farrow, F. Wright, C. Murdoch, S. Grubb, N. Brown, J. Dobson, and C. Lewis. A novel magnetic approach to enhance the efficacy of cell-based gene therapies. *Gene therapy*, 15:902–10, 07 2008.
- [76] T.G. Myers. Application of non-Newtonian models to thin film flow. *Physical Review E*, 72:066302, 2005.
- [77] T.G. Myers. Optimizing the exponent in the heat balance and refined integral methods. *International Communications in Heat and Mass Transfer*, 36(2):143–147, 2009.
- [78] T.G. Myers. Optimal exponent heat balance and refined integral methods applied to Stefan problems. *International Journal in Heat and Mass Transfer*, 53(5-6):1119–1127, 2010.
- [79] T.G. Myers and C. Fanelli. On the incorrect use and interpretation of the model for colloidal, spherical crystal growth. *Journal of Colloid and Interface Science*, 536:98–104, 2019.
- [80] T.G. Myers and S.L. Mitchell. Application of the combined integral method to Stefan problems. *Applied Mathematical Modelling*, 35:4281–4294, 2011.
- [81] T.G. Myers, S.L. Mitchell, and F. Font. Energy conservation in the one-phase supercooled Stefan problem. *International Communications in Heat and Mass Transfer*, 39(10):1522 – 1525, 2012.

-
- [82] A. Nacev, C. Beni, O. Bruno, and B. Shapiro. The behaviors of ferromagnetic nano-particles in and around blood vessels under applied magnetic fields. *Journal of magnetism and magnetic materials*, 323(6):651–668, 2011.
- [83] H. Ockendon and J. R. Ockendon. *Viscous Flow*. Cambridge Texts in Applied Mathematics. Cambridge University Press, 1995.
- [84] R.G. Owens and T.N. Phillips. *Computational rheology*, volume 14. World Scientific, 2002.
- [85] B. Pan, R. He, F. Gao, D. Cui, and Y. Zhang. Study on growth kinetics of CdSe nanocrystals in oleic acid/dodecylamine. *Journal of Crystal Growth*, 286(2):318 – 323, 2006.
- [86] Q.A. Pankhurst, J. Connolly, S.K. Jones, and J. Dobson. Applications of magnetic nanoparticles in biomedicine. *Journal of Physics D: Applied Physics*, 36(13):R167–R181, 2003.
- [87] J. Park. Liposome-based drug delivery in breast cancer treatment. *Breast cancer research : BCR*, 4:95–9, 02 2002.
- [88] J.K. Patra, G. Das, L. Fraceto, E. Campos, M. Rodríguez-Torres, L. Acosta-Torres, L. Diaz-Torres, R. Grillo, M. Swamy, S. Sharma, S. Habtemariam, and H. Shin. Nano based drug delivery systems: recent developments and future prospects. *Journal of Nanobiotechnology*, 16, 12 2018.
- [89] X. Peng, J. Wickham, and A.P. Alivisatos. Kinetics of II-VI and III-V colloidal semiconductor nanocrystal growth: “focusing” of size distributions. *Journal of the American Chemical Society*, 120(21):5343–5344, 1998.
- [90] Z.A. Peng and X. Peng. Mechanisms of the shape evolution of CdSe nanocrystals. *Journal of the American Chemical Society*, 123(7):1389–1395, 2001.
- [91] S. Perrault, C. Walkey, T. Jennings, H. Fischer, and W. Chan. Mediating tumor targeting efficiency of nanoparticles through design. *Nano letters*, 9:1909–15, 05 2009.

- [92] National Library of Medicine (US). Genetics Home Reference. Capillaries. <https://ghr.nlm.nih.gov/art/large/capillaries.jpeg>, 2020.
- [93] H. Ribera and T.G. Myers. A mathematical model for nanoparticle melting with size-dependent latent heat and melt temperature. *Microfluidics and Nanofluidics*, 20, 11 2016.
- [94] G. Richardson, K. Kaouri, and H.M. Byrne. Particle trapping by an external body force in the limit of large Péclet number: applications to magnetic targeting in the blood flow. *European Journal of Applied Mathematics*, 21(1):77–107, 2010.
- [95] I. Rukshin, J. Mohrenweiser, P. Yue, and S. Afkhami. Modeling superparamagnetic particles in blood flow for applications in magnetic drug targeting. *Fluids*, 2(2):29, 2017.
- [96] S. Sarian and H.W. Weart. Kinetics of coarsening of spherical particles in a liquid matrix. *Journal of Applied Physics*, 37(4):1675–1681, 1966.
- [97] G. Schmid. *Clusters and Colloids: From Theory to Applications*. John Wiley & Sons, 2008.
- [98] B. Shapiro, S.D. Kulkarni, A. Nacev, S. Muro, P. Stepanov, and I. Weinberg. Open challenges in magnetic drug targeting. *Wiley Interdisciplinary Reviews: Nanomedicine and Nanobiotechnology*, 7, 10 2014.
- [99] J. Sherwood, D. Holmes, E. Kaliviotis, and S. Balabani. Spatial distributions of red blood cells significantly alter local haemodynamics. *PloS one*, 9:e100473, 06 2014.
- [100] T. Sochi. Non-Newtonian flow in porous media. *Polymer*, 51(22):5007 – 5023, 2010.
- [101] J. Stefan. Über die theorie der eisbildung, insbesondere über die eisbildung in polarmeere. *Annalen der Physik*, 278(2):269–286, 1891.
- [102] H. Su, J. D. Dixon, A. Y. Wang, J. Low, J. Xu, and J. Wang. Study on growth kinetics of CdSe nanocrystals with a new model. *Nanoscale Research Letters*, 5(5):823–828, 2010.

-
- [103] T. Sugimoto. Preparation of monodispersed colloidal particles. *Advances in Colloid and Interface Science*, 28:65–108, 1987.
- [104] D.V. Talapin, A.L. Rogach, M. Haase, and H. Weller. Evolution of an ensemble of nanoparticles in a colloidal solution: theoretical study. *The Journal of Physical Chemistry B*, 105(49):12278–12285, 2001.
- [105] K. Tanabe. Optical radiation efficiencies of metal nanoparticles for optoelectronic applications. *Materials Letters*, 61:4573–4575, 2007.
- [106] R. Tao and K. Huang. Reducing blood viscosity with magnetic fields. *Physical review. E, Statistical, nonlinear, and soft matter physics*, 84:011905, 07 2011.
- [107] N. Varghese and C.N.R. Rao. Growth kinetics of platinum nanocrystals prepared by two different methods: Role of the surface. *Journal of Colloid and Interface Science*, 365(1):117 – 121, 2012.
- [108] R. Viswanatha and D.D. Sarma. *Growth of nanocrystals in solution*, pages 139–170. Wiley Online Library, 2007.
- [109] P.A. Voltairas, D. Fotiadis, and L. Michalis. Hydrodynamics of magnetic drug targeting. *Journal of biomechanics*, 35:813–21, 07 2002.
- [110] P.W. Voorhees. The theory of Ostwald ripening. *Journal of Statistical Physics*, 38(1-2):231–252, 1985.
- [111] P.W. Voorhees. Ostwald ripening of two-phase mixtures. *Annual Review of Materials Science*, 22:197–215, 1992.
- [112] P.W. Voorhees and M.E. Glicksman. Solution to the multi-particle diffusion problem with applications to Ostwald ripening - I. Theory. *Acta Metallurgica*, 32(11):2001–2011, 1984.
- [113] P.W. Voorhees and M.E. Glicksman. Solution to the multi-particle diffusion problem with applications to Ostwald ripening - II. Computer simulations. *Acta Metallurgica*, 32(11):2013–2030, 1984.

- [114] E. Voura, J. Jaiswal, H. Mattoussi, and S. Simon. Tracking metastatic tumor cell extravasation with quantum dot nanocrystals and fluorescence emission-scanning microscopy. *Nature medicine*, 10:993–8, 10 2004.
- [115] C. Wagner. Theorie der alterung von niederschlägen durch umlösen (Ostwald-reifung). *Zeitschrift für Elektrochemie, Berichte der Bunsengesellschaft für physikalische Chemie*, 65(7-8):581–591, 1961.
- [116] G. Wang, S. Gao, R. Tian, J. Miller-Kleinhenz, Z. Qin, T. Liu, L. Li, F. Zhang, Q. Ma, and L. Zhu. Theranostic hyaluronic acid-iron micellar nanoparticle for magnetic field-enhanced in vivo cancer chemotherapy. *ChemMedChem*, 13, 10 2017.
- [117] M. Wilson, R. Kerlan, N. Fidelman, A. Venook, J. Laberge, J. Koda, and R. Gordon. Hepatocellular carcinoma: Regional therapy with a magnetic targeted carrier bound to doxorubicin in a dual MR imaging/ conventional angiography suite-initial experience with four patients. *Radiology*, 230:287–93, 02 2004.
- [118] K.V. Wong and O. De Leon. Applications of nanofluids: current and future. *Advances in mechanical engineering*, 2:519659, 2010.
- [119] M. S. Wong and G. D. Stucky. The facile synthesis of nanocrystalline semiconductor quantum dots. *MRS Proceedings*, 676, 2001.
- [120] Z. Yang, M. Sen, and S. Paolucci. Solidification of a finite slab with convective cooling and shrinkage. *Applied Mathematical Modelling*, 27(9):733–762, 2003.
- [121] H. Ye, Z. Shen, L. Yu, M. Wei, and Y. Li. Manipulating nanoparticle transport within blood flow through external forces: an exemplar of mechanics in nanomedicine. *Proceedings of the Royal Society A: Mathematical, Physical and Engineering Sciences*, 474, 2018.
- [122] P. Yue, S. Lee, S. Afkhami, and Y. Renardy. On the motion of superparamagnetic particles in magnetic drug targeting. *Acta Mechanica*, 223, 03 2012.
- [123] C. Zoppou and J.H. Knight. Analytical solution of a spatially variable coefficient advection–diffusion equation in up to three dimensions. *Applied Mathematical Modelling*, 23(9):667 – 685, 1999.